

DISS. ETH NO. 22249

**NOVEL MINIATURE MOTORS FOR  
WIDE SPEED AND TORQUE RANGES**

A thesis submitted to attain the degree of  
DOCTOR OF SCIENCES of ETH ZURICH

(Dr. sc. ETH Zurich)

presented by

ARDA TÜYSÜZ

M.Sc., RWTH Aachen

born on 18.02.1984

citizen of Turkey

accepted on the recommendation of

Prof. Dr. Johann W. Kolar  
Prof. Dr. ir. Johan Driesen

2014



# Contents

<b>Acknowledgments</b>	<b>1</b>
<b>Abstract</b>	<b>3</b>
<b>Kurzfassung</b>	<b>5</b>
<b>Notation</b>	<b>7</b>
<b>1 Introduction</b>	<b>11</b>
1.1 Motivation and applications . . . . .	11
1.1.1 High power density . . . . .	11
1.1.2 High reliability . . . . .	12
1.1.3 Drives for wide torque and speed ranges . . . . .	12
1.2 State of the art . . . . .	13
1.3 Novel machine topology . . . . .	14
1.4 Challenges . . . . .	15
1.5 Outline of the thesis . . . . .	16
1.6 Scientific contributions . . . . .	17
1.7 List of publications . . . . .	19
<b>2 Proposed machine concept</b>	<b>21</b>
2.1 Concept description . . . . .	21
2.2 Modeling approach . . . . .	24
2.3 Optimization method . . . . .	27
<b>3 Design and construction of the machine</b>	<b>29</b>
3.1 Proof of concept and topology comparison . . . . .	29

3.1.1	Specifications . . . . .	29
3.1.2	Geometric parametrization . . . . .	30
3.1.3	Loss models . . . . .	30
3.1.4	Simulation results . . . . .	33
3.2	Electromagnetic design of the first prototype . . . . .	42
3.2.1	Improvements of the loss models . . . . .	46
3.2.2	Simulation results . . . . .	50
3.3	Hardware realization . . . . .	55
3.3.1	Rotor stresses . . . . .	55
3.3.2	Rotor dynamics . . . . .	63
3.3.3	Stator construction . . . . .	64
3.3.4	Positioning of the stator parts . . . . .	65
<b>4</b>	<b>Experimental verification of the machine design</b>	<b>71</b>
4.1	Standstill torque measurement . . . . .	72
4.2	No-load loss measurement . . . . .	74
4.3	Measurement results . . . . .	76
<b>5</b>	<b>Driving the lateral-stator machine</b>	<b>83</b>
5.1	Self-sensing rotor position detection . . . . .	83
5.1.1	State of the art . . . . .	83
5.1.2	Proposed signal injection method . . . . .	85
5.2	Active torque ripple compensation . . . . .	90
5.3	Hardware realization . . . . .	97
5.3.1	Power electronics . . . . .	97
5.3.2	Rotor position sensing . . . . .	101
5.4	Software realization . . . . .	108
5.5	Experimental results . . . . .	108
5.5.1	Active torque ripple compensation . . . . .	108
5.5.2	Rotor position estimation . . . . .	109
<b>6</b>	<b>Position estimation using sensing coils</b>	<b>119</b>
6.1	Introduction . . . . .	119
6.2	Concept description . . . . .	121
6.3	2-D FEM simulations . . . . .	122
6.4	Hardware realization of sensing coils . . . . .	125
6.5	Design of sensor electronics . . . . .	126
6.6	Further design aspects . . . . .	131
6.7	Measurement results . . . . .	133

---

<b>7</b>	<b>Comparison with the state of the art</b>	<b>141</b>
7.1	Slotless topology . . . . .	142
7.2	Slotted topology with concentrated windings . . . . .	144
7.3	Comparison . . . . .	148
<b>8</b>	<b>Improved machine design and integration in a medical application</b>	<b>155</b>
8.1	Thermal analysis of a dental handpiece . . . . .	157
8.2	Electromagnetic design of the machine . . . . .	168
8.2.1	Modeling . . . . .	168
8.2.2	Simulation results . . . . .	171
<b>9</b>	<b>Conclusions</b>	<b>181</b>
9.1	Summary . . . . .	181
9.2	Outlook . . . . .	184
	<b>Curriculum Vitae</b>	<b>195</b>



# Acknowledgments

First and foremost, I would like to thank Prof. Johann W. Kolar giving me the opportunity to be part of the excellent working environment he has set up at the Power Electronic Systems (PES) Laboratory of ETH Zurich. It has been, and always will be, an honor to have worked under his supervision. My PhD work is the result of the fine balance between his friendly and encouraging supervision and his willingness to let me pursue my own research ideas. I appreciate everything I have learned from him, not only in terms of designing converters and actuators that perform beyond the state-of-the-art, but also in terms of carrying out high-quality research projects that are well appreciated by colleagues world wide.

I would like to thank Prof. Johan Driesen from KU Leuven for accepting to be the co-examiner of my PhD thesis. I truly appreciate his interest in my work.

Christof Zwysig has played a very important role in my decision to stay in Zurich and pursue a PhD degree following my Master's thesis, which he supervised. I thank him very much for all his support starting from my very first days in Zurich as an exchange student until the end of my PhD study. I would also like to thank Martin Bartholet, Daniel Krähenbühl and all the Celeroton team for their help and friendship through the years.

I would like to thank Peter Albrecht, Peter Seitz, Monica Kohn-Müller, Prisca Maurantonio, Roswitha Coccia, Damaris Egger and Beat Seiler for maintaining the clockwork organization of PES. A big thank you goes to Claudia Stucki and Markus Berger for providing us with high quality IT services.

At different times during my PhD studies at PES, I shared my office with Thomas Baumgartner, Andreas Looser, Andreas Müsing, Jonas

Mühlethaler, Hirofumi Uemura, David Boillat, Michael Flankl, Mario Mauerer and Thomas Nussbaumer. I would like to thank all of them for all the good times and interesting technical discussions we had.

Each interaction with every single current and past PES member has contributed making my stay at PES unforgettable. Of these wonderful spirits, I would like to mention especially Uwe Badstübner, Ivana Kovačević, Gabriel Ortiz, Christoph Marxgut, Yanick Lobsiger, Lukas Fässler, Thiago Soeiro, Daniel Christen, Bernardo Cougo, Patricio Cortés, Toke Andersen, Andrija Stupar, Dominik Bortis and Florian Krismer.

In various projects I had the privilege to work closely with Ralph Burkart, Matthias Kasper, Christoph Gammeter, Manish Mittal and Yannick Drapela. I am grateful for everything I have learned from them.

A special thank you goes to Roman Bosshard and Jonas Huber for accepting me in their office every time I needed a distraction.

I had the chance to be the thesis supervisor/co-supervisor of more than 25 students during my stay at PES. I would like to thank all of them for the good work they did. Among them, I would like to acknowledge the support of Marco Schöni, David Koller, Patrik Brülisauer, Stefan Abrach, Maurus Kaufmann, Tobias Wellerdieck and Corinne Doppmann whose works contributed directly to this thesis.

I would like to thank my flatmates Leila Mahmoudi and Pavlin Mavrodiev for sharing the ups and downs of the student life away from home with me.

Finally, I would like to thank my family for everything that I am and everything that I have.

Last but not least, I thank my lovely girlfriend Andrea for being extremely understanding at times when I asked her for sacrifices for the sake of my work. There is no way for me to express my gratitude and love to her in a foreign language, or in any language for that matter.

Arda Tüysüz  
Zurich, September 2014

# Abstract

High-speed electrical drives are becoming increasingly popular in industrial applications such as portable power generation, turbocompressors, micro-machining spindles, attitude control systems and high-speed scanning. Some of these applications such as turbocompressors benefit from a higher power density when the rotational speed is increased. In some other applications such as a micro-machining spindles, mechanical transmission stages can be omitted when high-speed electrical drives are used, leading to more reliable systems with less maintenance requirement. However, in some micro-machining applications the volume of the tool housing may limit the size of the direct-drive machine and the maximum torque that can be generated.

In this work, a novel electrical machine topology is presented for high-speed, direct-drive spindle applications where the space in the tool head is limited. The stator of the machine grows in one lateral direction outside the tool head, making use of the space that would otherwise not be utilized by a standard electrical machine placed in the tool head. The proposed machine is called the *Lateral-Stator Machine* (LSM) due to the shape of its stator.

Two different types of LSMs are identified. For both of them, the machine geometry is parametrized and 2-D FEM simulations are used to analyze the effect of different design parameters on the machine performance, and to find the optimum machine in the design space. A prototype is realized in hardware considering the mechanical aspects of the design such as the stresses in the rotor due to centrifugal forces and the rotor dynamics.

A test bench, which is capable of measuring the torque and losses of the machine without the effect of mechanical friction, is developed. The design procedure is experimentally verified using this test bench.

An FEM-based current profiling approach is presented to compensate the torque ripple originating from the asymmetric structure of the machine, the partial saturation of the stator core and the stator slotting. An impedance-tracking-based self-sensing method is presented as well as the design and experimental verification of another position sensing method where sensing coils are integrated into the machine.

The design process is shown for an LSM that is to be integrated in a given dental handpiece, considering the specific geometric constraints and cooling options of the application.

A comparison to state-of-the-art electrical machines reveals the advantages of the LSM for applications with confined spaces. For a specific micro-machining application, an LSM leads to at least three times higher local torque density compared to standard cylindrical electric machines.

# Kurzfassung

Elektrische Hochgeschwindigkeitsantriebe werden zunehmend in industriellen Anwendungsbereichen eingesetzt. Sie kommen in tragbaren Stromgeneratoren, in Turbokompressoren, in der Mikrobearbeitungstechnik, für die Lageregelung von Satelliten und für das Hochgeschwindigkeitsscannen zum Einsatz. Einige dieser Anwendungen, z.B. Turbokompressoren, profitieren bei einer gesteigerten Drehzahl von einer höheren Leistungsdichte. In anderen Anwendungen, wie in der Mikrobearbeitungstechnik, kann mit Hilfe von Hochgeschwindigkeitsantrieben auf den Einsatz von ansonsten notwendigen Getriebestufen verzichtet werden. Dadurch werden eine höhere Zuverlässigkeit und ein reduzierter Wartungsaufwand erreicht. In manchen Anwendungen der Mikrobearbeitungstechnik steht jedoch nur begrenzter Bauraum zur Verfügung, was unmittelbar die Grösse des Direktantriebes und damit das erzeugbare Drehmoment begrenzt.

In dieser Arbeit wird eine neuartige Maschinentopologie für Hochgeschwindigkeitsdirektantriebe präsentiert, welche für Anwendungen mit begrenztem Bauraum im Werkzeugkopf besonders geeignet ist. Im Besonderen zeichnet sich die vorgestellte elektrische Maschine dadurch aus, dass der Stator in eine Querrichtung ausgedehnt ist und dadurch Bauraum ausserhalb des Werkzeugkopfes genutzt werden kann, welcher beim Einsatz einer konventionellen elektrischen Maschine ungenutzt bliebe. Dieser Maschinentyp wird deshalb als *Lateral-Stator Machine* (LSM) bezeichnet.

Die parametrisierte Maschinengeometrie wird mit Hilfe von 2-D FEM Simulationen optimiert. Um den Entwurfsprozess zu verifizieren, wird ein Prüfstand entwickelt, welcher unbeeinflusst von mechanischer Reibung, das Drehmoment und die Verluste der Maschine messen kann. Des Weiteren wird ein FEM-basiertes Verfahren zur Optimierung des

Stromprofile vorgestellt, mit dem die Drehmomentwelligkeit aufgrund der asymmetrischen Bauform der LSM, der partiellen Sättigung des Stator Eisens und aufgrund des Effekts der Statornuten kompensiert werden kann. Ausserdem werden die Entwicklung und die experimentelle Überprüfung von zwei verschiedenen Verfahren zur Rotorlageerkennung beschrieben.

Ein direkter Vergleich mit dem Stand der Technik auf dem Gebiet der elektrischen Maschinen zeigt die Überlegenheit der LSM-Topologie für Anwendungen mit begrenztem Bauraum. Für eine spezielle Anwendung in der Mikrobearbeitungstechnik zeigt sich, dass eine LSM eine dreimal so hohe lokale Drehmomentdichte wie eine konventionelle zylindrische Maschine aufweist.

# Notation

## Symbols

$a_l$	Leg cross-sectional area
$A$	Magnetic vector potential
$a_c$	Cross-sectional area of a solid conductor
$a_{rov}$	Roving cross-sectional area
$a_w$	Winding cross-section area (coil side)
$B_r$	Remanent flux density
$B_{sat}$	Saturation flux density
$c$	Specific heat capacity
$c_f$	Air-friction coefficient
$d$	Hydraulic diameter
$d_r$	Rotor diameter
$d_t$	Tool housing depth
$e_b$	Back EMF
$E_{b, rms}$	RMS value of phase back EMF
$f_{inj}$	Injection frequency
$f_{res}$	Resonance frequency
$F_c$	Centrifugal force
$F_h$	Reactive force on the magnet-shaft interface
$F_s$	Force in the sleeve
$g_a$	Air gap
$g_{si}$	Shielding iron gap
$h$	Heat transfer coefficient

$h_s$	Shoe height
$I$	Axial moment of inertia
$I_{\text{rms}}$	Resonance frequency
$I_t$	Total current in a solid conductor
$i_d, i_q$	Direct and quadrature axis currents
$J_s$	Current density of an unknown source
$J_t$	Total current density in a solid conductor
$k_f$	Filling factor
$k_s$	Stacking factor
$l_a$	Active length
$l_l$	Leg length
$m_{\text{pre}}$	Mass of the preload
$N_w$	Number of winding turns
$p$	Number of pole pairs
$P_{\text{air}}$	Air-friction losses
$P_{\text{cu}}$	Copper losses
$P_{\text{eddy}}$	Eddy-current losses
$P_{\text{fe}}$	Stator core losses
$P_{\text{no-load}}$	No-load losses
$Q$	Number of slots
$r_b$	Stator bore radius
$r_r$	Rotor radius
$r_s$	Stator radius
$s$	Surface
$T$	Torque
$t$	Time
$T_l$	Load torque
$t_m$	Magnet thickness
$t_{\text{si}}$	Shielding iron thickness
$t_{\text{sl}}$	Sleeve thickness
$t_w$	Winding thickness
$T_m$	Torque applied on a rotating shaft
$V$	Volume
$\dot{V}_{\text{air}}$	Volumetric flow rate of air

---

$w_h$	Tool head width
$w_l$	Stator leg or tooth width
$w_s$	Shaft width or radius
$w_t$	Tool neck width
$w_w$	Coil side width
$w_y$	Yoke width
$\alpha$	Magnet span
$\alpha_{sc}$	Sensing coil angle
$\delta_i$	Fluid temperature at the inlet
$\delta_o$	Fluid temperature at the outlet
$\gamma$	Angle between the PM flux and the stator current space vector
$\theta$	Rotor position
$\lambda$	Thermal conductivity
$\rho$	Density
$\sigma_c$	Conductivity of a solid conductor
$\sigma_s$	Tensile stress
$\sigma_x, \sigma_y$	Stresses in x and y directions
$\tau$	Shoe span
$\tau_m, \tau_s$	Middle and side shoe spans
$\phi$	Current space vector angle
$\phi_{dm}$	Demodulation angle
$\phi_p$	Phase shift between injected signals
$\psi_{PM}$	Permanent-magnet flux
$\psi_s$	Stator flux linkage
$\omega_m$	Rotational speed (mechanical)

## Abbreviations

ADC	Analog-to-digital conversion (or converter)
DSP	Digital signal processing (or processor)
EMF	Electro-motive force

FEM	Finite element method
LSM	Lateral-stator machine
MOSFET	Metal-oxide-semiconductor field-effect transistor
NdFeB	Neodymium iron boron
Nu	Nusselt number
OPAMP	Operational amplifier
PCB	Printed circuit board
PM	Permanent magnet
PWM	Pulse-width modulation
SmCo	Samarium cobalt

# Chapter 1

## Introduction

### 1.1 Motivation and applications

High-speed electrical drives have been a very popular research topic lately. In the last decade, both academia and industry have been working on this topic intensively due to the higher power density and improved reliability that high-speed drive systems offer [1]. Especially in the last decade, high-speed drive systems have found new application areas in portable power generation, turbocompressors and spindles [2], [3]. Furthermore, a major part of the research in electrical machinery is expected to be about high-speed drives in the near future due to both advancements in enabling technologies and the advantages that high-speed drives bring in several applications [1].

#### 1.1.1 High power density

For a given power rating and cooling capability, increasing the rotational speed of an electrical machine results in lower machine volume and weight, hence higher power density [4]. This is especially beneficial in mobile applications such as heating, ventilation and air conditioning as well as turbocharging of higher-efficiency, more-electric engines of automobiles and cabin pressurization compressors of airplanes [1], [5]. As examples, a 500 000 r/min, 150 W electrically driven turbocompressor is presented in [5], and the design methodology for a 500 000 r/min, 100 W electrical machine is given in [6]. Similarly, the reaction wheels used for

attitude control of small satellites benefit from a reduced weight and increased angular momentum density with higher rotational speeds. For instance, a 250 000 r/min motor with a novel active magnetic bearing topology is investigated for small satellite reaction wheels in [7].

### 1.1.2 High reliability

High power density is not the only motivation behind high-speed electrical drives. Small and high-speed tools are used for drilling, milling and grinding in high-precision manufacturing [8]. For example, notch grinding of silicon wafers is mentioned as an application that requires up to 150 000 r/min in [9] and a 200 W, 300 000 r/min Printed Circuit Board (PCB) drilling spindle is shown in [1]. Using a high-speed drive system in such applications eliminates the need for step-up mechanical transmission stages, i.e. enables direct drive, increasing the overall reliability of the drive system. On the other hand, the reliability and the maximum lifetime of the available ball bearings decrease rapidly above 200 000 r/min. However, recent research identifies contactless concepts such as active magnetic or gas bearings as promising solutions for future high-speed applications with speeds above 500 000 r/min [10], [11].

### 1.1.3 Drives for wide torque and speed ranges

A number of high-speed applications such as turbocompressors and gas turbines have a specific working point with a defined speed and power. Hence, the electrical machines are designed and optimized for this nominal speed and power. However, there are several other high-speed applications that have different torque and speed requirements.

High-speed electrical machines used in directly driven high-precision manufacturing tools are required to operate over a wide torque and speed range. Such an application is micro-machining spindles for high-speed milling where tools with diameters as small as 0.1 mm are used. They require almost zero torque at high speeds [12], whereas higher torques are required when the same spindles are used for thread cutting at low speeds. As a further example of this type of applications, new desktop machining centers are developed to process very small work pieces for the watch industry and for the manufacturing of dental crowns [13].

Another application with similar specifications is dental handpieces. Traditionally, air turbines driven by compressed air have been used to

power dental drills. As these systems are designed for a single operating point, several different handpieces are required for different treatments, each handpiece being designed for a different operating point [8]. Furthermore, when the bur of an air-driven handpiece contacts the material to be cut, the speed drops drastically due to the resistance build-up during cutting and the air pressure needs to be regulated to maintain a constant speed of rotation [14].

Today, traditional air-driven dental handpieces are predominantly replaced by electrical handpieces where the electric motors run at up to 40 000 r/min and several stages of mechanical transmission are used to increase the speed up to 200 000 r/min at the tool head [8], [14]. Replacing an air-driven turbine with an electric drive enables an accurate speed control of the system, making the treatment more comfortable for the patient and more ergonomic for the dentist. Further optimization of the handpiece is possible by removing the gearbox by using a high-speed, direct-drive motor. However, even though the size of the motor gets smaller by increasing its speed, the space available in the head of the dental handpiece is very limited due to ergonomic reasons. This makes it a major challenge to fit a motor that is able to provide the higher torque required at lower speeds in the head of the handpiece.

## 1.2 State of the art

The commonly preferred type of electrical machine for high-speed drives is the slotless permanent-magnet synchronous machine, mainly due to its simple and robust rotor construction and weak armature reaction which limits the rotor losses induced by asynchronous field harmonics in the air gap [15]. The torque of such a machine can only be increased by increasing the machine volume (for constant relative losses). This is, however, not possible in several applications that require a small size in order not to compromise the handling flexibility. For example, in desktop micro-machining centers, the space for the milling spindle is very limited and the head size of a spindle limits the possible shapes of the work piece. Likewise, the head size of a dental handpiece influences the ergonomics for the patient and the dentist. Moreover, the maximum rotational speed of a machine is limited by the diameter and the length of the rotor due to mechanical stresses and rotor dynamics constraints [16].

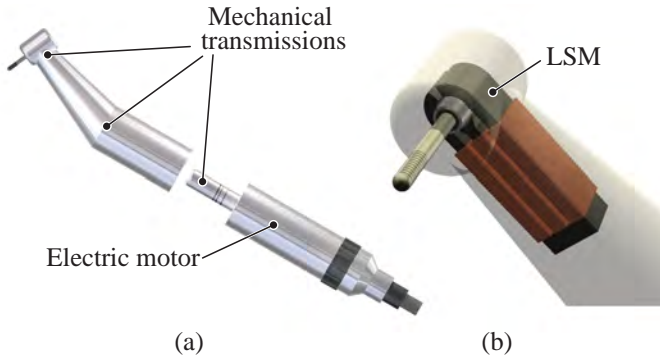


**Figure 1.1:** (a) Dental handpiece with a low-speed motor and several stages of mechanical transmission. (b) A direct-drive handpiece using a Lateral-Stator Machine (LSM).

### 1.3 Novel machine topology

In this thesis, a novel electrical machine topology, the so-called Lateral-Stator Machine (LSM) is proposed in order to overcome the drawbacks of the present high-speed motors in space restricted applications. In this section, the novel motor topology is introduced briefly considering dental drills as an example application. The state-of-the-art dental handpiece is powered by a low-speed motor (typically 40 000 r/min) placed in the body of the handpiece where there is enough space for the motor. Several stages of mechanical transmission transmits the power to the tool head as shown in Figure 1.1(a). The mechanical transmission stages introduce additional weight, acoustic noise and losses, and decrease the overall reliability of the tool. A direct drive removes the need for mechanical transmission; however, the space in the tool head is too small for a machine that can generate the desired torque. In such a case, an LSM can be used as shown in Figure 1.1(b) as it makes use of the space at the tool neck, which would otherwise not be used for magnetic parts.

## 1.4 Challenges

The major challenges in the design, optimization and control of an LSM are summarized below.

- ▶ **Modeling and optimization of the machine:** The peculiarity of the LSM is the shape of its stator, which grows in one lateral direction, resulting in an unusual machine geometry. For that reason, the models developed for analyzing the electromagnetic behavior of cylindrical rotating electrical machines cannot be used. The unusual geometry and the non-negligible effect of stray fields through the stator slots as well as the magnetic saturation in the stator teeth (in this work called the stator legs) make the electromechanical modeling of this machine even more difficult, especially considering fast analytical models. In order to capture the effects of saturation and leakage accurately for determining the optimum machine geometry, a parametric Finite Element Method (FEM) analysis needs to be set up.
- ▶ **Hardware realization:** Production of the stator core stack is challenging due to the small size and high accuracy requirement. Furthermore, positioning of the different parts of the stator and rotor correctly with respect to each other is a problem that has to be approached carefully given the small amount of usable space and the high forces pulling the rotor and the stator together due to the asymmetrical construction of the machine. Like in any other high-speed electrical machine, the rotor design requires an in-depth study of the rotor dynamics and the mechanical stresses in the rotor.
- ▶ **Testing the motor:** For verifying the design procedure, the low- (or zero-) speed, full-load torque of the machine as well as the high-speed, low- (or zero-) load losses of the machine need to be measured accurately. For a direct verification of the machine's electromagnetic design, the electromagnetic torque and the electromagnetic losses (core losses and rotor losses) need to be measured without any effect of mechanical friction from the bearings or the air in the air gap.
- ▶ **Driving the machine:** Rotor position needs to be known for a high-performance, closed-loop control of the shaft speed. State-

of-the-art position sensors require additional space, introduce additional complexity into the system, reduce the reliability and in certain applications, they bring in additional limits on the maximum operating temperature of the motor. To eliminate these problems partly or fully, a simple and robust position estimation method is needed which does not need a significant amount of additional space. Furthermore, the geometry of the LSM inherently results in a large torque ripple, which needs to be taken into account when driving the machine in order to avoid undesirable oscillations in shaft speed.

## 1.5 Outline of the thesis

The goal of this thesis is the conceptualization, analysis, optimization and experimental verification of an electrical drive system comprising a novel electrical machine topology. The peculiarity of the novel machine is the shape of its stator that grows in one lateral direction unlike in standard rotating electrical machines. The lateral-stator topology enables the use of a larger volume for torque production in direct-drive applications where the radial space around the shaft is limited by the application. Following the motivations behind the new drive system and a short summary of the state-of-the-art, the novel machine topology is introduced in Chapter 1.

Chapter 2 shows two different types of LSMs. The modeling procedure using FEM is explained and the advantages and the drawbacks of the adopted optimization method are discussed.

In Chapter 3, the two LSM topologies are comparatively analyzed for an initial set of specifications. The geometries of both machine types are parametrized and the effects of the geometric parameters on the machine performance are discussed. Based on this, a second round of optimization is carried out for a slightly different set of specifications, leading to the first hardware prototype. Furthermore, the mechanical aspects of the machine design such as the mechanical stresses in the rotor and the rotor dynamics considerations are discussed in detail. The design procedure of composite and metallic retaining sleeves are explained.

Chapter 4 deals with the design and construction of a test bench that can measure the standstill electromagnetic torque of the machine as well as the no-load losses at high speeds. Special attention is given to

avoiding the effect of mechanical friction for the torque measurement. Similarly, the segregation of the electromagnetic and mechanical no-load losses is explained. The results of the experiments are shown to verify the design procedure of the first prototype.

Chapter 5 details the design and realization of an inverter for driving the LSM. The designed inverter utilizes dedicated hardware for a novel signal-injection-based self-sensing position estimation method. Moreover, an FEM-based current profiling approach is presented to obtain the optimum current profile that leads to a ripple-free torque.

Chapter 6 introduces a novel position sensing method suitable for the section-type LSM where sensing coils are introduced in the machine. Different stages of signal injection, filtering and amplitude demodulation are explained in detail and experimental results are given to show the validity of the position sensing method at rotational speeds up to 200 000 r/min.

In Chapter 7, the LSM topology is compared to two types of standard electrical machines. The models used for optimizing the state-of-the-art machines are described briefly. A comparison between the LSM and the standard machines optimized for the same application shows the advantages of using an LSM for direct-drive applications in confined spaces.

Chapter 8 deals with the integration of an improved machine design in a dental handpiece which is identified as an example application. A lumped-parameter thermal model of the handpiece is developed. The electromagnetic design of an LSM is carried out as before, this time considering different core materials and a modified geometry that utilizes the volume better.

Finally, Chapter 9 summarizes the work presented in this thesis and suggests topics for future research.

## 1.6 Scientific contributions

The main contributions presented in this thesis are summarized below. References are given to the related publications of the author, which are compiled in Section 1.7.

- ▶ A novel machine concept is presented for high-speed applications with wide torque and speed requirements. Two possible variations of this machine concept are shown and an exhaustive parametric

FEM study is carried out to compare them and to demonstrate the maximum achievable performance in a given micro-machining application [I].

- ▶ An FEM-based, offline current profiling method is shown for the torque ripple compensation of the LSM [I].
- ▶ Design of a test bench that can evaluate the zero-speed electromagnetic torque and the high-speed, no-load electromagnetic losses of the machine excluding the effect of mechanical friction is presented. Even though developed for a specific machine type, the method can be used for any other type of electrical machine where the torque and losses need to be measured without the effect of mechanical friction [II].
- ▶ A novel, signal-injection-based self-sensing method for high-speed electrical drives is presented. Signal injection, measurement, filtering and demodulation stages are built with dedicated hardware, reducing the computational effort for the signal processor and removing any need to modify the drive inverter operation. Even though developed for a lateral-stator type machine, the differential measurements presented in this work make this method particularly useful to estimate the rotor position of very low-saliency slotless Permanent-Magnet (PM) machines which are widely used in high-speed drive applications [III].
- ▶ The FEM models of [I] are enhanced to calculate the rotor losses and to account for the rotating field effects when calculating the stator core losses. Furthermore, the effects of certain geometric parameters on the machine performance are discussed [V].
- ▶ Results of measurements taken using the test bench described in [II] are presented. The experiments verify the design procedure of the LSM [V].
- ▶ A simple and robust position estimation method that uses sensing coils is developed and experimentally verified for the LSM. This method can survive high temperatures and does not need a significant amount of additional space. Furthermore, its accuracy does not depend on the speed or the load of the machine. The design and experimental verification of this method will be discussed in detail in an upcoming publication [VI].

## 1.7 List of publications

Publications of the author that are directly related to the Ph.D. project:

*Conference papers:*

- [I] A. Tüysüz, A. Looser, C. Zwyssig, and J. W. Kolar, “Novel miniature motors with lateral stator for a wide torque and speed range,” in *Proceedings of the 36<sup>th</sup> Annual Conference of the IEEE Industrial Electronics Society (IECON)*, Phoenix, USA, Nov. 2010, pp. 1741–1747.
- [II] A. Tüysüz, D. Koller, A. Looser, and J. W. Kolar, “Design of a test bench for a lateral stator electrical machine,” in *Proceedings of the 37<sup>th</sup> Annual Conference of the IEEE Industrial Electronics Society (IECON)*, Melbourne, Australia, Nov. 2011, pp. 1801–1806.
- [III] A. Tüysüz, M. Schöni, and J. W. Kolar, “Novel signal injection methods for high-speed self-sensing electrical drives,” in *Proceedings of the IEEE Energy Conversion Congress and Exposition (ECCE USA)*, Raleigh, USA, Sep. 2012, pp. 4663–4670.

*Workshops:*

- [IV] A. Tüysüz, and J. W. Kolar, “The use of FEM tools for the design, control and optimization of high-speed electrical drives,” *ANSYS Conference & 32<sup>th</sup> CADFEM Users’ Meeting*, Nuremberg, Germany, Jun. 2014.

*Journal papers:*

- [V] A. Tüysüz, C. Zwyssig, and J. W. Kolar, “A novel motor topology for high-speed micro-machining applications,” *IEEE Transactions on Industrial Electronics*, Vol. 61, No. 6, pp. 2960–2968, Jun. 2014.
- [VI] A. Tüysüz and J. W. Kolar, “Integrated position sensors for an unconventional electrical machine topology,” *IEEE Transactions on Magnetics*, under preparation to be submitted in Apr. 2015.

Further publications of the author in the field of electrical drives:

*Conference papers:*

- [VII] B. Cougo, A. Tüysüz, J. Mühlethaler, and J. W. Kolar, “Increase of tape wound core losses due to interlamination short circuits and orthogonal flux components,” in *Proceedings of the 37<sup>th</sup> Annual Conference of the IEEE Industrial Electronics Society (IECON)*, Melbourne, Australia, Nov. 7-10, 2011, pp. 1372–1377.
- [VIII] L. Schwager, A. Tüysüz, C. Zwyssig, and J. W. Kolar, “Modeling and comparison of machine and converter losses for PWM and PAM in high-speed drives,” in *Proceedings of the International Conference on Electrical Machines (ICEM)*, Marseille, France, Sep. 2012, pp. 2441–2447.
- [IX] A. Tüysüz, A. Schaubhut, C. Zwyssig, and J. W. Kolar, “Model-based loss minimization in high-speed motors,” in *Proceedings of the IEEE International Electric Machines and Drives Conference (IEMDC)*, Chicago, USA, May 2013, pp. 332–339.
- [X] A. Tüysüz, R. Bosshard, and J. W. Kolar, “Performance comparison of a GaN GIT and a Si IGBT for high-speed drive applications,” in *Proceedings of the International Power Electronics Conference (ECCE Asia)*, Hiroshima, Japan, May 2014, pp. 1904–1911.
- [XI] C. Gammeter, Y. Drapela, A. Tüysüz, and J. W. Kolar, “Weight optimization of a machine for airborne wind turbines,” in *Proceedings of the 40<sup>th</sup> Annual Conference of the IEEE Industrial Electronics Society (IECON)*, Dallas, USA, Oct. 2014.

*Journal papers:*

- [XII] L. Schwager, A. Tüysüz, C. Zwyssig, and J. W. Kolar, “Modeling and comparison of machine and converter losses for PWM and PAM in high-speed drives,” *IEEE Transactions on Industry Applications*, Vol. 50, No. 2, pp. 995–1006, Mar/Apr. 2014.
- [XIII] A. Tüysüz, A. Schaubhut, C. Zwyssig, and J. W. Kolar, “Model-based loss minimization in high-speed Motors,” *IEEE Transactions on Industry Applications*, under preparation to be submitted in Apr. 2015.

# Chapter 2

## Proposed machine concept

### 2.1 Concept description

The LSM is introduced in Section 1.3. It is depicted in a dental hand-piece in Figure 1.1(b). As it can be seen in that figure, the drill is directly mounted to the rotor without any additional gearbox, resulting in a direct-drive system. The shape of the stator is modified such that the windings can be relocated from the area where the space is limited. By carrying the permanent-magnet flux out of this restricted space, the stator can be made longer to gain more space for the windings.

Two possible designs of the LSM are shown in Figure 2.1. The machine shown in Figure 1.1(b) and in Figure 2.1(a) is called the *surrounding-type* LSM as the stator *surrounds* the rotor. It is derived from a three-phase, two-pole, three-slot electrical machine with double-layer concentrated windings. The shape of the stator is modified by moving the windings away from the area where the space is limited. More space is gained for the windings by making the stator teeth longer and guiding the permanent-magnet flux out of the confined space.

The machine depicted in Figure 2.1(b) is another type of LSM, which is called the *section-type* LSM, as the lateral stator covers only a *section* of the rotor. The winding topology is identical to the surrounding type, with contracted windings, each phase being wound on a separate leg. As the stator does not fully enclose the rotor in this configuration, a

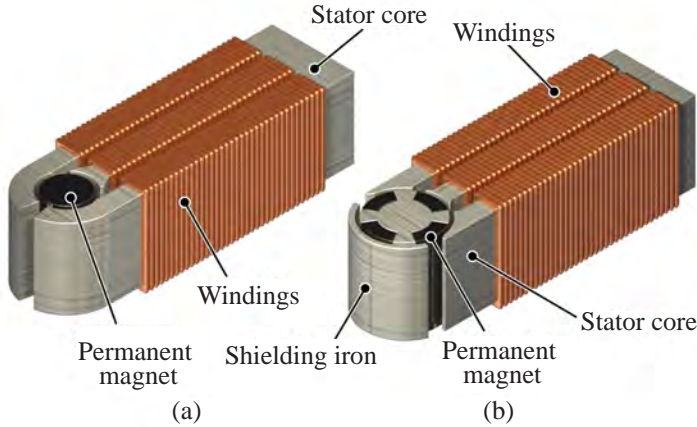


**Figure 2.1:** Two lateral-stator machine (LSM) topologies: (a) machine with surrounding stator and (b) with section stator.

shielding iron is used to guide the magnetic field of the rotor magnets that are not facing the stator core. This implies that in the section-type LSM, only part of the permanent magnets placed in the rotor contribute to torque production at a given rotor position. On the other hand, as the stator does not extend around the rotor, the rotor can be larger and therefore have more permanent-magnet material compared a surrounding-type LSM. Similar machine concepts have been presented in [17] and [18]; however neither a systematic analysis of the machines nor any considerations on optimization or driving the machines have been given.

Figure 2.2 shows the middle leg of an LSM that can be of either the surrounding or the section type. If the space for the machine is not growing immediately outside the tool head, i.e. if the legs of the LSM are parallel to each other as shown in Figure 2.1, the stator leg width  $w_1$  is small enough to assume that the permanent magnets drive the stator leg into saturation. In other words, if  $a_1 = w_1 \cdot l_a$  where  $l_a$  is the active length<sup>1</sup> of the machine, the flux linkage  $\Psi_s$  can be defined by the cross-sectional area of the stator leg  $a_1$ , the saturation flux density of the core material  $B_{\text{sat}}$  and the number of turns  $N_w$

<sup>1</sup>Thickness of the stator leg perpendicular to the page plane.

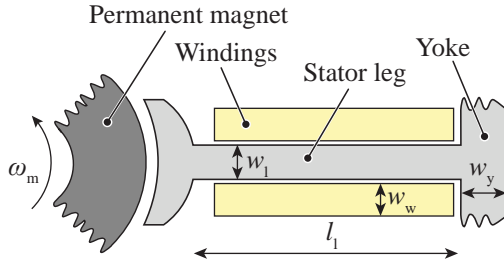


**Figure 2.2:** Middle leg of an LSM that can be of either the surrounding or the section type.

$$\Psi_s = a_l B_{\text{sat}} N_w. \quad (2.1)$$

The back Electro-Motive Force (EMF)  $e_b$  induced in this winding can be then written as a function of mechanical speed  $\omega_m$  and pole pair number  $p$

$$e_b = \Psi_s \omega_m p. \quad (2.2)$$

$$e_b = a_l B_{\text{sat}} N_w \omega_m p. \quad (2.3)$$

From (2.3) it can be seen that, when the flux linkage is assumed to be defined by the leg cross-sectional area and the saturation flux density of the core material, increasing the pole pair number would lead to a higher back EMF at the same shaft speed. This means that a section-type LSM is expected to have a higher torque-per-current ratio compared to its surrounding-type counterpart. On the other hand, as the electrical frequency is increased and the rotor diameter is bigger, the core losses and the air-friction losses are also expected to be higher in the section-type LSM.

Even though it enables direct drive in confined spaces, the lateral-stator topology inherently has certain drawbacks and limitations compared to traditional cylindrical rotating electrical machines, which have to be studied carefully during the design phase. The stator slotting and the asymmetrical air gap permeance may lead to a high cogging

torque<sup>2</sup>. Furthermore, the magnetic asymmetry of the phases (for example different self inductance of the phases wound on the side and middle legs) may lead to a non-constant torque even when excited by balanced three-phase currents. These two effects may add up to result in a large torque ripple, which may cause undesired speed oscillations, especially at low-speeds.

As described above, the thin legs of the lateral-stator structure are likely to be driven into saturation at light or even no-load conditions, meaning that an accurate design procedure has to consider magnetic saturation in the core, taking the armature reaction into account. Since the permeability of the core material decreases with increasing flux it carries, the stray flux<sup>3</sup> will limit the maximum length of the leg; i.e. increasing  $l_1$  (cf. Figure 2.2) will not increase the torque of the machine any further beyond a certain limit for given copper losses.

A further inherent property of the lateral-stator structure is the force pulling the rotor and stator together due to the unbalanced magnetic structure of the machine. This force has to be taken into account when designing the mechanical system and dimensioning the shaft.

## 2.2 Modeling approach

An analytical model for evaluating the performance of a slotless PM machine is given in [19], where the field equations are solved in polar coordinates to get the PM field distribution in the machine, taking advantage of the slotless configuration. However, there are also analytical models presented in literature which can model more complicated machine geometries and further phenomena such as the armature reaction effect.

For example, an analytical model for predicting the open circuit magnetic field distribution in a slotless PM machine is presented in [20]; an analytical expression for the field generated in the air gap and magnet regions of a slotless machine by three-phase windings has been derived in [21]; a relative permeance function to obtain the air gap flux density distribution in a slotted machine is shown in [22]; and finally, an analytical model that predicts the instantaneous magnetic field dis-

---

<sup>2</sup>Cogging torque, also known as detent torque, is the alternating torque with an average value over one rotational period equal to zero, caused by the attraction between the rotor magnets and the stator core at no-load.

<sup>3</sup>Flux crossing from one leg to the other through the winding region.

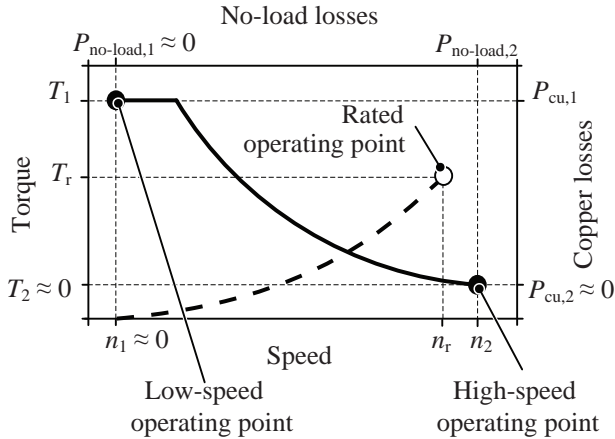


**Figure 2.3:** Torque and speed requirements of typical micro-machining and turbocompressor applications. Lower x-axis denotes speed, upper x-axis denotes no-load losses, left y-axis denotes torque and right y-axis denotes copper losses. The turbocompressor (dashed curve, white circle) may be designed and optimized for a single rated speed  $n_r$  and torque  $T_r$ , whereas the micro-machining spindle (solid curve, black circles) has a wide operating range that can be modeled with two operating points at the high- and low- speed extremes of the operational range.

tribution in a PM machine operating under any given load condition is derived in [23]. The effect of tooth tips, which has been neglected in all these models, is taken into account in [24].

However, the approaches presented in these works cannot be used here as the partial saturation of the lateral stator has a significant impact on the performance of the LSM, and all the works mentioned above neglect saturation and assume infinite permeability in the iron. Moreover, important phenomena such as stray flux or torque ripple result mainly from the shape of the lateral-stator and cannot be modeled analytically without assumptions that sacrifice accuracy. Therefore, FEM simulations are used instead of an analytical modeling approach to model and optimize the LSM.

As also mentioned in Section 1.1.3, while turbocompressors are typically designed to operate only at a rated speed and power, recent trends

in applications such as micro-machining spindles or dental handpieces show speeds from almost standstill up to 200 000 r/min. Figure 2.3 visualizes the torque and speed requirements of these two groups of high-speed applications.

For micro-machining applications, the torque for the high-speed drilling and milling is very low ( $T_2 \approx 0$ ) and can be generated with negligible current, hence negligible copper losses ( $P_{\text{cu},2} \approx 0$ ). Therefore, only the no-load losses are relevant for the high-speed operating point of the LSM.

For the low-speed operation on the other hand, the speed-dependent loss components such as the core losses or eddy current losses in the rotor can be neglected and only the copper losses are taken into account ( $P_{\text{no-load},1} \approx 0$ ).

In this thesis, the constraints and the goal of the machine design are set in the following way. Firstly, the maximum allowed values for the no-load losses at the high-speed and copper losses at the low-speed operating points are determined following a thermal study. This ensures that the machine does not overheat during continuous operation at the high-speed operating point. The low-speed operating point is an intermittent short-term operating point (for example, when the tool is loaded by a hard workpiece for a short amount of time). Therefore, maximum copper losses may be higher than the allowed no-load losses without leading to a dangerous temperature rise in the machine in this intermittent period ( $P_{\text{cu},1} > P_{\text{no-load},2}$ ). After the loss limits are set, the goal of the machine design procedure is to find the machine that produces the highest torque at the low-speed operating point while generating no more losses than the maximum allowed no-load losses at the high-speed operating point.

In order to do so, firstly the geometry of the LSM is parametrized using independent, dependent and fixed parameters. For example, considering one single stator leg as shown in Figure 2.2, the stator leg length  $l_1$  and the stator leg width  $w_1$  can be independent parameters, whereas the yoke width  $w_y$  can be defined as a dependent parameter such as  $w_y = 1.5 \cdot w_1$ . A geometric constraint introduced by the considered specific application such as  $w_t$ , the neck width of the tool in which the machine has to fit, is an example of a fixed parameter (cf. Figure 3.1). As  $w_t = 3w_1 + 4w_w$ , the winding coil side width  $w_w$  can also be considered a dependent parameter in this example. This way, a unique set of independent parameters define a unique machine for a

given set of geometric constraints.

In order to evaluate a machine, two FEM simulations are carried out, one evaluating its performance in the low-speed and the other in the high-speed operating point (cf. Figure 2.3).

For the low-speed operating point analysis, initially the machine geometry is created in a two-dimensional (2-D) FEM software environment based on the parameter set that defines the machine. The winding resistance is calculated based on the winding geometry and used to calculate the phase current that generates the maximum allowed copper losses  $P_{\text{cu},1}$ . Finally, the FEM simulation is run for an electrical period while three-phase,  $120^\circ$  phase shifted sinusoidal currents are injected into the windings. The instantaneous torque is calculated and recorded as a function of rotor position in order to evaluate its mean value and the torque ripple.

For the high-speed operating point analysis, the computation is repeated for zero winding currents and the electromagnetic no-load losses of the machine at the no-load speed  $n_2$  are calculated using the FEM software.

## 2.3 Optimization method

In order to find the optimum LSM geometry for a given application, first the limits for the low-speed copper loss ( $P_{\text{cu},1}$ ) and high-speed no-load loss ( $P_{\text{no-load},2}$ ) are defined. Then, the ranges are defined for each independent parameter. The parameter space is discretized, i.e. specific parameter values to be evaluated are defined. Finally, all the sets of independent parameters are evaluated, simulating every possible machine in the parameter range.

The advantage of such an exhaustive evaluation (also known as direct search) is its simplicity as it does not require a cost function. Furthermore, there is no risk of the optimization routine converging to a local optimum. Even though the regions of the parameter space that lead to suboptimal results may also be searched as intensively as the better regions due to the lack of an intelligent algorithm, the generated data are distributed over the entire parameter range, which allows for sensitivity analysis for any parameter and any performance criteria. The discretization steps may be chosen relatively coarse, decreasing the computational time for an initial analysis. After the verification of the design procedure, finer steps of discretization can be applied and/or the

parameter ranges can be broadened for improving the design.

# Chapter 3

## Design and construction of the machine

### 3.1 Proof of concept and topology comparison

#### 3.1.1 Specifications

In order to prove the feasibility of the LSM topology and to compare the two (surrounding and section) type of LSMs introduced earlier, a general micro-machining spindle application is considered. The high-speed operating point is selected at 200 000 r/min. As the goal is a proof of concept and comparison of the two LSM types, a detailed thermal analysis is omitted at this stage and the no-load loss limit  $P_{\text{no-load},2}$  is set to 1.2 W and the maximum allowed copper losses  $P_{\text{cu},1}$  is set to 8 W based on experience on machines of similar size and simple scaling. A detailed thermal model of an LSM is presented in Chapter 8.

Amorphous iron is chosen as core material both for the stator and rotor<sup>1</sup> due to its lower losses compared to standard electrical steels and higher saturation flux density compared to nanocrystalline alloys or ferrites. Table 3.1 summarizes the main specifications of this material.

---

<sup>1</sup>Applies to section-type LSM only.

Density ( $\text{g/cm}^3$ )	7.18
Young's modulus (GPa)	100
Saturation flux density (T)	1.56
Sheet thickness ( $\mu\text{m}$ )	23
Stacking factor	84%
Electrical resistivity ( $\mu\Omega\text{ m}$ )	1.3
Core losses at 400 Hz, 0.5 T (W/kg)	0.5
Core losses at 400 Hz, 1 T (W/kg)	1.8
Core losses at 1 kHz, 0.5 T (W/kg)	2
Core losses at 1 kHz, 1 T (W/kg)	5

**Table 3.1:** Main specifications of the amorphous iron used in this work [25].

### 3.1.2 Geometric parametrization

For evaluating different possible machines and assessing the effect of specific geometric parameters on the performance, geometries of the surrounding-type and the section-type LSMs are parametrized as shown in Figure 3.1. The analyzed parameter values are listed in Table 3.2.

### 3.1.3 Loss models

#### Core losses

Core losses in electrical machines can be calculated using the empirical formula of Steinmetz. However, this method is developed for sinusoidal variation of magnetic flux density over time, and needs to be modified to be used for nonsinusoidal flux densities in the material. In [26], the Modified Steinmetz Equation (MSE) is developed for nonsinusoidal flux waveforms. Even though the MSE considers flux only in one direction, which is not exactly the case in the whole stator of the LSM, it is used to calculate the core losses because the core volume where a significant flux rotation occurs is smaller than the core volume where the flux is only one dimensional. Furthermore, the MSE does not need any additional data apart from the easily available Steinmetz coefficients.

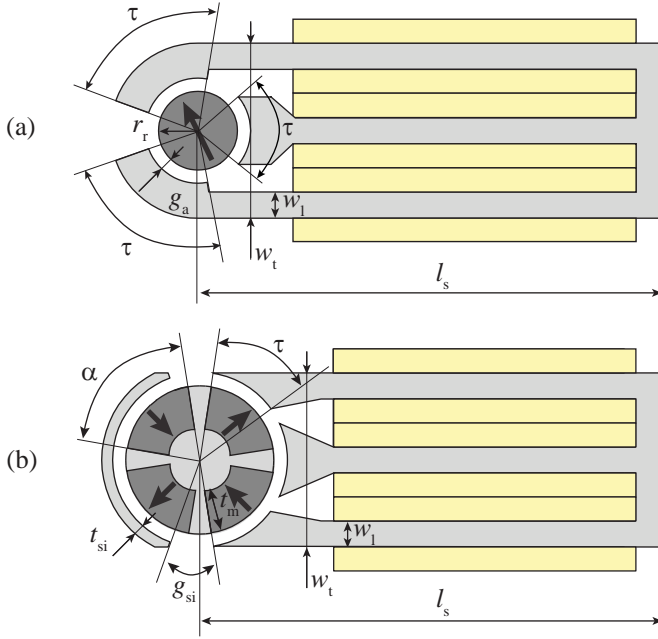


**Figure 3.1:** Cross-sectional view and geometric parameter definition of the two LSM topologies: (a) surrounding type, (b) section type. The dark gray color indicates permanent magnets with arrows showing the magnetization direction, light gray color denotes laminated core material and the yellow regions show the windings.

### Copper losses

As described earlier, copper losses are considered only at low-speeds. Assuming copper conductors thinner than twice the skin depth<sup>2</sup>, the skin effect and the proximity losses caused by the stray fields can be neglected. Thus, the total copper losses are calculated considering only the fundamental component of the current using (3.1), where  $J_p$  is the

<sup>2</sup>Skin depth is 0.8 mm for copper at 6.6 kHz, which is fundamental the frequency of a 4-pole motor running at 200 000 r/min.

Surrounding type		
$\tau$	Stator shoe span	60, 70, 80, 90, 100 and 110°
$r_r$	Rotor radius	1.5, 2 and 2.8 mm
$g_a$	Air gap	0.6, 0.8 and 1 mm
$w_l$	Stator leg thickness	0.8, 1.2, 1.6 and 1.8 mm
$l_l$	Stator length	20, 35, 40, 60 and 80 mm
$w_t$	Tool width (tool head diameter)	8 mm (fixed)
$l_a$	Active length (into page plane)	8 mm (fixed)
Section type		
$\tau$	Stator shoe span	40, 45 and 50°
$w_l$	Stator leg width	0.8, 1.2 and 1.6 mm
$l_l$	Stator length	15, 20 and 30 mm
$g_{si}$	Shielding iron gap	5, 15 and 25°
$t_m$	Magnet thickness	1, 2 and 2.5 mm
$\alpha$	Magnet span	55, 70 and 80°
$t_{si}$	Shielding iron thickness	1 mm (fixed)
$w_t$	Tool width (tool head diameter)	8 mm (fixed)
$l_a$	Active length (into page plane)	8 mm (fixed)

**Table 3.2:** Discretization of the parameter ranges including fixed parameters for the section and surrounding-type LSMs.

peak current density in the winding area,  $\sigma_{cu}$  is the conductivity of copper and  $k_f$  is the copper filling factor;  $a_w$  represents the winding cross-sectional area (i.e. area of one of the two adjacent rectangles between the stator legs in Figure 3.1) and  $l_w$  represents the winding length (i.e. total length of the winding around one stator leg). Both  $a_w$  and  $l_w$  depend on the parameters given in Table 3.2, and they are calculated separately for each independent parameter set.

$$P_{cu} = \frac{3J_p^2 a_w l_w}{2k_f \sigma_{cu}}. \quad (3.1)$$

### Air-friction losses

In [19], it is shown that the air-friction losses  $P_{air}$  of a cylindrical rotor in a constant air gap can be calculated as a function of the air density  $\rho_{air}$ , air-friction coefficient  $c_f$ , along with the rotational speed  $\omega_m$ , radius  $r_r$  and length  $l_a$  of the rotor as

$$P_{\text{air}} = c_f \pi \rho_{\text{air}} \omega_m^3 r_r^4 l_a. \quad (3.2)$$

The same approach is adopted in this work for the calculation of the air-friction losses.

### Rotor losses

Eddy currents are induced in solid conductive bodies in the rotor of an electrical machine, because of the time and space harmonics of the air-gap field [27]. To analyze those eddy currents precisely, a three-dimensional (3-D) transient FEM simulation is needed, as the eddy-current problem is a 3-D problem [28]. On the other hand, 2-D models for estimating the eddy currents have also been presented in literature [28]. However, the rotor eddy-current losses are neglected at the initial design step in this work for the sake of simplicity. Nevertheless, once the best machine in the defined parameter space is identified by the simulations, a 3-D transient FEM model of that machine is built and the rotor losses are calculated to justify the assumption that they are negligible during the initial modeling phase.

#### 3.1.4 Simulation results

Figure 3.2 shows the performance of all the simulated machines. It can be seen clearly that the section-type LSMs can produce higher torque for 8 W of given copper losses, but on the other hand they have higher no-load losses at the given rated speed of 200 000 r/min as expected due to the reasons mentioned in Section 2.1.

It can be seen in Figure 3.2 that there is a group of motors with similar performance (marked with a circle). The common geometric parameters and the resulting torque ripple<sup>3</sup> of these machines are listed on Table 3.3.

Considering that all the machines in this group have similar average torques and their no-load losses are all below the allowed limit, the best machine is chosen as the one with the minimum torque ripple. Table 3.4 shows the parameter set that defines this machine.

A 3-D transient FEM model of this machine is built to calculate the eddy-current losses in the magnets, in order to justify the as-

---

<sup>3</sup>Torque ripple is defined as the difference between maximum and minimum instantaneous torques at full load.

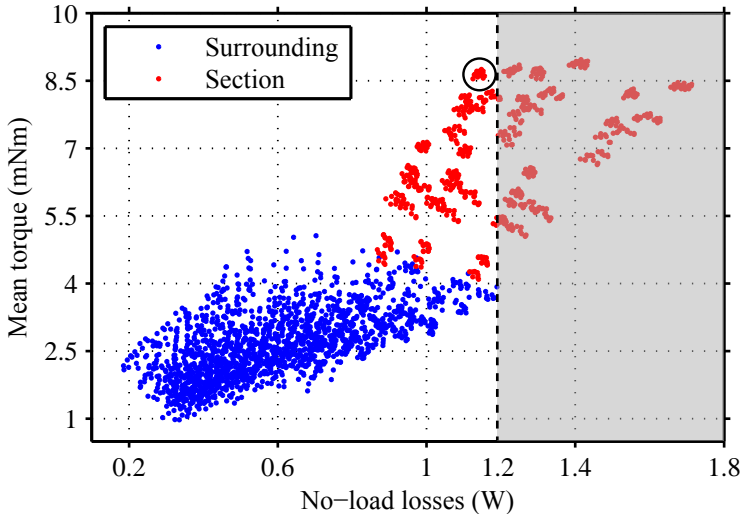


**Figure 3.2:** Performance of the analyzed surrounding-type and section-type machines. y-axis shows the mean torque of a machine when producing 8 W copper losses. x-axis shows the no-load losses at 200 000 r/min. The machines in the gray shaded region are infeasible designs due to their high no-load losses. The optimum group of machines is marked with a circle. The common geometric parameters of the machines belonging to this group are given in Table 3.3.

$w_1$	Stator leg width	1.2 mm
$l_1$	Stator length	15 mm
$\alpha$	Magnet span	80°
$t_m$	Magnet thickness	2 or 2.5 mm
	Torque ripple	3.4 to 7.5 mN m

**Table 3.3:** Common geometric parameters and the torque ripples of the group of machines highlighted in Figure 3.2.

sumption that they are negligible during the initial modeling phase. A laminated rotor core and axially segmented magnets are considered. Figure 3.3 shows the resulting model geometry along with the geometric discretization of the stator parts. The total eddy-current losses are calculated as 0.16 W, which is less than 15% of the rest of the no-load

### 3.1. PROOF OF CONCEPT AND TOPOLOGY COMPARISON

$\tau$	Stator shoe span	40°
$w_1$	Stator leg width	1.2 mm
$l_1$	Stator length	15 mm
$g_{si}$	Shielding iron gap	25°
$t_m$	Magnet thickness	2 mm
$\alpha$	Magnet span	80°
$t_{si}$	Shielding iron thickness	1 mm (fixed)
$w_t$	Tool width (tool head diameter)	8 mm (fixed)
$l_a$	Active length (into page plane)	8 mm (fixed)
$g_a$	Air gap	0.6 mm (fixed)
$k_f$	Filling factor	0.5 (fixed)
$B_r$	Remanent flux density of the magnets	1.1 T

**Table 3.4:** Parameter set defining the best machine (the one with the lowest torque ripple of 3.5 mNm) belonging to the highlighted group in Figure 3.2.

losses. Figure 3.4 shows the induced currents in one machine pole that is axially segmented into four pieces.

So far in this analysis, the performance of the surrounding and section type LSMs have been compared and the best machine in the analyzed parameter space has been identified. In the following, the effects of individual parameters on the machine performance are discussed.

For a surrounding-type LSM in a spindle with a fixed tool width  $w_t$ , the rotor radius effects the shape of the stator shoes and hence the flux distribution in the tool head region. A smaller rotor radius would imply less permanent-magnet material use and lower cost, as well as smaller mechanical stresses on the rotor surface due to centrifugal forces. Figure 3.5 shows the effect of the rotor radius on the performance of the surrounding-type LSMs. It can be seen that higher torques can be achieved by increasing the rotor radius. This however, increases the no-load losses of the machine as well.

A large stator shoe span  $\tau$  in this kind of machine also influences the flux paths in the tool head region directly. A larger shoe span helps collecting more flux and ideally leads to a higher flux linkage. However, a larger shoe span also creates a lower-impedance path for the stray flux, which decreases the flux linkage. From Figure 3.6 it can be concluded that the machines with smallest shoe spans exhibit the highest torques, which shows the dominating effect of stray flux when the stator shoes

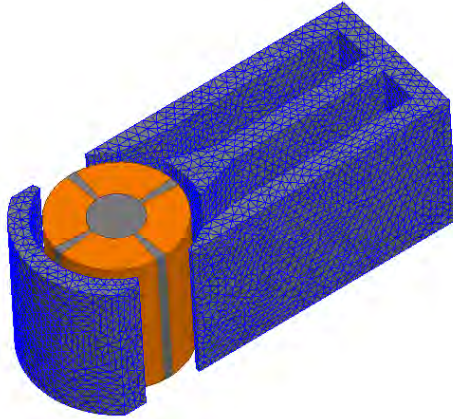


**Figure 3.3:** The 3-D FEM model used for calculating the rotor eddy-current losses. The mesh is not shown in the rotor for better visibility of the magnet segments. The windings are not included in the model as only no-load operation is considered.

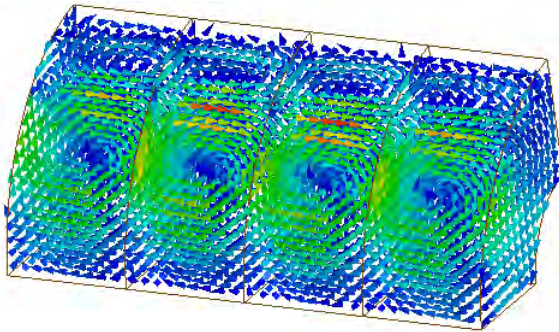


**Figure 3.4:** 3-D FEM simulation results showing the induced eddy currents in one pole of the machine at a given time. The pole is axially segmented into four pieces of permanent magnets. The magnet segments are insulated against each other and the shaft (the rotor core). The segmentation introduces additional end resistances and limits the total eddy-current losses.

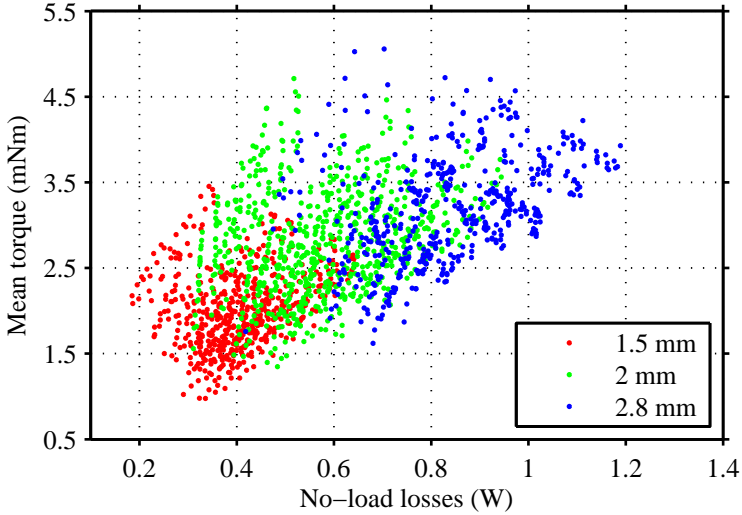


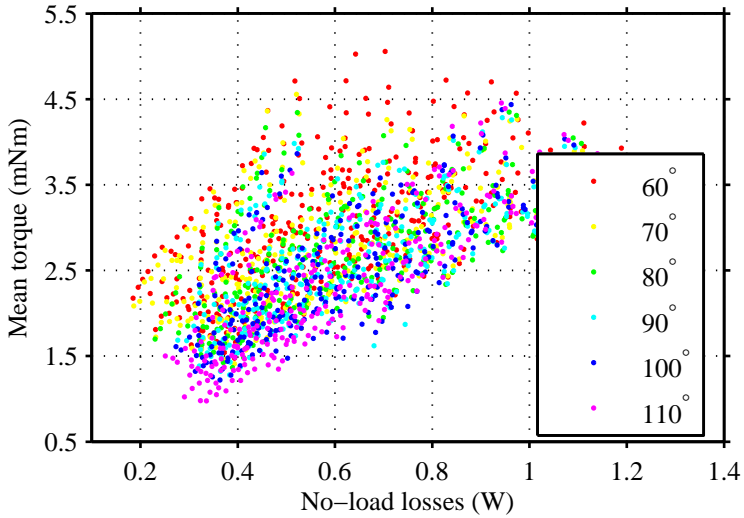
**Figure 3.5:** The effect of the rotor radius on the performance of the surrounding-type LSMs.

become wider.

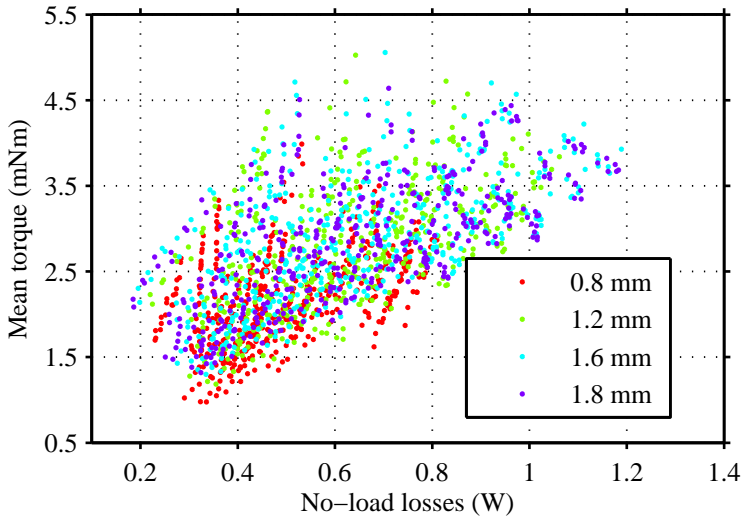
The selection of the stator leg width  $w_1$  is a trade-off between the iron and copper cross-sectional areas. A small leg width limits the maximum flux that the iron can carry. On the other hand, a small leg width leads to more space for the copper and higher phase currents for given copper losses. Figure 3.7 shows that the minimum value of the leg width (0.8mm) is not enough to carry enough flux for generating high torques, and the optimum value lies around 1.2 - 1.4 mm.

Figure 3.8 reveals a very interesting outcome of this analysis by showing that increasing the stator length leads to higher no-load losses and lower torque for the analyzed surrounding-type machines. As the copper losses are kept constant, increasing the stator length increases the winding area, decreases the winding resistance and consequently leads to higher phase currents. Thus, the counter-intuitive fact that longer stators lead to smaller torques again shows the importance of stray field in this type of electrical machines.

A small air gap in electrical machines employing permanent magnets in the rotor means a smaller magnetic reluctance between the rotor



**Figure 3.6:** The effect of the shoe span on the performance of the surrounding-type LSMs.



**Figure 3.7:** The effect of the leg width on the performance of the surrounding-type LSMs.

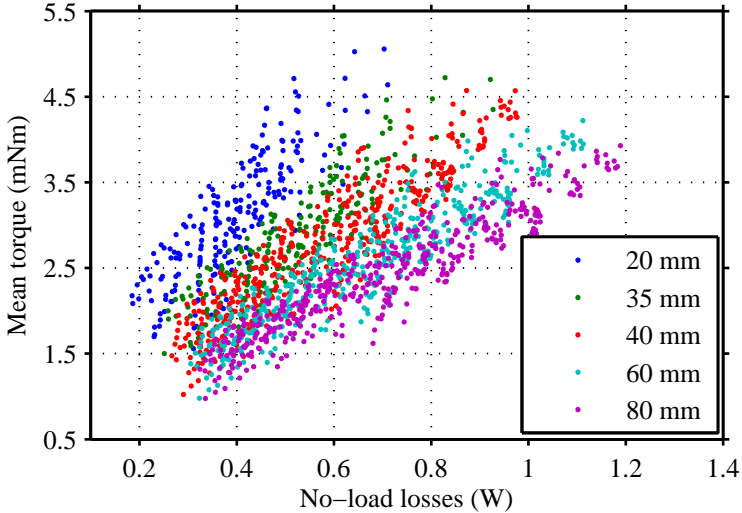


**Figure 3.8:** The effect of the stator length on the performance of the surrounding-type LSMs.

and the stator, hence higher flux linkage and higher torque-per-current. On the other hand, small air gaps require tighter production tolerances which increase the complexity and the cost of the machine manufacturing. Figure 3.9 shows that the surrounding-type machines with highest torques have small (0.6 mm) air gaps.

Sintered rare-earth permanent magnets are generally used in applications with high torque-per-volume requirements. Today, sintered NdFeB magnets with remanent flux densities higher than 1.3 T and coercive forces around 1000 kA/m are available in the market. However, the maximum operating temperature of these magnets are around 120 °C. Sintered NdFeB magnets with highest operating temperatures can be used up to around 200 °C, but these magnets have lower remanent flux densities around 1.1 T [29]. On the other hand, SmCo magnets with around 1.1 T remanent flux density, 800 kA/m coercive force and up to 350 °C maximum operating temperatures can be found in manufactures' catalogs [30]. However, the electrical conductivity of SmCo magnets is almost twice as high as that of NdFeB magnets, making them more susceptible to overheating due to eddy-current losses. Plastic-

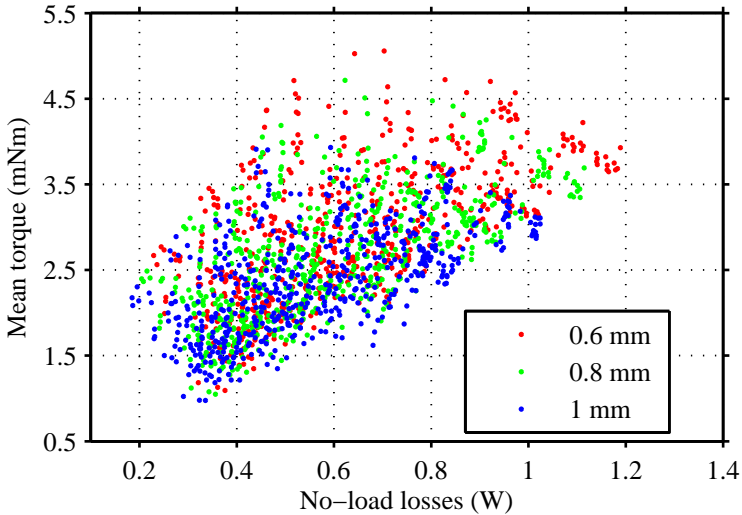


**Figure 3.9:** The effect of the air gap on the performance of the surrounding-type LSMs.

bonded magnets have much higher electrical resistance than sintered NdFeB and SmCo magnets; however, the utilization of plastic-bonded magnets leads to a larger machine volume as the energy product of plastic-bonded magnets is significantly lower compared to sintered NdFeB or SmCo magnets [31]. Figure 3.10 shows that magnets with a remanent flux density of 1.1 T lead to higher torques in the analyzed machines compared to magnets with remanent flux density of 0.8 T.

Figure 3.11 shows that the smallest simulated stator leg width is not sufficient to produce high torques in the section-type LSM, similar to what has been observed in the surrounding type. According to Figure 3.12, the simulated range of stator shoe span  $\tau$  values is not wide enough to cause a significant change in the performance. The effect of stray flux is visible in Figure 3.13, where longer stators lead to worse performance, which is also the case for the surrounding-type LSM.

A parameter that exists only in the section-type LSM is the shielding iron gap  $g_{si}$ . As seen in Figure 3.14, this parameter does not effect the mean torque of the machine directly, as it does not directly change the flux linkage. On the other hand, it changes the flux distribution in the

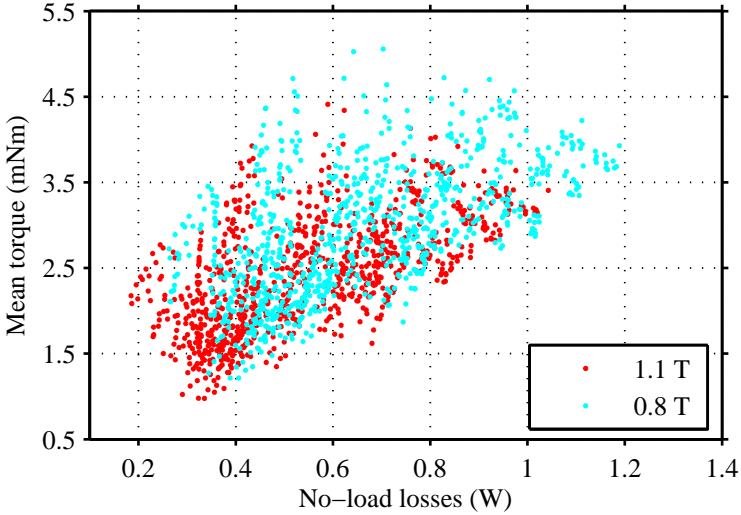


**Figure 3.10:** The effect of the remanent flux density on the performance of the surrounding-type LSMs.

tool head region, resulting in a significant effect on the cogging torque. Figure 3.15 shows the effect of  $g_{si}$  on the torque ripple and the mean torque. A bigger gap seems to result in less torque ripple. However, a bigger gap also compromises the shielding capability, which may result in failure to comply with environmental compatibility requirements and create additional eddy-current losses in the metallic tool housing or other conductive parts in the vicinity of the tool head.

Figure 3.16 shows the effect of the magnet span  $\alpha$ . In the section-type machines analyzed in this section, wider magnets result in higher torques. Similarly, Figure 3.17 depicts the effect of the magnet thickness  $t_m$  on the performance. It can be concluded that increasing the magnet thickness from 1 mm to 2 mm results in an increase in torque. A further increase to 2.5 mm on the other hand does not bring a significant increase in the machine's torque capability.

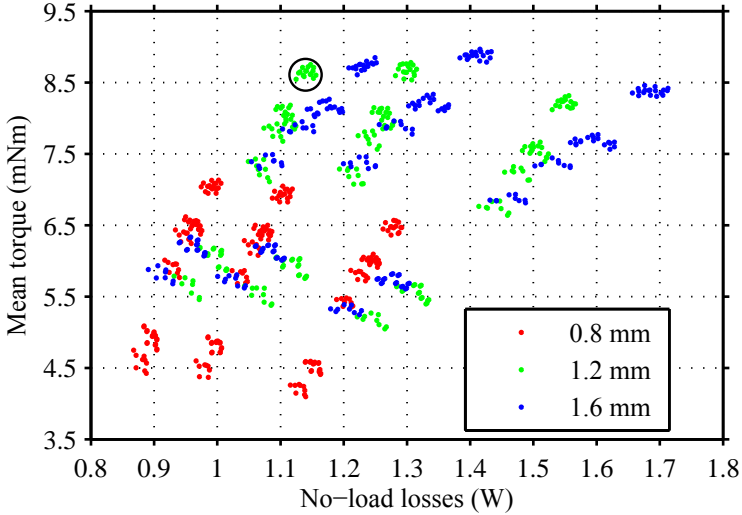


**Figure 3.11:** The effect of the leg width on the performance of the section-type LSMs. The optimum group of machines is marked with a circle.

## 3.2 Electromagnetic design of the first prototype

In the previous section, the performances of surrounding and section-type LSMs are comparatively analyzed for the specifications of a general micro-machining spindle and the effect of individual parameters on the machine performance are discussed.

This section deals with the design of the first LSM prototype to verify the LSM concept experimentally. The target application area is narrowed down from general spindle drives to dental handpieces. The high-speed operating point is set at 200 000 r/min based on state-of-the-art dental drills. For determining the loss limits of this application, a preliminary thermal model is used.

For the high-speed operating, the air spray of the dental handpiece is assumed to be utilized for cooling the machine. The maximum allowed no-load losses are calculated as

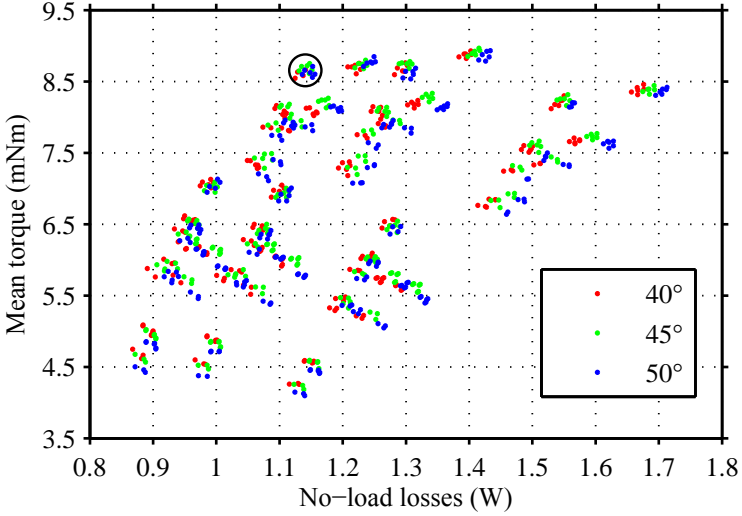


**Figure 3.12:** The effect of the shoe span on the performance of the section-type LSMs. The optimum group of machines is marked with a circle.

$$P_{\text{no-load},2} = \rho_{\text{air}} \dot{V}_{\text{air}} c_{\text{air}} (\delta_{\text{o}} - \delta_{\text{i}}) \quad (3.3)$$

where  $\rho_{\text{air}}$ ,  $\dot{V}_{\text{air}}$ , and  $c_{\text{air}}$  are the density, volume flow and specific heat capacity of air, respectively. The air temperature is  $\delta_{\text{i}}$  at the inlet and  $\delta_{\text{o}}$  at the outlet. Considering an inlet temperature of 25 °C and a flow rate of 10l/min for the air spray, the maximum allowed losses at the high-speed operating point can be calculated as 2.4 W, such that the temperature of the air exiting the handpiece does not exceed 37 °C (for ergonomic reasons).

On the other hand, as the low-speed, high-torque operation usually lasts for a limited time, only the thermal capacitance of the windings are considered for determining the maximum copper losses as

$$P_{\text{cu},1} = \frac{m_{\text{cu}} c_{\text{cu}} \Delta \delta_{\text{cu}}}{t} \quad (3.4)$$

where  $t$  is the duration of operation and  $m_{\text{cu}}$  is the total mass,  $c_{\text{cu}}$  is the specific heat capacity and  $\Delta \delta_{\text{cu}}$  is the temperature rise of the copper.

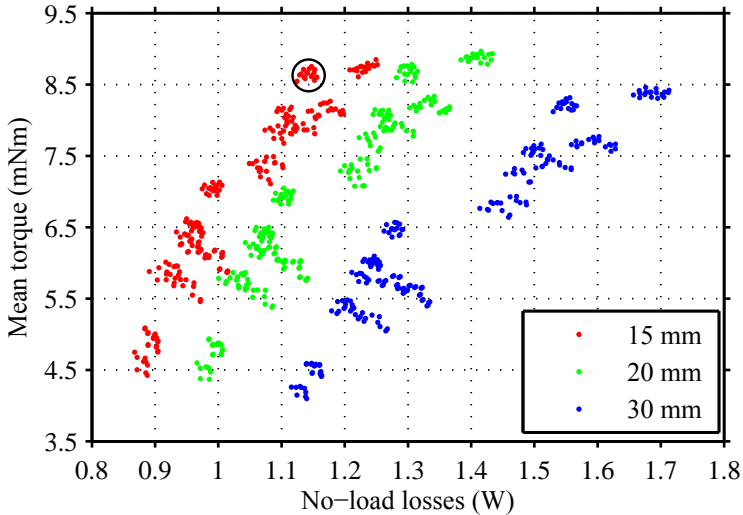


**Figure 3.13:** The effect of the stator length on the performance of the section-type LSMs. The optimum group of machines is marked with a circle.

Assuming a copper mass of 4.5 g based on the results presented in the previous section, and limiting the maximum temperature rise of the windings to 35 °C at the end of a 10 s high-torque operation, maximum copper losses are set to 6 W.

A more detailed thermal model of a dental handpiece with an LSM is shown in Chapter 8.

As the section-type LSM is shown to be capable of producing more torque than the surrounding-type LSM for given copper losses, only the section-type machines are considered. In addition to the analysis in the previous section, practical considerations regarding the construction of the machine as well as mechanical aspects of the high-speed motor design are taken into account.

In the analysis before, axially segmented arc-shaped magnets, laminated amorphous iron sheets and no retaining sleeve are considered on the rotor. Therefore, the rotor eddy-current losses are safely neglected. Even though these assumptions can be justified for a proof-of-concept analysis, they need to be revisited for the design of a hardware proto-

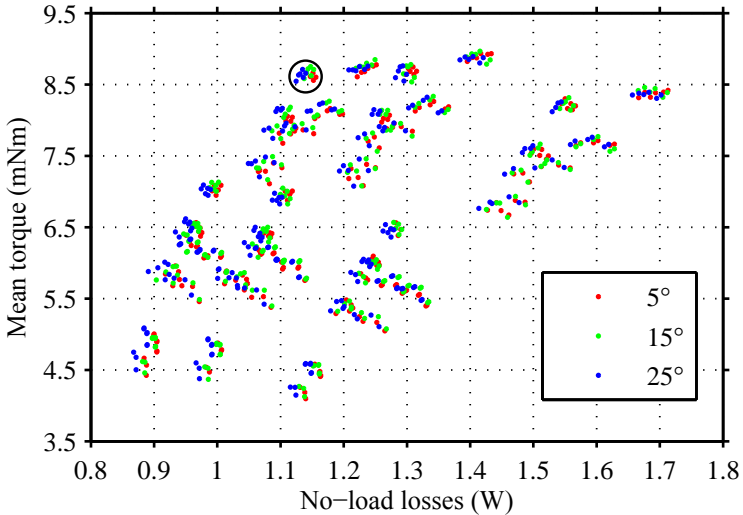


**Figure 3.14:** The effect of the shielding iron gap on the performance of the section-type LSMs. The optimum group of machines is marked with a circle.

type.

For simpler rotor construction, the arc-shaped magnets are replaced by breadloaf-shaped magnets on the rotor. The rotor core is made of a solid cobalt-iron shaft instead of laminated amorphous iron sheets in order to have a mechanically robust rotor structure.

In order to hold the magnets in their place under high centrifugal forces occurring at high speeds, a retaining sleeve is used on the rotor surface. This sleeve is a hollow titanium cylinder that is interference fitted on the magnets. The calculation of the interference fit is explained in detail Section 3.3. A rotor dynamics analysis is also carried out as the critical speeds of the rotor can be a limiting factor on the maximum achievable speed in high-speed electrical machines.

As one-piece permanent magnets and a solid cobalt-iron shaft are used in the rotor as opposed to laminated iron sheets and axially segmented permanent magnets, and as a conductive sleeve is introduced, the rotor eddy-current losses cannot be neglected anymore. Therefore, the loss models that are described previously are enhanced to calculate

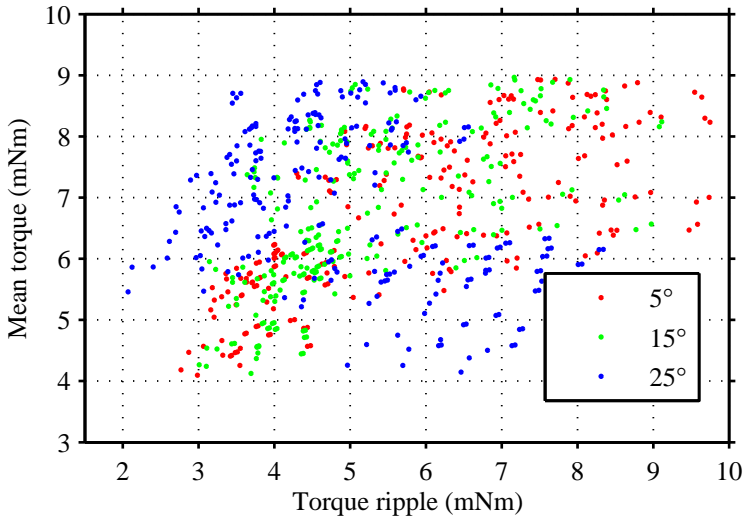


**Figure 3.15:** The effect of the shielding iron gap on the torque ripple of the section-type LSMs.

the rotor eddy-current losses. Moreover, the core loss model described earlier is adapted to take the effect of rotating fields into account, in order to calculate the losses in the stator shoe region and in the shielding iron more accurately. These modifications are explained in the following sections.

The cross-sectional view and parameter definition of the machine is shown in Figure 3.18. The parameter ranges are given in Table 3.5.

### 3.2.1 Improvements of the loss models

#### Rotor losses

Time and space harmonics of the air gap field induce eddy currents in the solid conductive bodies of the rotor in an electrical machine. In order to analyze those eddy currents accurately, a 3-D model is needed, as the eddy-current problem is a 3-D problem by its nature [28]. However, 3-D FEM simulations require much longer computational time than 2-D simulations. For that reason there have been efforts to approximate the eddy-current losses using only 2-D simulations, like in [28].

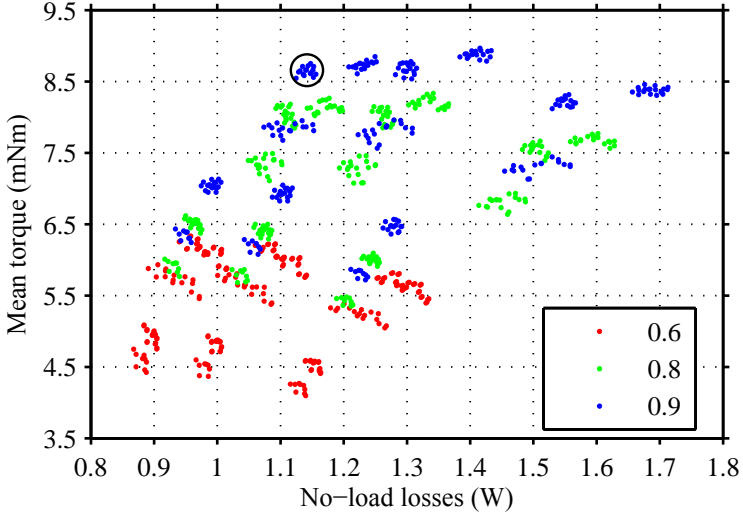


**Figure 3.16:** The effect of the magnet span on the performance of the section-type LSMs. The optimum group of machines is marked with a circle.

$w_s$	Shaft width	3.5 and 4 mm
$d_r$	Rotor diameter	6.8 mm
$w_t$	Tool neck width	8 mm
$w_h$	Tool head width	8.8 mm
$l_s$	Stator length	10, 15, 20 and 25 mm
$\tau$	Shoe span	40 and 45°
$w_l$	Leg width	0.8, 1, 1.2 and 1.4 mm
$l_a$	Active length (into page plane)	7.4 mm

**Table 3.5:** Discretization of the parameter range including fixed parameters for the first LSM prototype.

This method is developed for rectangular permanent magnets and it depends on the assumption of uniform magnetic field density over a magnet body. It calculates a fictitious electric resistivity of the permanent magnets according to their dimensions, which includes the effect of the end resistances in a 2-D model.

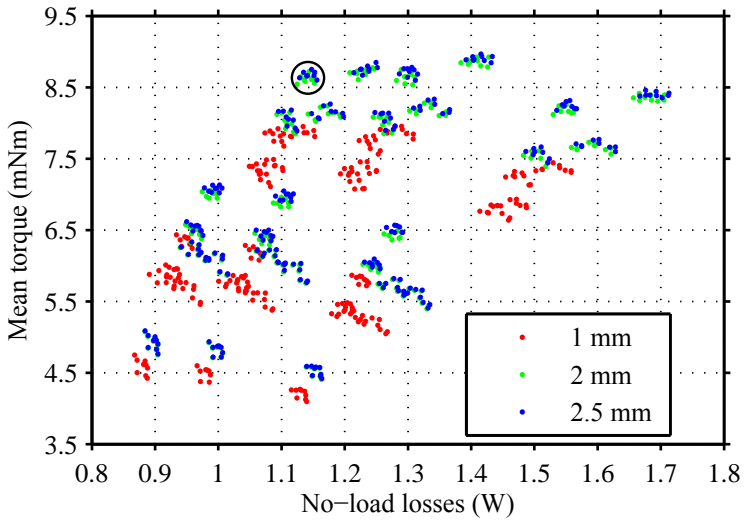


**Figure 3.17:** The effect of the magnet depth on the performance of the section-type LSMs. The optimum group of machines is marked with a circle.

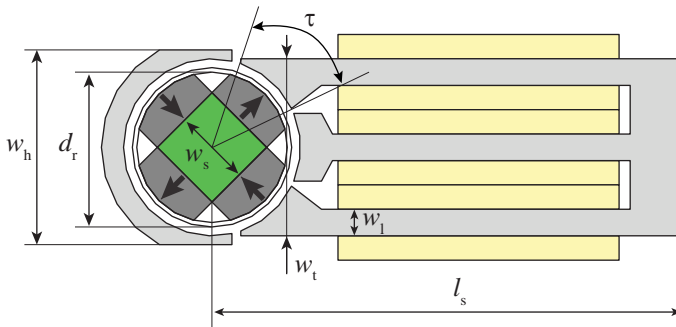


**Figure 3.18:** Cross-sectional view and parameter definition of the section-type LSM with breadloaf-shaped magnets. Dark gray color indicates permanent magnets with arrows showing the magnetization direction, light gray areas indicates the laminated core material, green region shows the solid rotor core and yellow regions show the windings.

In this work, as the armature currents are neglected at the high-speed operating point, only the no-load eddy currents<sup>4</sup> are considered in the rotor. A 2-D field solution is used to calculate the eddy currents, neglecting the end resistances of the permanent magnets. This way, the calculation is kept simple; moreover, the calculated eddy currents are expected to be larger than the real eddy currents as the end resistances are neglected. This is considered to be an additional safety factor regarding the thermal considerations, as the cooling of the rotor is poor and overheating may demagnetize the permanent magnets.

For a solid conductor in which the total current  $I_t$  is known, the current distribution can be calculated according to (3.5), where  $a_c$  is the cross-sectional area of the conductor,  $J_t$  is the total current density,  $\sigma_c$  is the conductivity of the conductor,  $A$  is the magnetic vector potential and  $J_s$  is the unknown current source component to be calculated [32].

$$\int \int_{a_c} (-\sigma_c \frac{dA}{dt} + J_s) da_c = \int \int_{a_c} J_t da_c = I_t \quad (3.5)$$

To evaluate the eddy currents induced in the rotor, (3.5) is solved with the additional condition  $I_t = 0$  in the conducting bodies of the rotor. This additional condition forces the total current in the cross-sectional area to be zero, limiting the path of the induced current within the solid body under consideration. After the current distribution is obtained, the eddy-current losses are calculated using (3.6) where  $P_{\text{eddy}}$  is the eddy-current loss in a conducting body whose conductivity is  $\sigma_c$  and volume is  $V$ .

$$P_{\text{eddy}} = \frac{1}{\sigma_c} \int_V J_t^2 dV \quad (3.6)$$

Table 3.6 gives the electrical conductivities of the permanent magnets, shaft and the sleeve used in the rotor.

### Core losses

The Modified Steinmetz Equation (MSE) [26] is used to calculate the core losses in the previous analysis. Even though it can take nonsinusoidal flux changes into account, this method considers only unidirectional fields in the magnetic core. In order to take the effect of rotating

---

<sup>4</sup>No-load eddy currents are induced in the permanent magnets as the nonuniform air gap permeability leads to a varying magnetic flux density in the magnets.

Permanent magnet	625 000 S/m [30]
Titanium sleeve	590 000 S/m [33]
Shaft	2 272 700 S/m [34]

**Table 3.6:** Electrical conductivities of the solid conductive bodies in the rotor.

fields into account and calculate the losses in the stator shoes and the shielding iron more accurately, the method presented in [35] is used for designing the first prototype. This method takes both nonsinusoidal and rotating flux effects into account, and it only needs the standard loss data (as given in Table 3.1), which are generally provided by core material manufacturers.

### 3.2.2 Simulation results

Figure 3.19 shows the mean torque generated by the machines at 6 W copper losses and their no-load losses at 200 000 r/min. The machine that generates the highest torque while generating less no-load losses than the no-load loss limit of 2.4 W is marked with a circle.

It can be seen in Figure 3.20 that below a certain stator length, the winding area is small, limiting the phase current for given copper losses; hence limiting the torque. However, after a certain stator length, a longer stator does not necessarily always mean a higher torque. This is due to the increasing stray field with increasing stator length.

Figure 3.21 shows that in the parameter space analyzed here, increasing the width of the stator legs leads to higher torque and also higher no-load losses. These results identify the leakage and the saturation of the legs as the two main limiting factors for the torque.

Furthermore, decreasing the shoe span in all cases leads to increasing torque due to the decreasing stray field, as seen in Figure 3.22.

Finally, Figure 3.23 shows the effect of the shaft width (which in turn determines the magnet thickness as the rotor diameter is fixed) on the machine performance. It is interesting to note that a bigger shaft, i.e. smaller magnets, lead to higher losses at similar torques. The reason for this can be explained by Figure 3.24, in which the effect of the shaft width on the rotor and core losses is shown. The change of the shaft width from 3.5 mm to 4 mm does not change the flux in the stator significantly (does not affect core losses), but leads to a higher

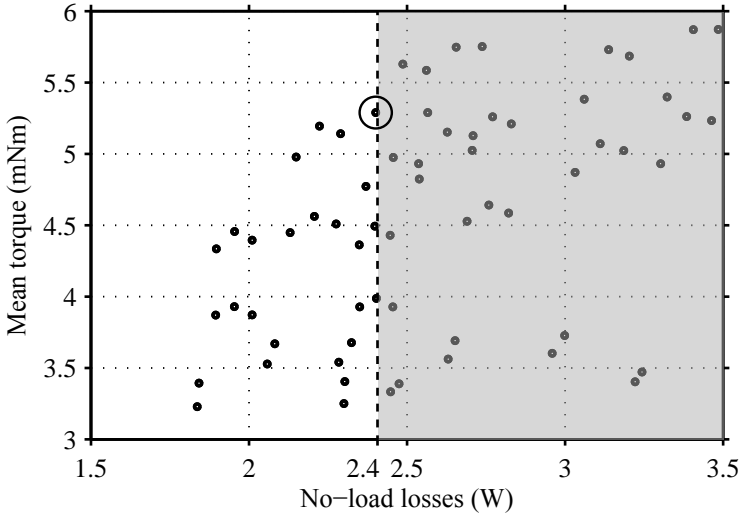


**Figure 3.19:** The performance of the analyzed machines. The no-load loss limit of 2.4W is marked, and the machine that generates the highest torque and generates less no-load losses than the limit is marked with a circle.

Rotor eddy-current losses	1.67 W
Stator core losses	0.42 W
Air-friction losses	0.3 W

**Table 3.7:** Calculated no-load loss components of the first prototype at 200 000 r/min.

overall volume of conductive bodies in the rotor, increasing the rotor eddy-current losses.

The machine marked with a circle in Figure 3.19–Figure 3.23 is selected for the first prototype. Figure 3.25 shows the dimensions of this machine.

The selected machine (Figure 3.25) generates the torque waveform shown in Figure 3.26 when driven with sinusoidal currents resulting in 6 W of copper losses. Table 3.7 lists the different no-load loss components of this machine at 200 000 r/min.

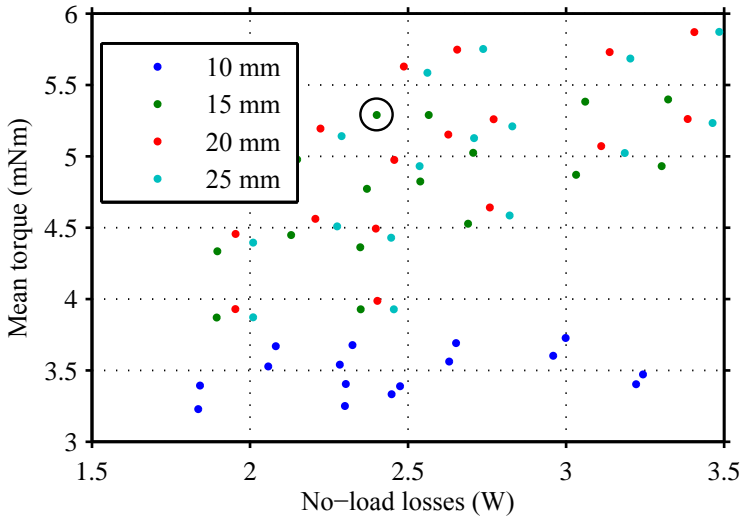


**Figure 3.20:** The effect of the stator length on the performance of the section-type LSMs.

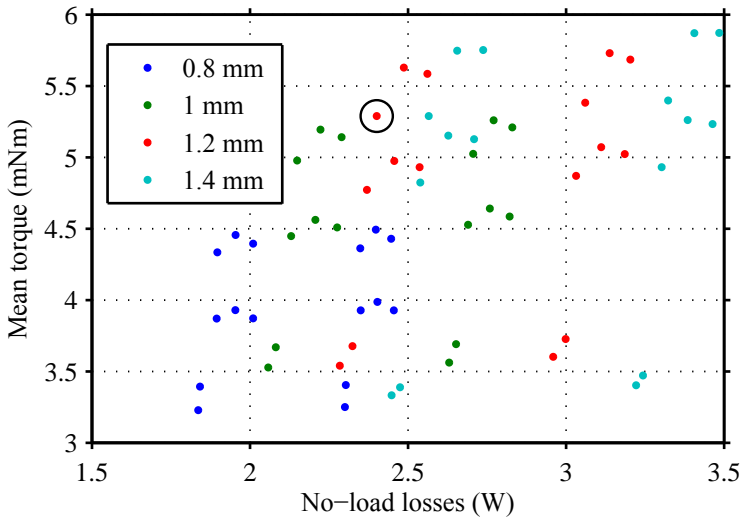


**Figure 3.21:** The effect of the leg width on the performance of the section-type LSMs.

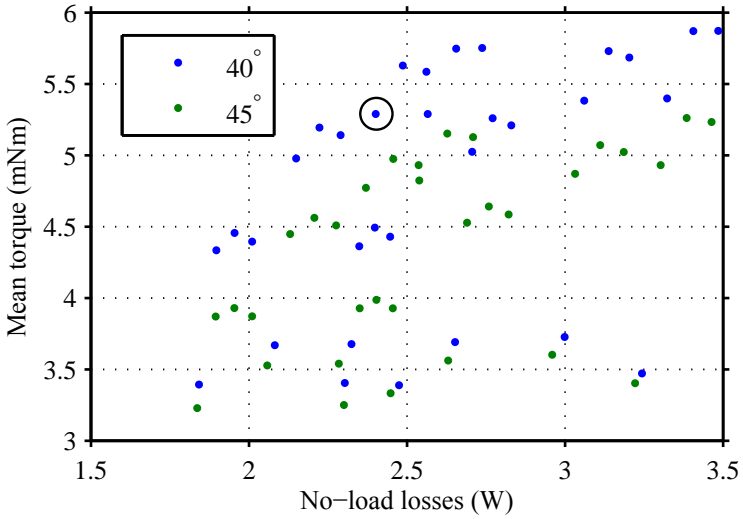


**Figure 3.22:** The effect of the shoe span on the performance of the section-type LSMs.

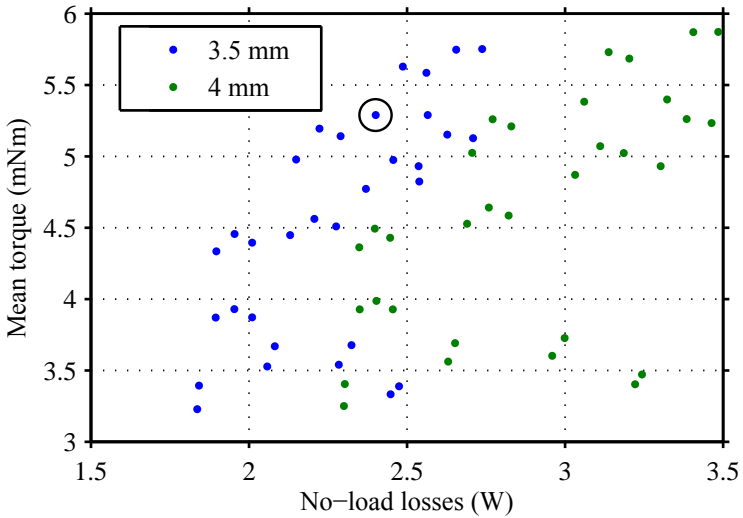


**Figure 3.23:** The effect of the shaft width on the performance of the section-type LSMs.

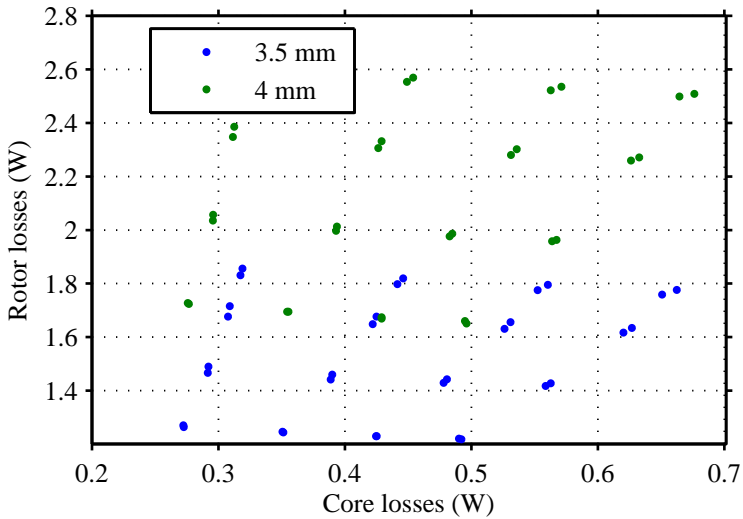


**Figure 3.24:** The effect of the leg width on the core and rotor eddy-current losses of the section-type LSMs.

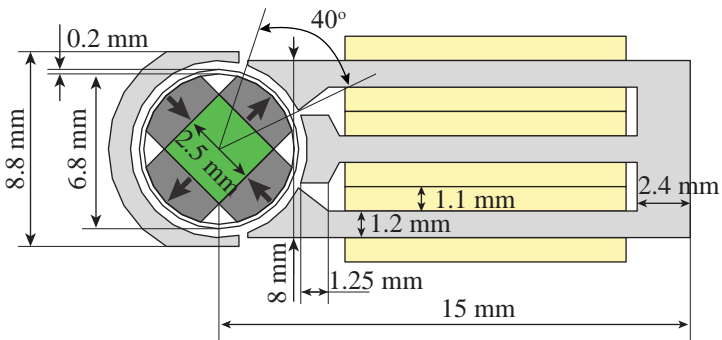


**Figure 3.25:** The LSM design selected for the first prototype. The lateral stator and the shielding iron are made of amorphous iron (Table 3.1). NdFeB magnets with remnant flux density of 1.1 T are used in the rotor. Grade 5 titanium [33] and cobalt-iron [34] are used for the sleeve and the shaft, respectively. The active length (into page plane) of the machine is 7.4 mm.

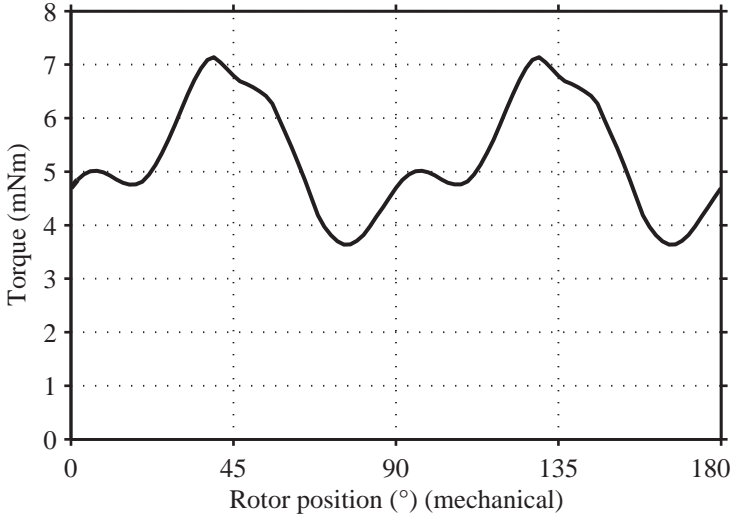


**Figure 3.26:** Torque of the selected machine over the rotor position when driven with three-phase  $120^\circ$  phase shifted sinusoidal currents (peak 165 Ampere – turns) resulting in 6 W of copper losses. The average value of the torque is 5.28 mNm.

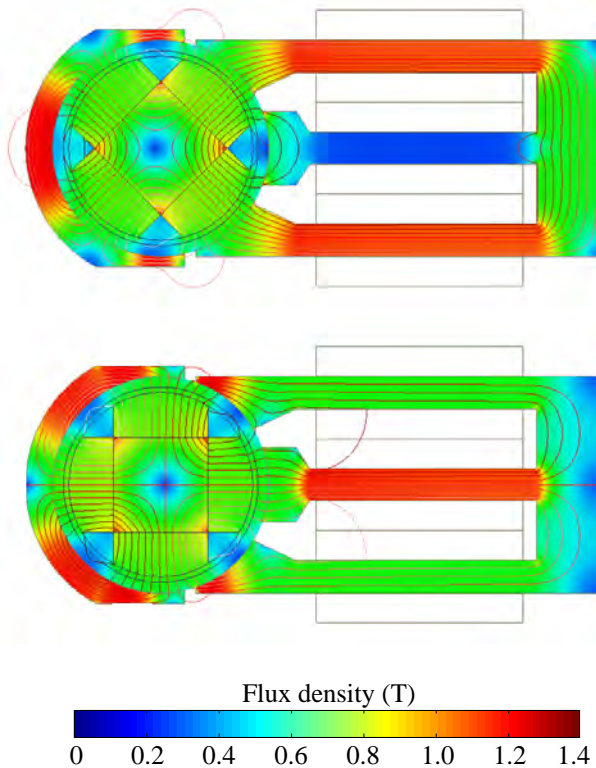
Figure 3.27 shows the flux distribution of the selected machine for the first prototype, for two rotor position that are mechanically  $45^\circ$  apart. It can be seen that even at no-load the stator legs carrying the rotor flux are close to saturation. Figure 3.28 shows the flux distribution in the machine for the same rotor positions but at full load (6 W copper losses), where the effect of the stray flux is visible.

Figure 3.29 shows the eddy currents induced in the rotor as calculated by the 2-D FEM analysis while the rotor rotates counter clockwise with 200 000 r/min at no-load.

## 3.3 Hardware realization

### 3.3.1 Rotor stresses

Sintered rare-earth permanent magnets have low tensile strengths which makes them susceptible to mechanical failure under the centrifugal



**Figure 3.27:** 2-D FEM simulation results showing the flux lines and the flux density for the first prototype at no-load, for two different rotor positions. The no-load flux causes partial saturation of the stator core.

forces acting on them at high rotational speeds. Furthermore, the magnets are glued on the rotor core; therefore, a retaining sleeve is used to fasten and protect the permanent magnets [16], [36].

Retaining sleeves can be made of titanium alloys [8] or composite structures such as carbon fiber reinforced polymers [37], [38]. Even though they offer very high mechanical strength and low densities, the main drawback of using carbon fibers is their negligible thermal expan-

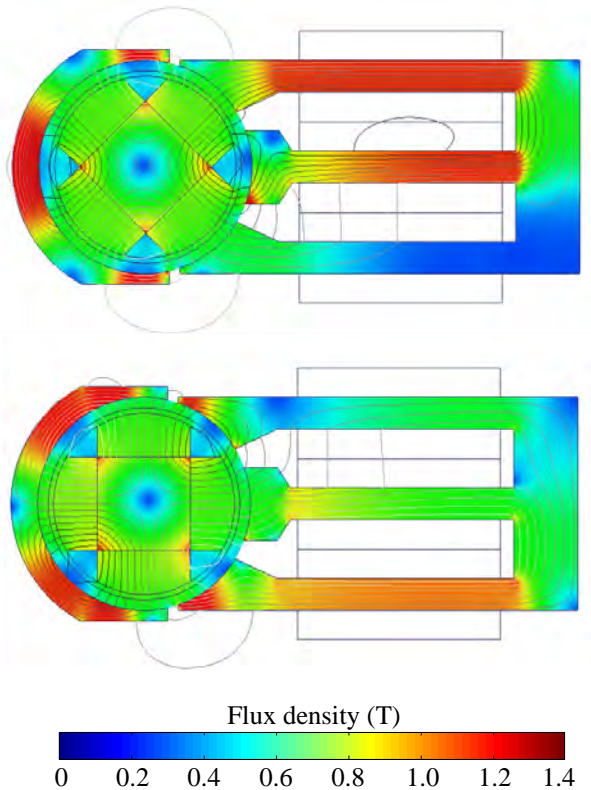


**Figure 3.28:** 2-D FEM analysis results showing the flux lines and the flux density for the first prototype at full-load, for two different rotor positions.

sion in contrast with that of permanent magnets; therefore, additional stresses are expected in the rotor at elevated temperatures. Furthermore, composite sleeves have lower thermal conductivity compared to metallic sleeves, leading to a worse cooling of the permanent magnets. The thermal behavior of different sleeves is analyzed in [37].

The selection of the sleeve material is however not only a mechanical or thermal problem, but also the effects of the sleeve on the electromagnetic behavior of the machine need to be analyzed. For example, [39]

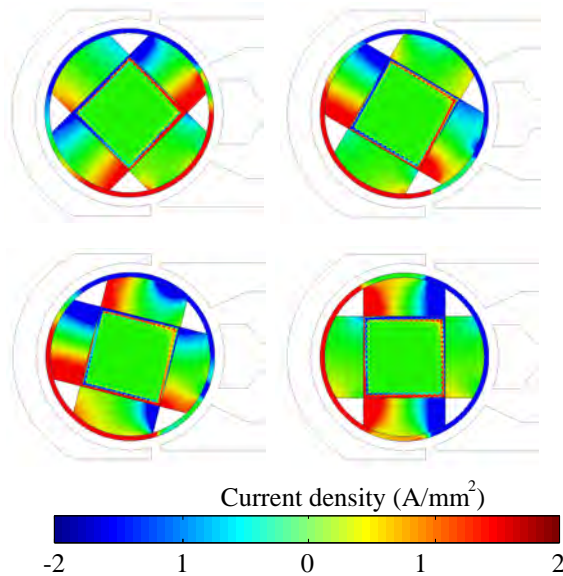


**Figure 3.29:** Eddy currents induced in the conductive bodies of the rotor while it is rotating counter clockwise at 200 000 r/min under no-load conditions. The angular displacement between the images is 15° (mechanical).

studies the effects of the sleeve material on the rotor losses.

In this work, rotors with titanium as well as composite sleeves are built and tested. Aramid, carbon and glass fibers are utilized for different composite sleeves.

### Titanium sleeve

The interference fit of the titanium sleeve ensures an initial tension (preload) on the magnets, counteracting the centrifugal forces. Such an interference fit can be realized either by thermal expansion and/or contraction, by force or by a combination of these two.

Analytical models for calculating the stresses in rotors with a cylindrical magnet and a hollow cylindrical sleeve around it are shown in [8] and [16]. However, in this work a structural mechanical FEM analysis

	Magnet	Sleeve	Shaft
Young's modulus (GPa)	140	115	205
Poisson's ratio	0.28	0.35	0.3
Density (kg/m <sup>3</sup> )	7700	4430	8120
Tensile strength (MPa)	75	895	350
Compressive strength (MPa)	1100	-	-

**Table 3.8:** Mechanical properties of the materials of the permanent magnet, titanium sleeve and the cobalt-iron shaft.

is employed in order to capture the stresses in the breadloaf shaped magnets and in the sleeve accurately.

The minimum amount of interference is calculated such that throughout the whole operating range there is pressure at the magnet-shaft and sleeve-magnet interfaces. This ensures a low eccentricity by guaranteeing that the sleeve and the magnets do not lift off. Furthermore, the von Mises stresses in the sleeve have to be smaller than the tensile strength of titanium [8].

Figure 3.30(a) shows the deformation (60 times up-scaled) and the von Mises stresses in the rotor for a sleeve radial thickness of 0.2 mm, a diametrical interference of 12  $\mu\text{m}$  and a rotational speed of 200 000 r/min. Figure 3.30(b) shows the stresses in the x and y directions  $\sigma_x$ ,  $\sigma_y$  when the rotor is at standstill. Figure 3.30(c) shows the same components of stress at a rotational speed of 200 000 r/min. It can be seen that the maximum von Mises stresses occur at the edges of the sleeve, but it is lower than the tensile strength of titanium. A negative stress at the magnet-shaft ( $x = 1.8$  mm) and sleeve-magnet ( $x = 3.4$  mm) interfaces ensure no lift-off. The glue at the magnet-steel interface is not modeled separately, and it acts as an additional safety factor in this case. Figure 3.31 shows a photograph of a rotor with a titanium sleeve. The mechanical properties of the sleeve, magnet and shaft materials are given in Table 3.8.

### Composite sleeve

Composite sleeves are used commonly in surface-mounted permanent-magnet electrical machines designed for relatively high speeds. Carbon-fiber is generally the preferred material as it offers a very high mechanical strength, which leads to sleeves with small radial thickness [37].

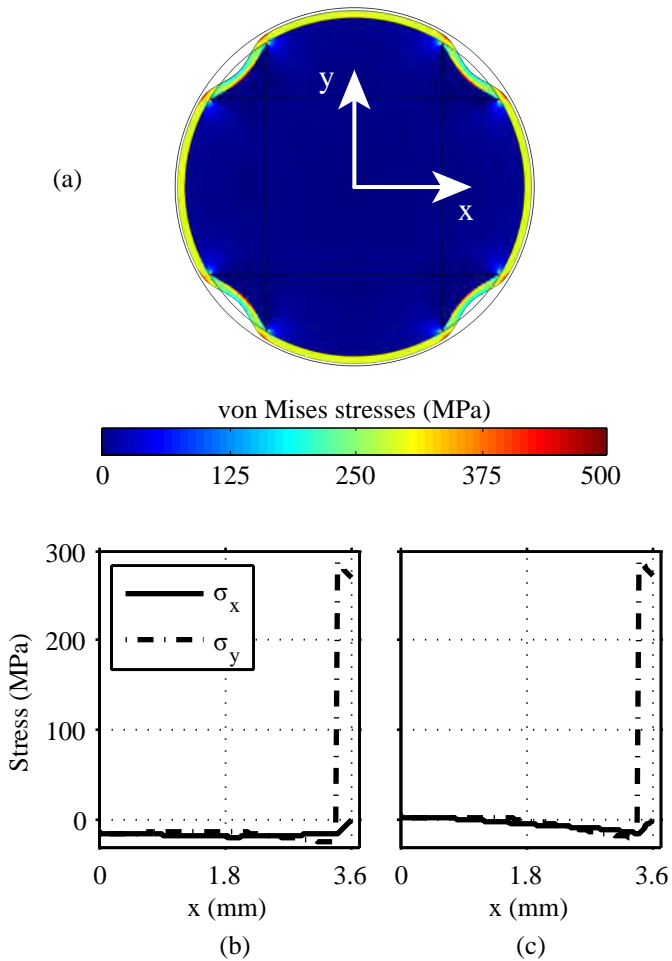


**Figure 3.30:** Results of 2-D FEM analysis showing the mechanical stresses in the rotor. The titanium sleeve has a radial thickness of 0.2 mm and a 12  $\mu\text{m}$  diametrical interference fit is considered. (a) von Mises stresses and 60 times amplified deformation while rotating at 200 000 r/min. (b) Stresses in the x and y directions at standstill. (c) Stresses in the x and y directions at 200 000 r/min.

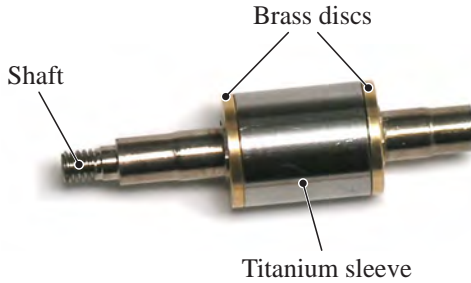


**Figure 3.31:** Photo of a rotor with titanium sleeve. The brass discs cover the axial faces of the permanent magnets and they can also be used for balancing the rotor. The total axial length of the shaft is 26 mm.

Composite sleeves are usually produced such that their inner diameter is slightly smaller than the magnet diameter, and they are mounted on the rotors either by forcing or shrink fitting [16]. As described in the previous section, the amount of interference fit has to be selected carefully in order to guarantee reliable operation throughout the whole speed range and avoid mechanical failure. This is, however, difficult due to the relatively large production tolerances of the permanent magnets in small electrical machines. The layer of glue between the magnet and the shaft contributes further to the uncertainty of the outer dimensions of individual magnets. Therefore, in order to ensure that the magnets have a round outer surface with a defined diameter, a precise grinding step is required between gluing the magnets on the shaft and mounting the sleeve on the magnets.

When a composite sleeve is used, this problem can be overcome by winding the sleeve on the magnets that might have slightly different outer radii due to the production tolerances. The unbalance of the rotor can be fixed by balancing the rotor as the last step of production, which is also recommended for rotors with titanium sleeves due to the unbalance that may be originating from various other manufacturing tolerances. The winding of the composite sleeve on the rotor is shown in Figure 3.32, where  $F_c$  is the centrifugal force, and  $F_s$  is the force in the sleeve. A positive  $F_h$  force means that the magnet is applying pressure on the shaft and there is no lift-off.

Firstly, one end of a roving consisting of up to thousands of fibers is fixed on the rotor. The roving is impregnated by passing through an epoxy bath, and it is wound on the rotor which is fixed on its axis of rotation and rotated by the help of a winding machine. A preload connected on the other end of the roving provides a defined tension on the roving.

Assuming a weightless sleeve and neglecting the expansion of the magnets and the shaft due to centrifugal forces, one can write the force balance as

$$F_c + F_h = 2 \cdot F_s \cos \beta. \quad (3.7)$$

The tensile stress  $\sigma_s$  in the sleeve can be calculated depending on the radial sleeve thickness  $t_{sl}$  and the axial length of the magnets  $l_a$  as

$$\sigma_s = \frac{F_s}{t_{sl} l_a}. \quad (3.8)$$

Tensile stress can also be written in terms of the preload mass  $m_{pre}$ , gravitational acceleration  $g$ , and the cross-sectional area of the roving  $a_{rov}$  as

$$\sigma_s = \frac{m_{pre} g}{a_{rov}}. \quad (3.9)$$

Using these equations the minimum mass of preload can be calculated in order to avoid the lift-off of the magnets. The tensile stress in the sleeve has to be smaller than the tensile strength of the material, and a safety factor is usually used to provide a safety margin. As an example, for the breadloaf-shaped magnets of the first prototype, a preload of 0.8 kg ensures a positive  $F_h$  up to 200 000 r/min when a carbon-fiber sleeve with 0.2 mm radial thickness is used. If the roving consists of 1000 fibers each with 7  $\mu$ m diameter, the tensile stress in the sleeve is 210 MPa, considerably smaller than the tensile strength of the material which is 950 MPa.

Figure 3.33(a) shows a rotor with an aramid sleeve while the sleeve is being wound. The same rotor is seen in Figure 3.33(b) after it has been ground down to the final outer diameter. A rotor with a glass fiber sleeve (without bearings) and another one with a carbon fiber sleeve are shown in Figure 3.34. Table 3.9 shows the properties of the carbon, aramid and glass fibers used for building the composite sleeves.

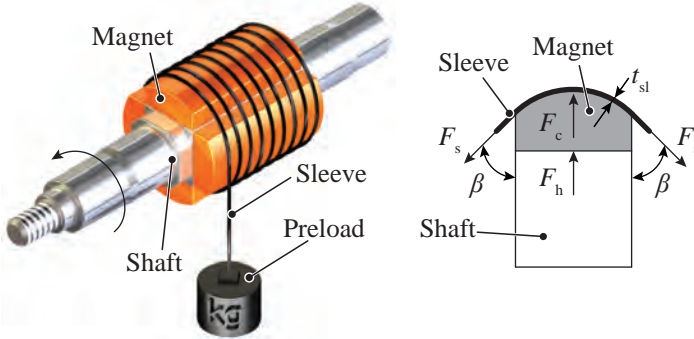


**Figure 3.32:** Winding process for the composite sleeve and the parameters used for dimensioning the sleeve.

	Carbon	Aramid	Glass
Linear density of roving (g/km)	67	805	2400
Fiber diameter ( $\mu\text{m}$ )	7	12	15
Tensile strength (raw fiber) (MPa)	3950	2880	3952
Tensile strength (composite) (MPa)	950	790	590
Young's modulus (raw fiber) (GPa)	283	100	73
Density (raw fiber) ( $\text{kg}/\text{m}^3$ )	1770	1450	2540

**Table 3.9:** Properties of the carbon, aramid and glass fibers used for building the composite sleeves [40].

### 3.3.2 Rotor dynamics

In electrical machines, the critical speeds of the rotor can be a limiting factor on the maximum achievable speed, as any unbalance on the rotor would excite vibrations whose amplitudes get bigger at these speeds [8]. Therefore, the rotor dynamics of a setup where the rotor of the LSM is coupled with a different drive machine is analyzed using a 3-D FEM model. The reason for having this coupling and its operation is explained in detail in Chapter 4.

Both the rotor of the LSM and of the drive machine are mounted in their respective housings using two single-row radial deep-groove ball bearings ULZ4008 [41] each. Figure 3.35 shows the results of the 3-D FEM rotor dynamics analysis. It can be seen that the first bending

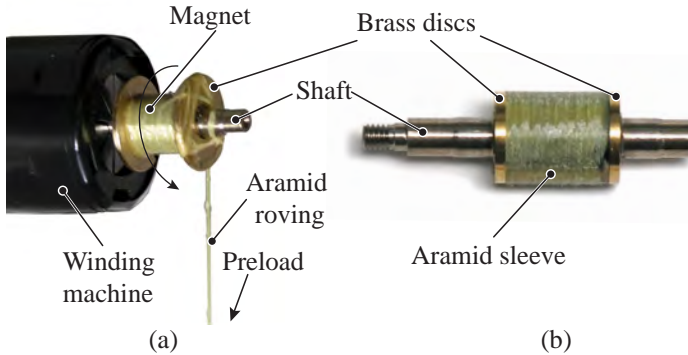


**Figure 3.33:** Photos of a rotor with an aramid sleeve. (a) Winding the aramid roving. (b) Rotor after machining down to the final outer diameter.

mode which limits the speed occurs at 312 000 r/min, which is higher than the rated speed of 200 000 r/min. The first two rigid-body modes, on the other hand, occur below the rated speed. However, the vibrations at these frequencies can be damped by a suitable bearing configuration, and the rotor can operate between the second and the third critical speeds [8], [16]. Therefore, 0.8 mm thick plastic o-rings with outer diameters of 8 mm are used with the ball bearings to limit the effect of these vibrations. The o-rings also make the construction less sensitive to misalignments when coupling the drive machine to the lateral-stator machine.

### 3.3.3 Stator construction

The lateral stator and the shielding iron are manufactured out of a larger laminated block of amorphous iron (Table 3.1) using electric discharge machining. Figure 3.36 shows such a block after the stator parts are machined out of it. The lateral stator can be machined as one piece or each leg can be machined separately. The former option leads to a more difficult winding manufacturing, but the alignment of the stator is simpler. The latter option leads to easier winding of the phase coils at the expense of more challenging alignment of the stator parts.

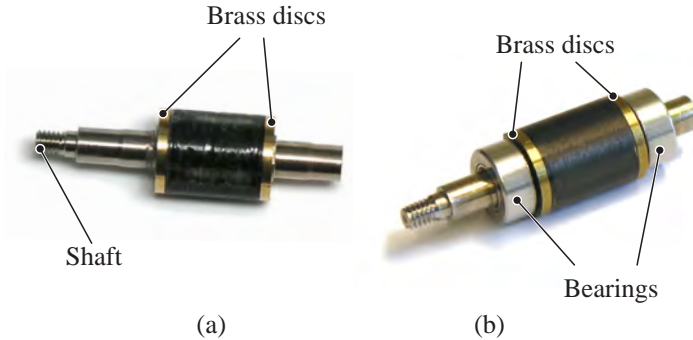


**Figure 3.34:** Photos of two rotors with composite sleeves. (a) Rotor with glass fiber. As the glass-epoxy structure is see-through, the magnets that are coated with a dark coating material and the epoxy-filled space between the magnets are visible through the sleeve. (b) Rotor with carbon fiber sleeve. Bearings are mounted after the sleeve is machined down to its correct diameter. The outer diameter of the bearings is 6.35 mm.

### 3.3.4 Positioning of the stator parts

The stator of the section-type LSM consists of two parts: the lateral stator and the shielding iron. These two parts need to be positioned correctly with respect to each other and to the rotor, for proper operation of the machine. The positioning is ensured by the machine case which consists of two parts, a plastic chamber surrounding the lateral stator and the shielding iron, and an aluminum housing built around this plastic chamber as shown in Figure 3.37.

The plastic chamber needs to fulfill the following requirements:

- ▶ Nonconductive, hence no eddy-current losses are caused by the rotor flux or the stray flux between the stator shoes.
- ▶ Nonmagnetic, such that the magnetic air gap of the design can be maintained.
- ▶ Precisely manufacturable, in order to position the stator and the rotor correctly with respect to each other.

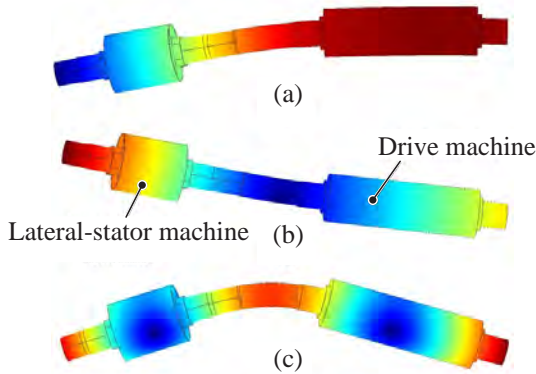


**Figure 3.35:** Critical speeds of the LSM coupled to an external drive machine. (a) First rigid-body mode at 2.27 kHz, 136 000 r/min; (b) second rigid-body mode at 2.53 kHz, 152 000 r/min; and (c) first bending mode at 5.2 kHz, 312 000 r/min. Blue shows no displacement, red shows maximum displacement. A stiffness of 0.4 MN/m is assumed for the bearing and o-ring combination.

- Mechanically strong, in order to withstand the forces attracting rotor and stator parts together.

Tight tolerances in the range of 0.1 mm and layer thicknesses of 0.05 mm can be achieved using Stereolithography-type 3-D printing. Therefore, this method is used for manufacturing the plastic chamber in order to fulfill the design requirements listed above. The liquid photopolymer ProtoTherm 12120 [42], which produces strong, high-temperature tolerant and water-resistant parts, is chosen as the material.

The plastic chamber is made of four pieces, facilitating the positioning of the lateral stator and the shielding iron. In Figure 3.38(a) an illustration of the plastic chamber is shown. For simplicity, only the half section views of part 3 and part 2 of the plastic chamber and only one leg of the lateral stator are depicted. It can be seen that part 3 of the plastic chamber is designed in a way that the stator legs would fit in and be aligned with respect to each other. Part 2 positions the

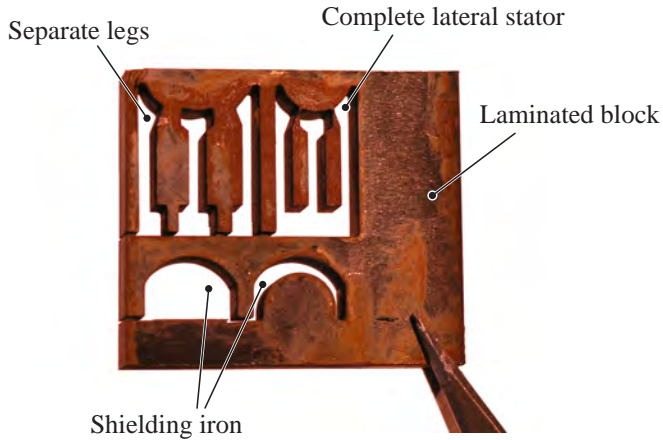


**Figure 3.36:** Photo of the laminated block of amorphous iron after stator parts are machined out of it. The lateral stator can be manufactured as one piece or each leg can be machined separately. The size of the block in the photo is approximately 35 mm x 30 mm x 10 mm.

shielding iron with respect to the stator legs. Part 1 and part 4 can be taken out to remove the lateral stator and the shielding iron without changing the air gap geometry, which is formed by the circular faces of part 3 and part 2. This allows for the segregation of the no-load losses (see Chapter 4). The winding ends are taken out through the empty space on part 4. A photo of the plastic chamber parts can be seen in Figure 3.38(b).

The housing around the plastic chamber aligns the plastic chamber (and therefore the stator) with respect to the rotor. The aluminum parts are designed in a way that it is possible to take the plastic chamber out and put it back to its position precisely, without disassembling the bearings. A photo of the machine case consisting of the plastic chamber and the aluminum housing can be seen in Figure 3.39.

The LSM is not a symmetric machine by its nature. Because of this asymmetry, there is always a force pulling the rotor and the stator parts towards each other. This force depends on the rotor position and

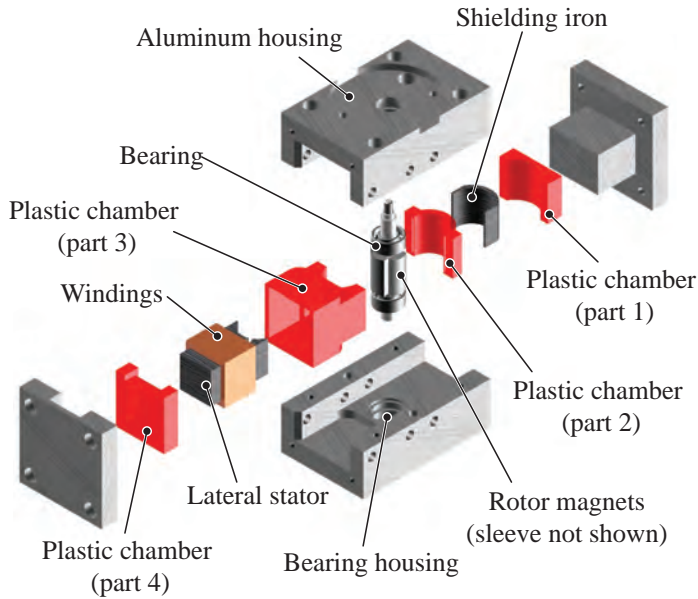


**Figure 3.37:** Illustration of the LSM in the complete housing including the 3-D printed plastic chamber (red parts) and the aluminum housing around it.

the stator currents. It has a peak value of 7.1 N for the shielding iron, 2.5 N for the rotor and 6.8 N for the lateral stator in the worst case, according to FEM analysis. Because of these forces, the lateral stator and the shielding iron apply forces on the plastic chamber, stressing its parts facing the air gap. The stresses induced in the plastic chamber parts due to these forces need to be analyzed to avoid any mechanical failure of the 3-D printed parts. Especially the walls of part 2 and part 3 facing the air gap are prone to mechanical stresses as these faces are only 0.2 mm thick in order to maintain a small magnetic air gap.

In Figure 3.40, the calculated stresses and the displacement of the plastic chamber are shown. The maximum value of the von Mises stress of 2.5 MPa is far below the tensile and flexural strengths of the plastic material, which are 77 MPa and 103 MPa respectively [42].

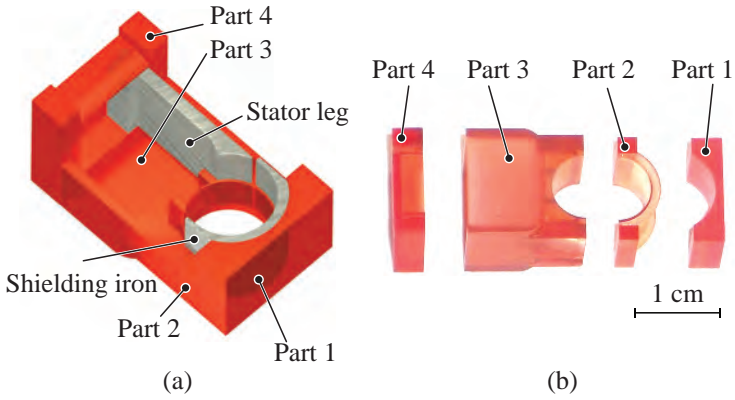


**Figure 3.38:** (a) Illustration and (b) photo of the four parts of the plastic chamber.

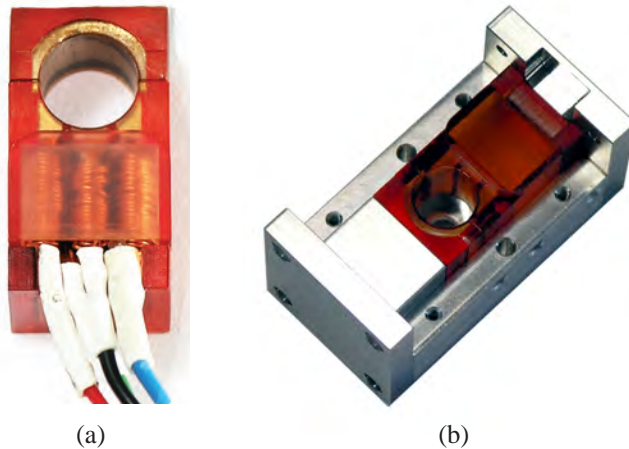


**Figure 3.39:** Photos of the first prototype. (a) Lateral stator and shielding iron in the plastic chamber. The star point of the LSM is accessible, therefore there are four cable connections to the stator. (b) Plastic chamber in the aluminum housing.

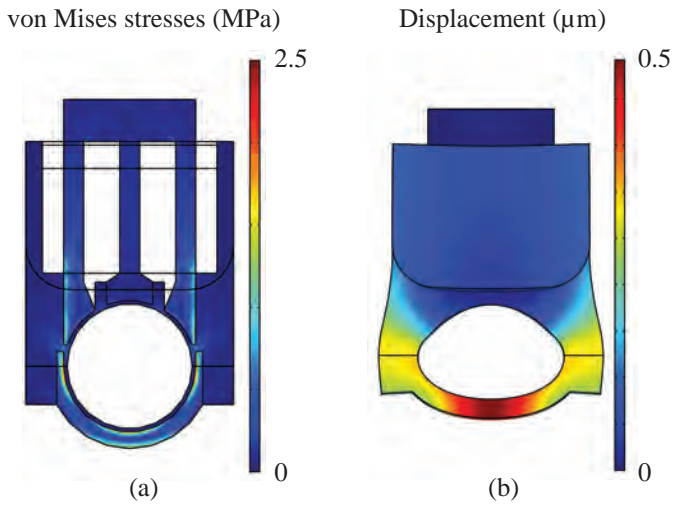


**Figure 3.40:** Results of 2-D FEM analysis showing (a) the von Mises stresses and (b) the displacement of the plastic chamber due to the magnetic pull between the rotor and the stator. The deformation is 3500 times magnified.

## Chapter 4

# Experimental verification of the machine design

In this thesis, the operation range of a general micro-machining application is summarized by two operating points (cf. Figure 2.3): a low-speed, high-torque operating point and a high-speed, low-torque operating point. It has also been shown that the speed dependent losses such as the rotor eddy-current, air-friction and stator core losses can be neglected at the low-speed operating point and only the copper losses in the windings are responsible for the heating of the machine. Therefore, at this operating point the speed can be assumed to be zero; hence, this operating point can be considered as the zero-speed, high-torque operating point. On the other hand, the torque and the copper losses can be neglected at the high-speed, low-torque operating point; therefore, this operating point can be considered as the high-speed, no-load operating point.

In the previous chapter, the machine design is carried out considering these two operating points. This chapter deals with the design of a test bench that can evaluate the performance of the machine at these two operating points, in order to verify the design procedure. Two separate test setups are developed, one measuring the torque of the LSM at standstill and the other measuring the no-load losses at higher speeds.

In the standstill torque measurement setup, a bearingless configuration is designed, and the torque is measured on the stator side with the rotor fixed in a given position. This corresponds to evaluating the ma-

chine performance in the zero-speed, high-torque operating point. As the electromagnetic torque is measured without the bearing friction, a direct verification of the FEM analysis is possible.

In the high-speed loss measurement setup, deceleration tests are used to measure the total no-load losses. This corresponds to the evaluation of the LSM in the high-speed, no-load operating point. Moreover, a method is proposed for the separation of the mechanical losses from the electromagnetic losses, which again is an important step towards the verification of the electromagnetic design in small, high-speed electric motors.

## 4.1 Standstill torque measurement

The instantaneous torque  $T$  of a permanent-magnet synchronous machine depends on the rotor position  $\theta$  and the stator currents  $i_a$ ,  $i_b$ ,  $i_c$  as

$$T = f(i_a, i_b, i_c, \theta). \quad (4.1)$$

The static torque measurement setup is shown in Figure 4.1 using a simplified diagram. In this setup, the rotor is fixed to a ground plate using a rotational positioning device, by which the rotor's angular position  $\theta$  can be adjusted and fixed. The active parts of the stator (lateral stator, shielding iron and windings) which are held together by the plastic chamber and the aluminum housing are fixed to the ground plate via the piezoelectric torque transducer 9329A from Kistler [43]. The torque transducer is connected to an oscilloscope through the charge amplifier 5011B, also from Kistler [44].

Once the parts holding the rotor and stator are positioned such that rotor is centered in the stator bore - where it will be during normal operation with the bearings installed - the stator reaction torque is recorded along with instantaneous stator currents for each rotor position. Using this data, the torque function in (4.1) can be recreated.

The advantage of this configuration is the ability to measure the electromagnetic torque directly on a bearingless configuration, eliminating any disturbances introduced by the bearings. Consequently, FEM simulations can be verified directly for different load conditions.

Figure 4.2(a) shows a photograph of the torque measurement setup, before the rotor is lowered into the stator bore to its correct position

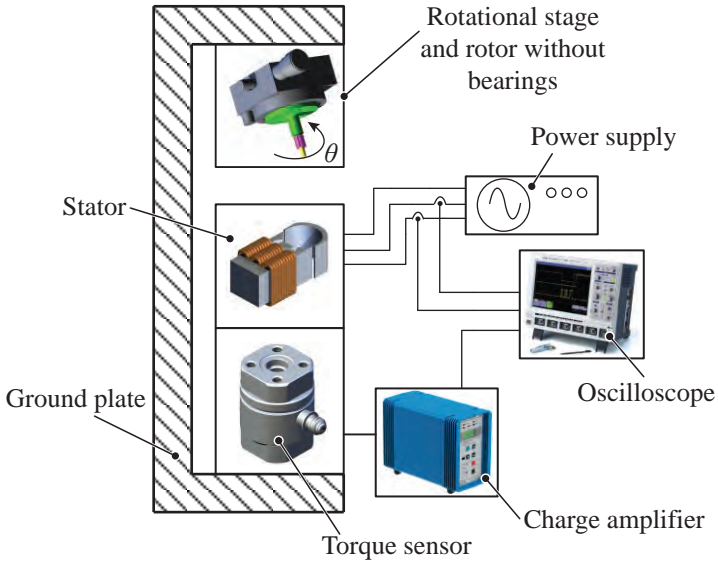


**Figure 4.1:** Block diagram of the static torque measurement setup. The housing containing the stator is mounted on a piezoelectric torque sensor that is connected to an oscilloscope through a charge amplifier. The rotor is held in the stator bore without bearings and a rotational positioning stage is used to adjust and fix the rotor's angular position. The torque is recorded for different combinations of rotor position and phase currents.

for the measurements. Figure 4.2(b) shows a cross-sectional view of the torque measurement setup with the rotor at its correct position for the measurements.

As the rotor is not supported by bearings in the torque measurement setup, the effect of the lateral magnetic pull is investigated using a 3-D FEM model. Figure 4.3 shows the result of this analysis. The maximum displacement occurs at the lower end of the rotor, but the total displacement is only  $2.5 \mu\text{m}$  under the worst-case magnetic pull. The highest value of von Mises stresses in this case is less than 10 MPa, well below the strength of all the materials used in the setup.

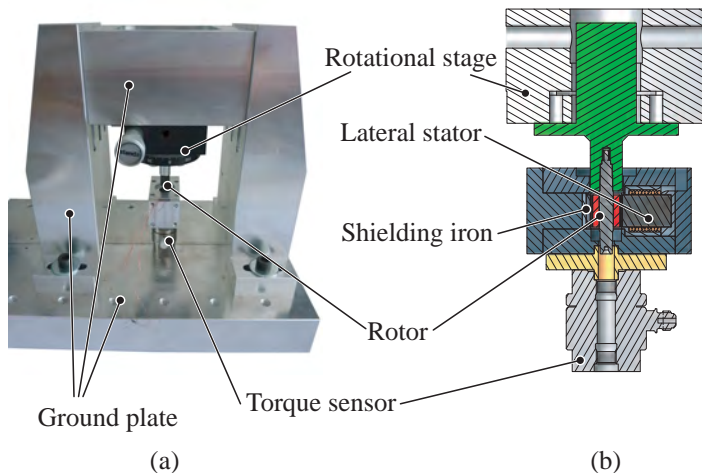


**Figure 4.2:** A photo and a cross-sectional view of the static torque measurement setup. In the photo the rotor is visible. For measurements the rotor is inserted in the stator bore as shown in the cross-sectional view.

## 4.2 No-load loss measurement

The no-load losses in an electrical machine are mechanical losses (air- and bearing-friction losses) and electromagnetic losses (rotor eddy-current losses, stator core losses and proximity losses caused by the no-load stray flux in the windings). Using the no-load loss measurement setup described in this section, those losses can be measured and segregated. In [4], the torque of an electrical machine is calculated by accelerating the machine and recording the angular position according to (4.2), where  $T_m$  is the total torque applied on the shaft,  $I$  is the axial moment of inertia of the rotor,  $\omega_m$  is the angular speed of the rotor and  $t$  is the time

$$T_m = I \frac{d\omega_m}{dt}. \quad (4.2)$$

Likewise, if the machine is first accelerated to a certain speed and then the drive power is cut off, the braking torque caused by the no-load

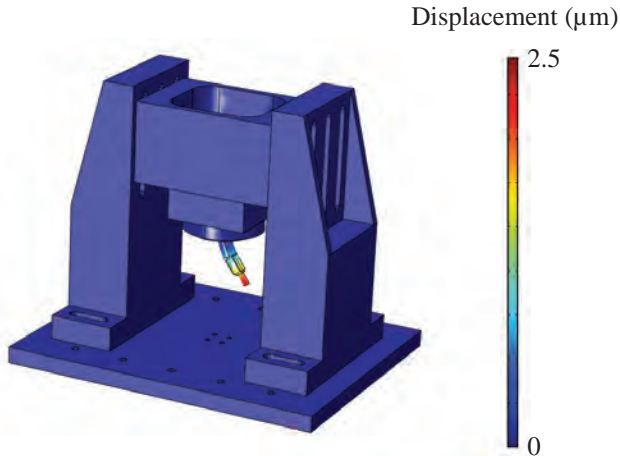


**Figure 4.3:** 3-D FEM analysis results showing the displacement of the rotor in the torque measurement setup. The deformation is 7500 times magnified. As the rotor is not fixed by bearings, the magnetic pull acting on the rotor leads to deformation; however, the deformation at the worst case is less than  $2.5 \mu\text{m}$ .

losses can be calculated using the moment of inertia and the deceleration profile of the machine. Using this deceleration test, the total no-load losses in a machine can be measured as a function of speed. However, different components of the total no-load losses cannot be separated.

In [45], a different method is proposed for measuring the losses of a permanent-magnet machine. A dummy rotor, which has identical geometry to the original rotor is built, but with unmagnetized permanent magnets. Using this dummy rotor, electromagnetic losses and the mechanical friction losses are separated. However, the bearing friction losses depend strictly on the preload, whose variation is hard to avoid or control while assembling the test bench or coupling the machine under test to a drive machine. This brings an uncertainty on the contribution of the bearing losses to the total no-load losses. This uncertainty can not be neglected in high-speed, low-power machines.

To separate the electromagnetic losses from the total no-load losses, a different method is proposed in this work. This method consists of

running deceleration tests with and without the lateral stator and the shielding iron.

In Figure 4.4 the high-speed loss measurement setup is explained with a block diagram. Figure 4.5 shows a photo of the same measurement setup. A commercial 100 W, 500 000 r/min electrical machine [46] is used as a drive machine to accelerate the LSM to a desired speed. Then, the drive power is cut off, and the back EMF of the drive machine is recorded with an oscilloscope during deceleration. The speed is calculated using the back EMF. With the speed and moment of inertia known, the total no-load losses of the drive machine and the LSM can be calculated. After running a deceleration test on this setup, the housing of the test bench is opened on both sides to take the stator and the shielding iron out. Removal of the lateral stator can be seen in Figure 4.5(b). As the bearings are not disassembled, the preload and therefore the friction losses of the bearings do not change. As seen in Figure 4.6, the plastic chamber ensures that the air gap geometry stays the same; therefore, the air-friction losses are also the same in the setups with and without the lateral stator and the shielding iron.

The aluminum housing described earlier is replaced by a plastic housing of the same geometry for the deceleration tests as seen in Figure 4.4, in order to avoid any additional eddy-current losses when the lateral stator and the shielding iron are taken out. A deceleration test on this setup gives the total no-load losses of the drive machine plus only the mechanical losses of the LSM. Accordingly, the electromagnetic losses of the LSM can be extracted. Furthermore, the no-load proximity losses can be measured in a similar way, by running deceleration tests with and without the windings around the stator legs.

### 4.3 Measurement results

As explained above, the rotor is fixed at different angles and three-phase, 120° phase shifted sinusoidal currents are injected into the windings for the standstill torque measurement, and the torque is recorded along with the currents. As the windings are Y-connected with an open star point, the currents are measured only at two phases. The results of this measurement as well as 2-D FEM simulations are shown in Figure 4.7 for full load and two rotor positions that are 20° apart. It can be seen that the 2-D simulations and measurements yield similar results, which verifies the 2-D FEM models.

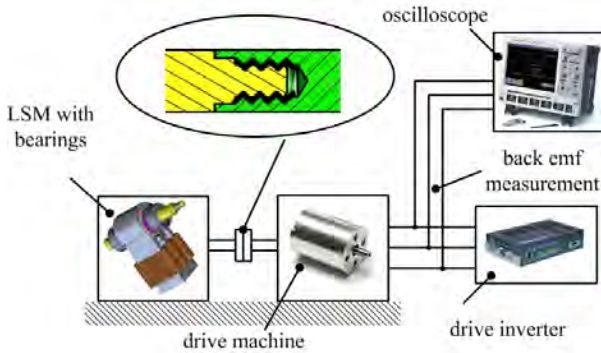


**Figure 4.4:** Block diagram of the high-speed loss measurement setup. Cross-sectional view of the coupling between the drive machine and the LSM shows the screw-thread coupling as well as the alignment surfaces.

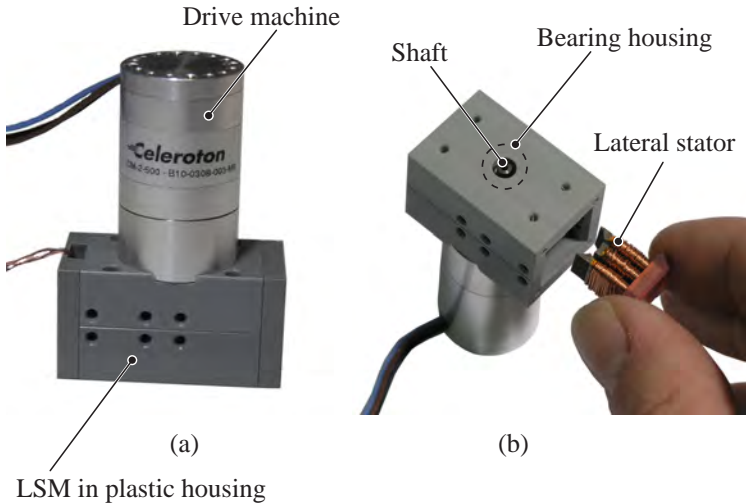


**Figure 4.5:** (a) Photograph of the high-speed loss measurement setup with the drive motor and the LSM. (b) The lateral stator and the shielding iron of the LSM can be taken out without disassembling the housing hence not changing the preload of the bearings.

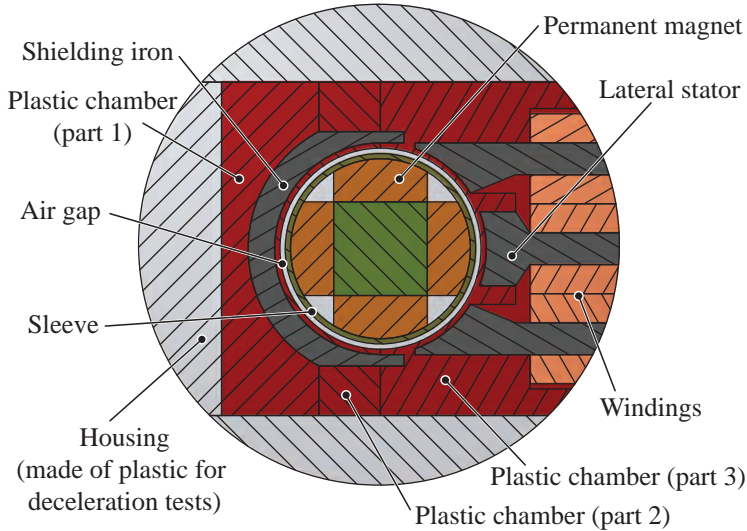


**Figure 4.6:** Cross-sectional view of the no-load loss measurement setup. It can be seen that the air gap and hence the air-friction losses stay the same when the lateral stator and the shielding iron are removed.

To measure the no-load losses, two deceleration tests are carried out, one with and one without the active parts of the LSM. The initial speed in these tests is set to 225 000 r/min, which is higher than the rated speed in order to have measurement results over a broader speed range and to counteract some data loss due to filtering and smoothing during post-processing.

The back EMF of the drive machine is measured across two of its terminals and recorded during deceleration. A decaying sinusoidal curve is fitted on the measured data and the frequency and hence the speed is obtained. Figure 4.8 shows the speed profiles during the two deceleration tests. The losses for the two deceleration tests are calculated according to (4.2) using these speed profiles. Their difference gives the electromagnetic no-load losses of the LSM, which is shown in Figure 4.9.

It can be seen on the same figure that the 2-D FEM simulations result in higher no-load losses compared to the measurements. To investigate this difference further, a 3-D FEM model of the prototype

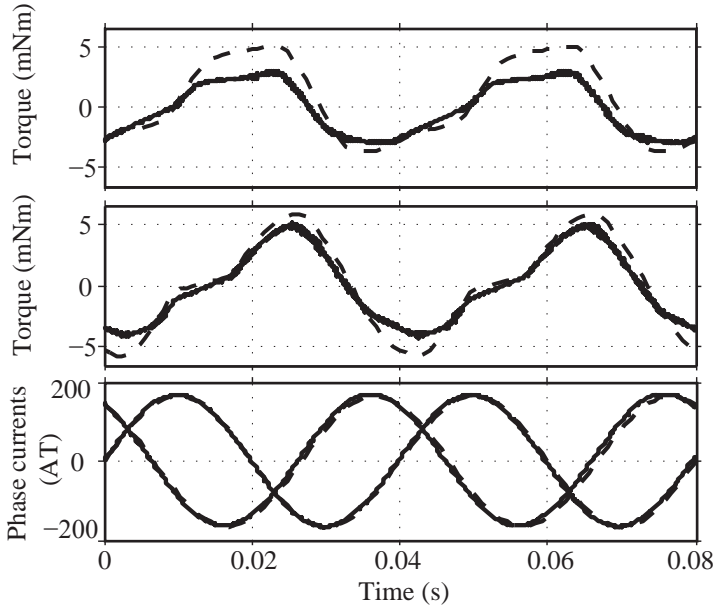


**Figure 4.7:** Results of 2-D FEM simulations and measurements for two different rotor positions that are  $20^\circ$  apart (mechanical). Solid lines show measurements and dashed lines show simulation results. (Top and middle) Simulated and measured torque waveforms. (Bottom) Total currents in machine windings in ampere-turns.

machine was built and simulated for three different speeds. The results from the 3-D FEM models agree with the measurements better, as the end resistances that are neglected in the 2-D models can be accurately modeled in 3-D. This justifies the approach of using 2-D models as an additional safety factor against overheating of the magnets.

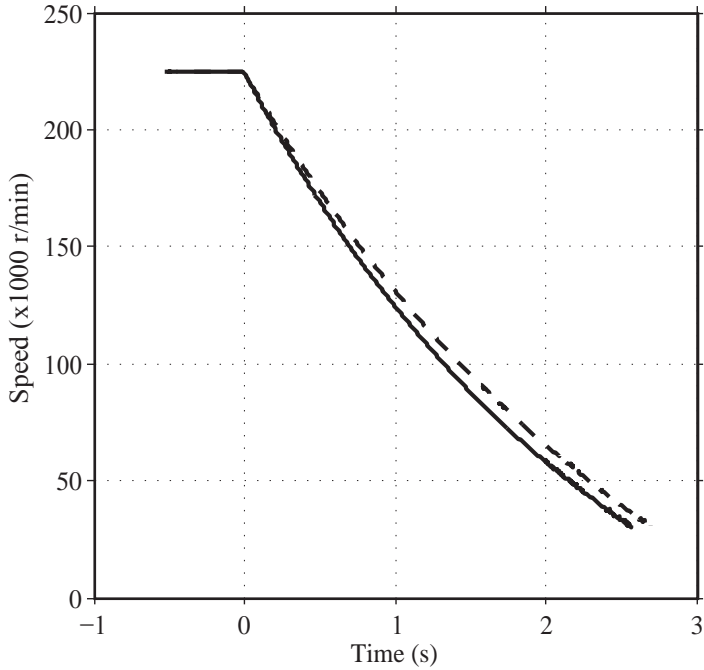


**Figure 4.8:** Speed profiles calculated using the voltage measured at the terminals of the drive machine. Solid line shows the deceleration profile with and the dashed line shows the deceleration profile without the lateral stator and the shielding iron.

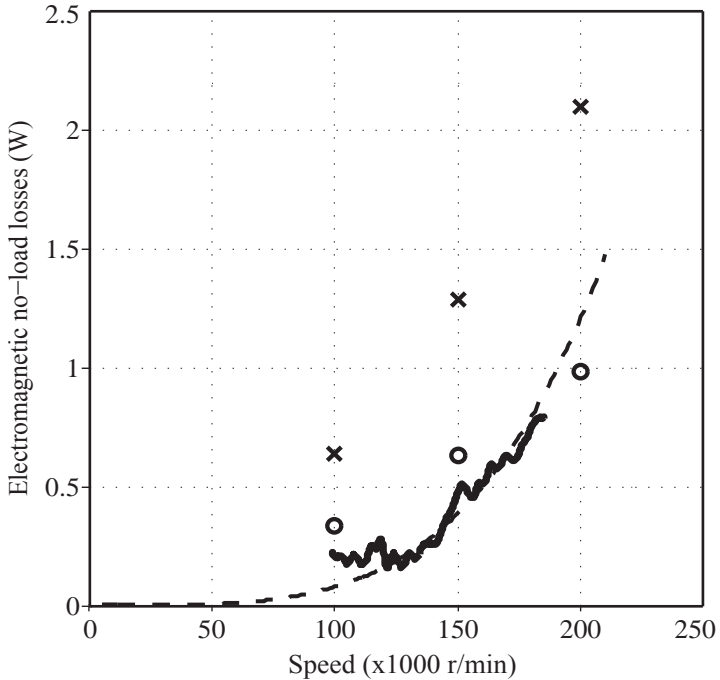


**Figure 4.9:** Electromagnetic no-load losses of the LSM. Crosses denote 2-D FEM and circles denote 3-D FEM simulation results. Solid line shows the difference of two no-load loss measurements, one with and one without the lateral stator and the shielding iron of the LSM. Dashed line shows the fitted curve. It can be seen that the 3-D simulations predict the losses better than the 2-D simulations due to the more accurate calculation of the rotor eddy currents by taking the current distribution in the end regions into account.



# Chapter 5

## Driving the lateral-stator machine

This chapter deals with the design and realization of an inverter for driving the LSM. The focus lies on self-sensing rotor position detection in the entire speed range and torque ripple compensation for a limited speed range. Different rotor position detection methods are briefly mentioned and a novel high-frequency signal injection method is proposed for the rotor position sensing of the LSM. A current profiling approach based on offline FEM simulations is shown to actively compensate the torque ripple.

### 5.1 Self-sensing rotor position detection

#### 5.1.1 State of the art

The LSM is an electronically commutated machine; therefore, the rotor position needs to be known for a controlled operation. Mechanical position sensors such as Hall effect sensors or optical sensors can easily obtain the rotor position. However, these sensors cause additional costs and decrease the reliability of the overall system. Furthermore, the environmental requirements of some applications limit the usability of position sensors. For example, in medical drills some of the conventionally used position sensors would not survive the high temperatures required for the sterilization process.

Position sensors require additional space, which is in conflict with the miniaturization trend of the high-speed drives. The additional space requirement also goes against the driving motivation behind the lateral-stator machine, which is to fit a direct-drive machine in a confined space.

For all the reasons listed above, self-sensing drives (drives without additional position sensors) are receiving increasing attention in the high-speed area as well as for electrical drives in general.

Several self-sensing approaches are described in literature, and they can be divided into two groups: approaches using the back EMF induced by the machine [2], [47], and approaches tracking the machine impedance which depends on the rotor position [48], [49]. As the back EMF gets harder to measure at low speeds and vanishes at standstill, the first group of self-sensing approaches is not operational in the full speed range; therefore not considered any further in this thesis.

In [49], the rotor position is estimated by applying short voltage pulses to the machine in different space vector directions and measuring their current responses. This can be done either by interrupting the drive power to the machine and applying the voltage pulses for a short time interval [50], or by integrating the measurement pulses into the drive Pulse Width Modulation (PWM) [51], [52]. The former method leads to torque distortions, acoustic noise, high current ripple and consequently high copper losses; whereas the latter requires complicated modifications of the PWM pattern, which means additional computational effort for the Digital Signal Processor (DSP).

Another method of tracking the rotor-position-dependent impedance of the machine is by injecting a carrier-frequency signal (generally a voltage) into the machine and extracting rotor position information from the phase or amplitude of its response (generally a current) [53]. Normally, the carrier frequency is selected significantly higher than the fundamental frequency of the drive current, and superimposed to the fundamental frequency by using the drive inverter. Compared to the short voltage pulses, this method has the advantage that it does not require a modification of the PWM patterns, additional  $di/dt$  sensors or oversampling of the current [54]. However, the complicated digital filtering and demodulation of the carrier-frequency response in the DSP may limit the practical application of this method to high-speed drives. Furthermore, superimposing a significantly higher carrier frequency to the fundamental drive current may push the inverter switching frequency beyond practical limits. Inverter output filters that are sometimes used

to suppress the high-frequency components of the drive currents in order to limit the machine losses also make it more challenging to use the inverter itself for injecting a high-frequency signal into the machine.

In this work, a new method for the full speed range quasi-self-sensing<sup>1</sup> operation of high-speed drives is proposed. A carrier-frequency signal is injected into the machine using an additional low-cost injection circuit. Decoupling the signal injection from the drive inverter removes the need for any modification of the PWM patterns and/or increasing the switching frequency. The filtering and demodulation are constructed in dedicated hardware, avoiding any additional computational effort for the DSP.

Differential measurements are used for detecting even weak changes in machine impedance with high accuracy. This property of the proposed self-sensing method makes it a very promising approach for the full speed range self-sensing position detection of not only the LSM but also very-low-saliency slotless PM machines that are generally used above 200 000 r/min.

### 5.1.2 Proposed signal injection method

Figure 5.1 shows the key components of the proposed self-sensing drive. A space-vector-modulation operated, standard, three-phase, two-level inverter feeds power to the machine through an LCL output filter which limits the harmonics applied to the machine. A high-frequency voltage (either sinusoidal or rectangular) is generated independently of the inverter and applied between the star point and one phase terminal of the machine. The high-frequency current flows through one phase of the machine only; and completes its path (in red) through the capacitor  $C_{inj}$ . A differential voltage measurement is taken between the other two phases of the machine, and after filtering and demodulation stages, a signal containing the useful rotor position information is fed to the Analog-to-Digital Converter (ADC) of the DSP.

---

<sup>1</sup>The term quasi-self-sensing is used here to stress that in the method proposed in this work, additional signal injection hardware is required in the inverter. The term self-sensing generally means the estimation of the rotor position without any additional hardware (position sensors) in the machine; and some readers may also infer that no additional hardware (e.g. additional current sensors or signal injection circuitry) is required in the inverter either. Nevertheless, following this explanation, the term self-sensing is used throughout this thesis to describe a position estimation method where no position sensors are required in the machine, but additional signal electronics may be used in the inverter.

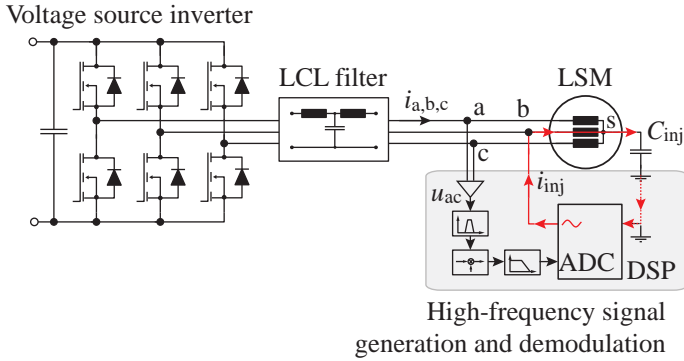


**Figure 5.1:** Overview of the drive system including the drive inverter, an LCL output filter, the machine and the dedicated hardware for position estimation.

If the LCL output filter is assumed to provide a very high impedance between the LSM and the inverter at the injection frequency, and when the phase resistances of the LSM are neglected, the voltages  $u_{as}$ ,  $u_{bs}$  and  $u_{cs}$  are induced in the machine phases (with respect to the star point) due to the self ( $L_{bs}$ ) and mutual ( $M_{ba}$ ,  $M_{bc}$ ) inductances and the high-frequency current  $i_{inj}$  injected into phase B of the machine according to

$$i_{inj} = \hat{i}_{inj} \sin(\omega_{inj}t), \quad (5.1)$$

$$u_{as} = M_{ba} \frac{di_{inj}}{dt} = M_{ba} \omega_{inj} \hat{i}_{inj} \cos(\omega_{inj}t), \quad (5.2)$$

$$u_{bs} = L_{bs} \frac{di_{inj}}{dt} = L_{bs} \omega_{inj} \hat{i}_{inj} \cos(\omega_{inj}t), \quad (5.3)$$

$$u_{cs} = M_{bc} \frac{di_{inj}}{dt} = M_{bc} \omega_{inj} \hat{i}_{inj} \cos(\omega_{inj}t). \quad (5.4)$$

A differential voltage measurement between the machine terminals a and c gives the difference  $u_{ac}$  of the induced voltages as a function of the injection frequency  $f_{inj}$  as

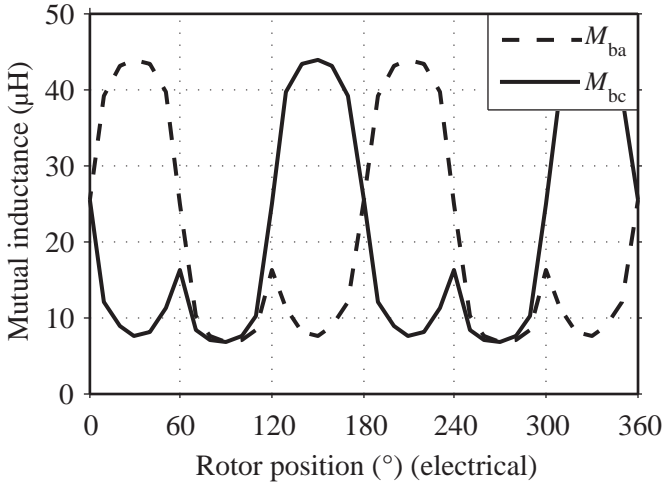


**Figure 5.2:** 2-D FEM simulation results showing the mutual inductances  $M_{ba}$  and  $M_{bc}$ .

$$u_{ac} = (M_{ba} - M_{bc})2\pi f_{inj}\hat{i}_{inj} \cos(\omega_{inj}t). \quad (5.5)$$

The amplitude of  $u_{ac}$  can then be written as

$$\hat{u}_{ac} = (M_{ba} - M_{bc})2\pi f_{inj}\hat{i}_{inj}. \quad (5.6)$$

Figure 5.2 shows that for the LSM, the mutual inductances  $M_{ba}$  and  $M_{bc}$  depend strongly on the rotor position; hence the LSM is not a low-saliency machine. However, it can be seen from (5.5) and (5.6) as well as from Figure 5.3 that a differential measurement enables the utilization of the full range of the ADC for rotor position sensing. In other words, the signal that contains rotor position information is offset-free, and the whole measurement range can be utilized for rotor position sensing. This is an important step towards achieving practical full speed range self-sensing drives with very low-saliency machines such as slotless PM machines.

In order to maximize the accuracy and resolution of the rotor position measurement, the analog signal at the ADC input of the DSP

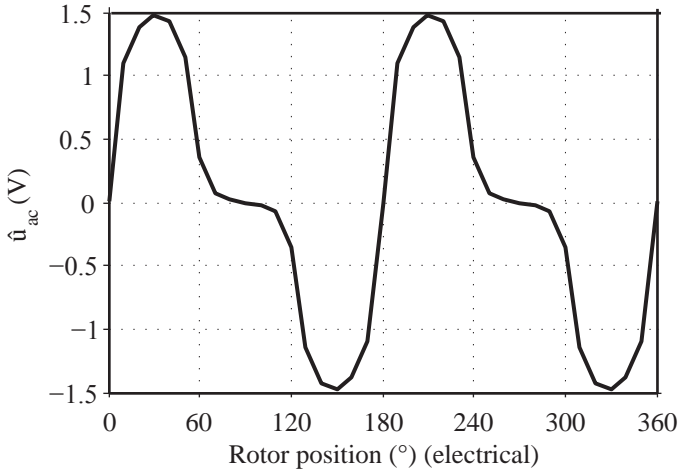


**Figure 5.3:** 2-D FEM simulation results showing the peak value of the differential voltage response for sinusoidal current injection with  $f_{inj} = 1.282$  MHz,  $\hat{i}_{inj} = 5$  mA. x-axis shows rotor's position in electrical degrees. As  $\hat{u}_{ac} = (M_{ba} - M_{bc})2\pi f_{inj}\hat{i}_{inj}$ , the negative values of  $\hat{u}_{ac}$  should be interpreted as the rotor positions where  $M_{ba} < M_{bc}$ .

should be free of any noise and unwanted harmonics. Therefore, frequencies of all possible disturbances need to be taken into account while choosing the injection frequency  $f_{inj}$ . The back EMF is the first disturbance that may affect the position estimation. When a four-pole machine is considered with a considerably large third harmonic component in its back EMF, components up to 20 kHz occur in the frequency spectrum of the the back EMF at 200 000 r/min. Another source of disturbances is the inverter switching harmonics, which are concentrated around multiples of the switching frequency. The stator inductance of the LSM decreases with increasing measurement frequency due to the eddy currents induced both in the stator core and the conductive bodies of the rotor. This fact, along with the self-resonance of the LCL filter inductances, sets the upper limit of the injection frequency  $f_{inj}$ .

As seen in Figure 5.3, the amplitude of the differential voltage response of the machine  $\hat{u}_{ac}$  contains rotor position information. In order to extract this information, firstly  $u_{ac}$  is measured and filtered using a

band-pass filter, whose center frequency is set to the injection frequency  $f_{\text{inj}}$ . This filter suppresses the back EMF and damps the nearest inverter switching-frequency harmonics as shown in Figure 5.4. Then, the band-pass filtered signal is demodulated to extract the rotor position information hidden in its amplitude. A well-known amplitude demodulation method is a simple multiplication of the signal with a cosine function of the same frequency, which can be explained as:

$$u_{\text{sig}} = \hat{u}_{\text{sig}} \cos(\omega_{\text{sig}} t), \quad (5.7)$$

$$u_{\text{sig,dm}} = \hat{u}_{\text{sig}} \cos(\omega_{\text{sig}} t) \cos(\omega_{\text{sig}} t), \quad (5.8)$$

$$u_{\text{sig,dm}} = \frac{\hat{u}_{\text{sig}}}{2} + \frac{\hat{u}_{\text{sig}}}{2} \cos(2\omega_{\text{sig}} t), \quad (5.9)$$

where,  $u_{\text{sig}}$  is an amplitude modulated signal with angular frequency  $\omega_{\text{sig}}$  and  $u_{\text{sig,dm}}$  is the demodulated signal. In (5.9), it is clear that multiplication with the carrier frequency moves the amplitude to DC and makes the further processing easier. This is also shown in Figure 5.5. Finally, a low-pass filter is used to suppress the demodulated disturbances before the signal containing the rotor position information is fed into the ADC of the DSP. The selection of the cut-off frequency of the low-pass filter is a trade-off between filtering performance and the dynamics of the signal containing rotor position information. As the signal waveform shown in Figure 5.3 is not a purely sinusoidal signal, its highest-frequency significant component needs to be identified as well as the maximum allowed phase lag at a given rotor speed. For example, for the waveform shown in Figure 5.3, the highest-frequency harmonic considered is the 10<sup>th</sup> with an amplitude of 12.3% of the highest-amplitude component. This component has a frequency of 13.33 kHz at 40 000 r/min. For an accurate rotor position estimation with look-up tables in the DSP, the maximum allowed phase lag at this frequency is set to 10°. Section 5.3.2 details the realization of the low-pass filter as a series connection of two 2<sup>nd</sup> order active filters in Sallen-Key topology.

It is clearly seen on Figure 5.3 that the frequency of the signal fed into the DSP is twice the electrical frequency of the rotor. Therefore, the initial rotor position cannot be detected using this signal. However, in the LSMs the saturation of the stator core can be used to determine the initial rotor position using well-known methods like the one presented in [49].

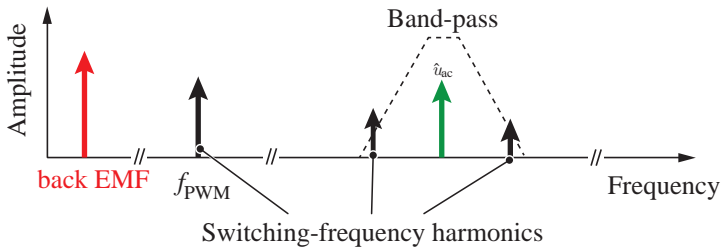


**Figure 5.4:** Frequency spectrum of the machine voltage.

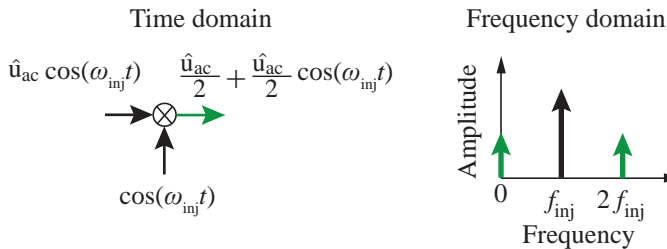


**Figure 5.5:** Amplitude demodulation in the time and frequency domain.

## 5.2 Active torque ripple compensation

Torque ripple is an undesired effect in applications like machining spindles and dental drills, especially at low speeds, as it may lead to speed oscillation. In literature, several machine design methods are presented to minimize torque ripple such as skewing or adjusting the shape of permanent magnets [55]. There have also been various studies on different control methods in order to reduce torque pulsations. In [56], an estimator-based method is presented, and in [57], the authors use the actual back EMF waveform to calculate the current waveform giving a ripple-free torque. However, as the torque ripple in the machines described in this thesis are load dependent and caused by phenomena such as saturation and leakage flux that are not easy to model analytically, an FEM-based torque ripple compensation method is presented.

Figure 5.6 shows the space vector of stator currents  $\underline{i}_s$  and the

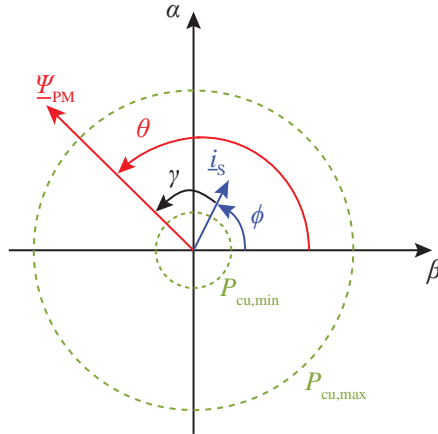


**Figure 5.6:** PM field and phase current space vectors.

permanent-magnet flux  $\psi_{\text{PM}}$  in the stator ( $\alpha\beta$ ) coordinate system. As known from the well-established theory of vector control of surface-mounted PM machines, in order to ensure maximum torque-per-current, stator and rotor fluxes have to be orthogonal. That means that the angle between  $i_s$  and  $\psi_{\text{PM}}$  should stay constant, and the torque is adjusted by adjusting the magnitude of  $i_s$ . This corresponds to the commonly used convention of having a zero direct current component ( $i_d = 0$ ) and controlling the torque by controlling the quadrature current component ( $T \propto i_q$ ) in the rotor (dq) coordinate system.

A stator current space vector rotating with constant angular frequency in the  $\alpha\beta$  coordinate system corresponds to three-phase,  $120^\circ$  phase shifted, balanced sinusoidal currents with the same angular frequency. The torque in this case is constant in an ideal surface-mounted PM machine. However, as shown earlier in this thesis, stator slotting and asymmetrical air gap permeance as well as the magnetic asymmetry of the machine phases and the saturation of the stator core lead to considerable torque ripple in the LSM when driven by balanced sinusoidal currents.

In order to find a stator current profile that produces a ripple-free torque, FEM simulations are used. For each rotor position  $\theta$ , the torque

	Sinusoidal	Compensated
Mean torque	8.6 mN m	8.2 mN m
Mean copper losses	8 W	8 W

**Table 5.1:** Torque and copper losses for sinusoidal and compensated currents.

is calculated for different stator current space vectors while the angle  $\phi$  is swept from  $0^\circ$  to  $360^\circ$  and the magnitude is swept from the value leading to a defined minimum copper loss  $P_{\text{cu,min}}$  to the value leading to a defined maximum copper loss  $P_{\text{cu,max}}$  (cf. Figure 5.6).

As an example, in Section 3.1.4 the machine shown in Figure 3.3 is identified as the best one in the analyzed discrete parameter range. It produces the highest mean torque compared to the other machines at 8 W of copper losses while still producing less no-load losses than the no-load loss limit. To find the current profile that generates a ripple-free torque for this specific machine, its torque is calculated using FEM simulations at different fixed rotor positions while current space vectors with different magnitudes are rotated for a whole electrical period. The range of the magnitude of the current space vector  $\underline{i}_s$  is adjusted such that the smallest magnitude leads to 0.5 W and the largest leads to 16 W of copper losses.

Figure 5.7 shows the instantaneous torque at a fixed rotor position for different magnitudes (leading to different copper losses) and angles of the current space vector  $\underline{i}_s$ . For generating a given torque at this specific rotor position, the angle and magnitude of the current space vector generating that torque with minimum losses shall be found.

Figure 5.8 shows the same information in a contour plot, where the optimum current angles leading to minimum copper losses are shown with the dashed lines. Using this algorithm, previously calculated currents can be injected in the machine windings depending on the torque reference and the actual rotor position. Figure 5.9 shows the torque of the machine under consideration when driven by three-phase sinusoidal currents, whereas the compensated current waveform as well as the resulting torque can be seen in Figure 5.10. The torque and copper losses for sinusoidal and compensated currents are listed in Table 5.1

The active torque ripple compensation approach presented here relies on an accurate rotor position information (similar to the widely

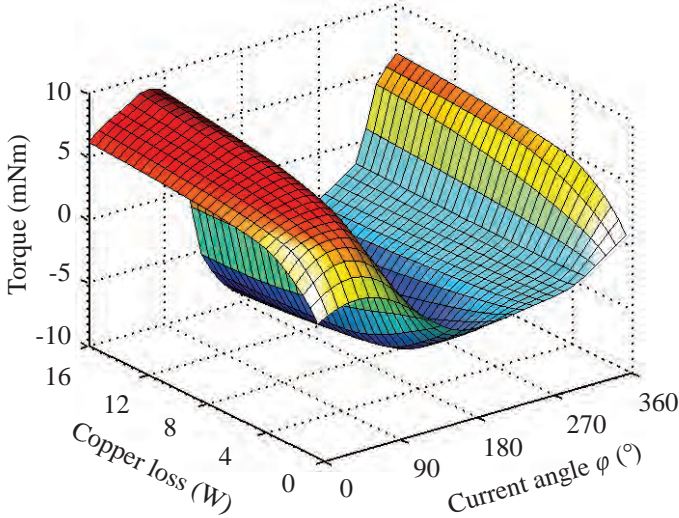


**Figure 5.7:** Torque generated by different current vectors versus the copper losses and the current angle at one rotor position.

used vector control of PM machines). Furthermore, the dependency of the torque on the amplitude and angle of the current space vector needs to be known for every rotor position. Using offline FEM calculations and storing the data on look-up tables is a viable solution even though it adds to the memory requirement of the DSP. Finally, the bandwidth of the inverter needs to be higher compared to a standard vector control drive as the optimum stator current has higher order harmonics and is not purely sinusoidal anymore. On the other hand, the effect of torque ripple is mainly important at low speeds as the inertia of the mechanical system filters the speed oscillations at higher speeds.

The mechanical transient behavior of a rotor with axial moment of inertia  $I$ , can be described as

$$T - T_1 = I \frac{d\omega_m}{dt}, \quad (5.10)$$

where  $T$  is the motor torque, the  $T_1$  is the load torque and  $\omega_m$  is the rotational speed. In a simplified model of a section-type LSM, the machine and load torques can be written as

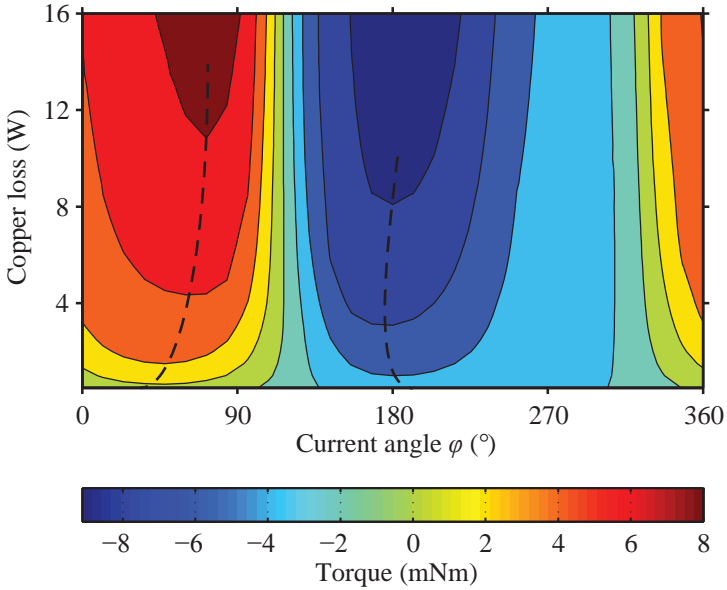


**Figure 5.8:** Contour plot showing the machine torque for different current space vector angles and magnitudes. The optimum current angles leading to minimum copper losses are shown with the dashed lines. The torque at zero copper losses (zero current) is the cogging torque.

$$T = T_{\text{mean}} + \Delta T \sin(4\omega_m t), \quad (5.11)$$

$$T_1 = k_1 \omega_m^2, \quad (5.12)$$

where  $k_1$  is a constant.

Figure 5.11 plots speed ripple<sup>2</sup> as a function of average speed for  $T_{\text{mean}} = 8 \text{ mNm}$ ,  $\Delta T = 4 \text{ mNm}$  and  $I = 1.94 \times 10^{-8} \text{ kg m}^2$ , which is the axial moment of inertia of the LSM's rotor. It can be seen that the effect of the torque ripple decays rapidly with increasing speed and

<sup>2</sup>Speed ripple is defined as the peak-to-peak variation of speed as the percentage of the average speed.

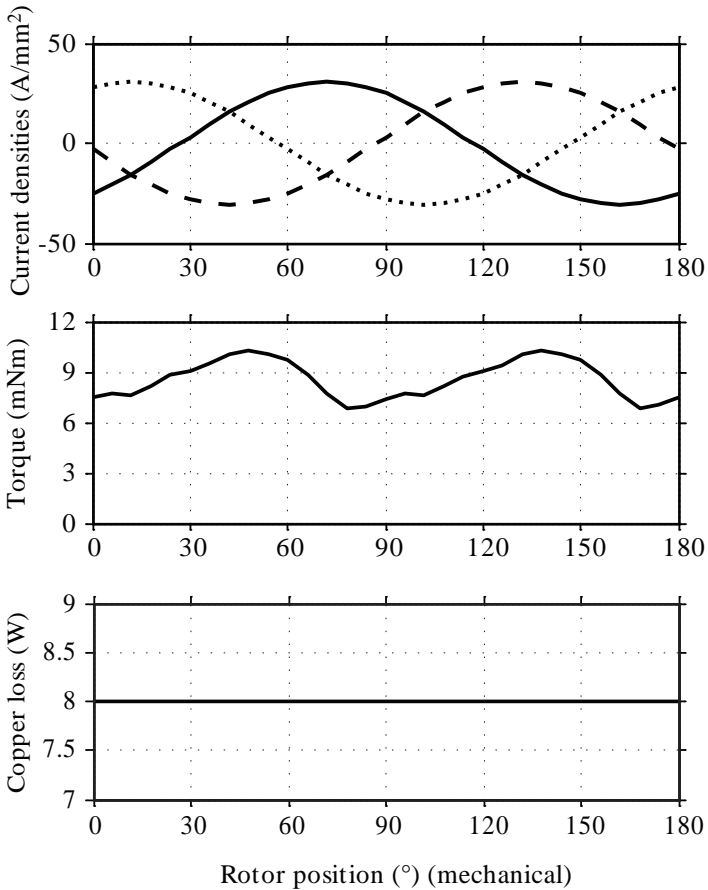


**Figure 5.9:** Phase current densities and machine torque for sinusoidal currents creating constant instantaneous copper losses of 8 W. Average torque is 8.6 mNm.

falls below 1% above 40 000 r/min. Hence, the described torque ripple compensation method is only considered at lower speeds. This also makes the inverter design easier in terms of the bandwidth of the current control. As torque ripple compensation is considered only for low speeds, its effects on the core losses or rotor eddy-current losses are not

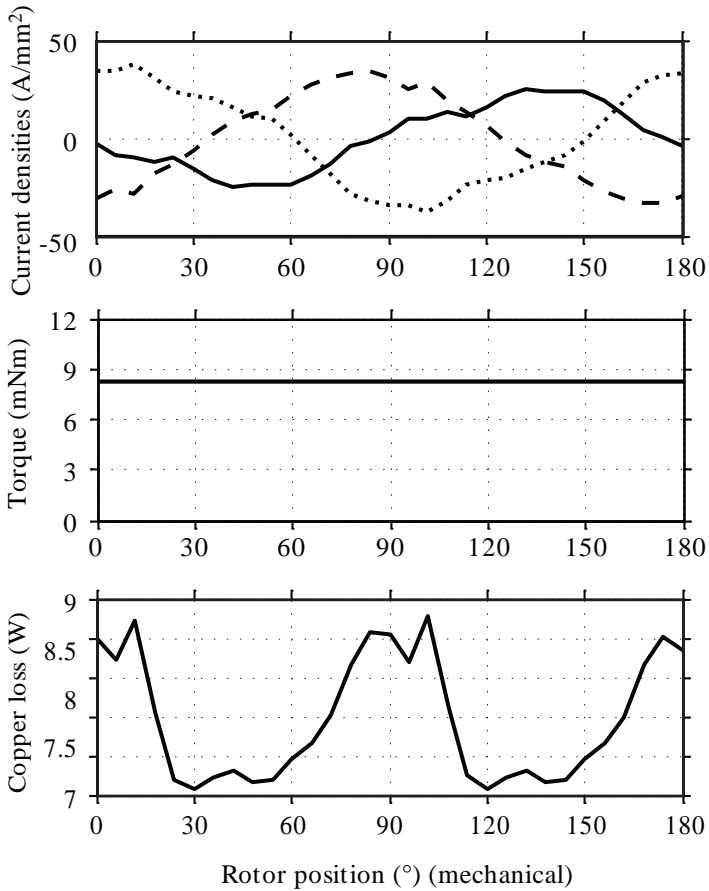


**Figure 5.10:** Stator current densities, machine torque and instantaneous copper losses for torque ripple compensation. Average copper losses are 8 W. Torque is constant at 8.2 mNm.

investigated.

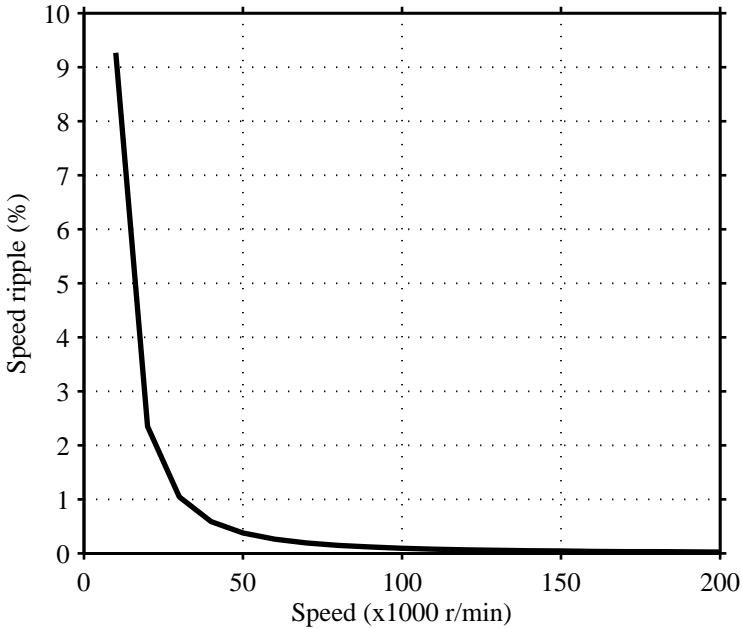


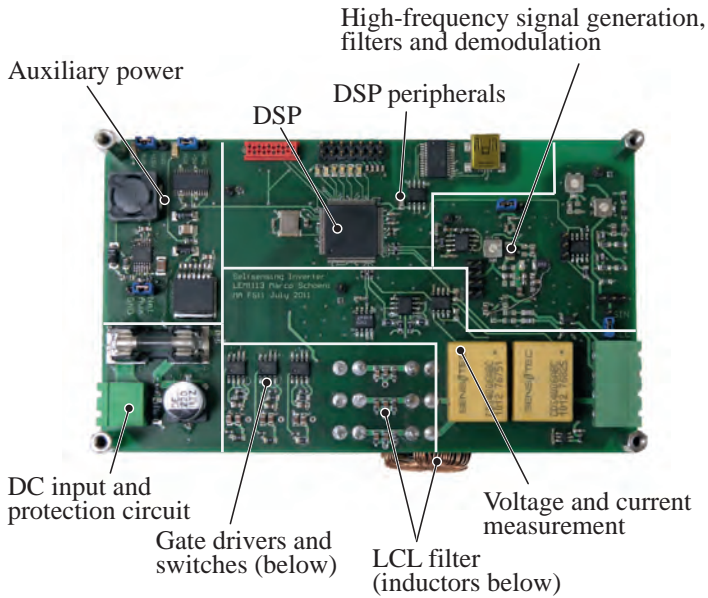
**Figure 5.11:** Ratio of the peak-to-peak speed to the average speed as a function of the average speed for  $T_{\text{mean}} = 8 \text{ mN m}$ ,  $\Delta T = 4 \text{ mN m}$  and  $I = 1.94 \times 10^{-8} \text{ kg m}^2$ . The speed ripple decays rapidly with increasing average speed and falls below 1% above 40 000 r/min.

## 5.3 Hardware realization

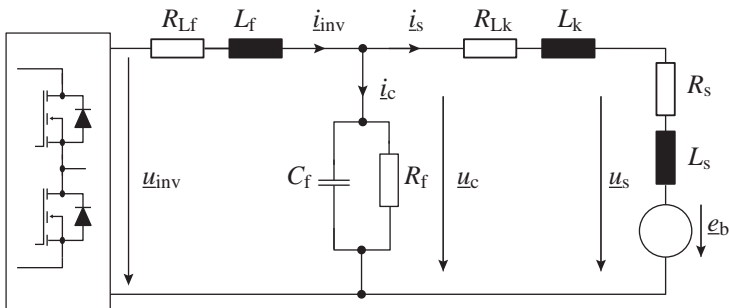
### 5.3.1 Power electronics

Figure 5.12 shows the realization of the inverter on a 4-layer, 14 cm x 8 cm PCB. The DC link input is designed for 36 V and is protected by a parallel Zener diode and a 6 A fuse. Auxiliary power supplies generate voltage levels of 15 V, 7.5 V, 5 V, 3.3 V and 1.5 V for the gate drivers, the DSP and various other components used for the high-frequency signal generation, filtering and demodulation for the rotor position estimation. IRF6674TRPbF MOSFETs [58] are used as power switches. The inverter switching frequency is 180 kHz.

An LCL output filter is used for damping the drive current harmon-



**Figure 5.12:** Hardware realization of the inverter on a 14 cm x 8 cm PCB.



**Figure 5.13:** One phase equivalent circuit of the inverter, LCL output filter and the machine.

ics. The equivalent circuit of the filter including the motor is shown in Figure 5.13 where  $L_f$  and  $L_k$  are the inductances and  $R_{Lf}$  and  $R_{Lk}$  are the resistances of the filter inductors,  $L_s$ ,  $R_s$  and  $\underline{e}_b$  are machine's stator inductance, resistance and back EMF,  $C_f$  is the capacitance of the filter capacitor and  $R_f$  is the damping resistance. After defining  $L_2$  and  $R_2$  as  $L_2 = L_k + L_s$  and  $R_2 = R_{Lk} + R_s$ , the following equations can be written in the rotating reference frame

$$\underline{u}_s = (sL_2 + R_2)\underline{i}_s + \underline{e}_b, \quad (5.13)$$

$$\underline{i}_c = (sC_f + \frac{1}{R_f})\underline{u}_c, \quad (5.14)$$

$$\underline{u}_{inv} = (sL_f + R_{Lf})\underline{i}_{inv} + \underline{u}_c, \quad (5.15)$$

$$\underline{i}_{inv} = \underline{i}_c + \underline{i}_s. \quad (5.16)$$

By rearranging equation (5.13) - (5.16), the stator current transfer function is found as

$$\underline{I}_s(s) = \frac{\underline{U}_{inv}(s) - \underline{e}_b(s)(s^2C_fL_f + s(C_fR_{Lf} + \frac{L_f}{R_f}) + \frac{R_{Lf}}{R_f} + 1)}{s^3A + s^2B + sC + D}, \quad (5.17)$$

where  $A = L_fL_sC_f$ ,  $B = L_fC_fR_2 + L_2R_{Lf}C_f + L_fL_2/R_f$ ,  $C = R_{Lf}R_2C_f + L_fR_2/R_f + L_2R_{Lf}/R_f + L_f + L_2$  and  $D = R_{Lf} + R_2 + R_{Lf}R_2/R_f$ .

The resonance frequency is given as

$$f_{res} = \frac{1}{2\pi\sqrt{C_f\frac{L_fL_2}{L_f+L_2}}}. \quad (5.18)$$

The transfer function in (5.17) can be approximated by a first order system below the resonance frequency by neglecting  $C_f$  and  $R_f$  as

$$\underline{I}_s(s) \approx \frac{\underline{U}_{inv}(s) - \underline{e}_b(s)}{s(L_f + L_2) + R_{Lf} + R_2}. \quad (5.19)$$

Figure 5.14 shows the Bode plot of the actual damped LCL filter according to (5.17) and the simplified first order low-pass filter according to (5.19) for the values given in Table 5.2. Below the resonance

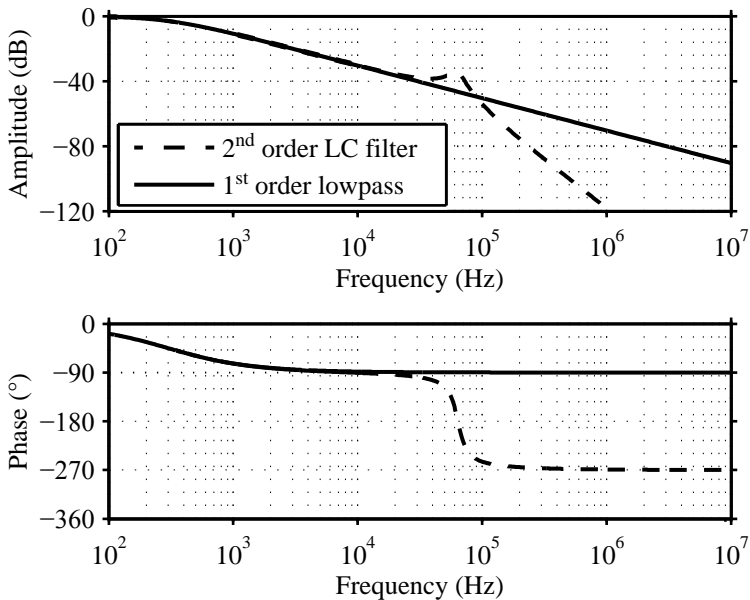


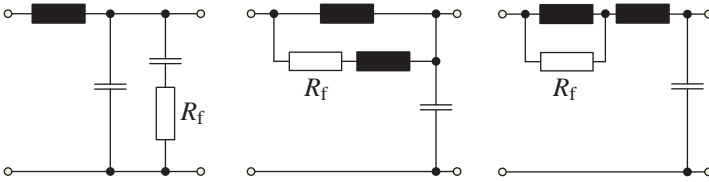
**Figure 5.14:** Bode plot of the transfer function of the LCL output filter and its first order low-pass approximation. The simplified and the actual transfer functions coincide below the resonance frequency at around 60 kHz.

frequency at around 60 kHz, the simplified and the actual transfer functions coincide and the filter - machine combination acts as an inductive load.

The selection of the resonance frequency is a trade-off between a better damping of the inverter switching harmonics and higher achievable current control bandwidth. A low resonance frequency means better damping of the harmonics but on the other hand it leads to a larger phase lag, reducing the maximum current bandwidth. In this application, the resonance frequency is set to 60 kHz.

In the filter topology shown in Figure 5.13, the power dissipation in the damping resistor  $R_f$  is high and this hinders the inverter efficiency. Figure 5.15 shows further topologies that enable the damping of the

$L_f = 200 \mu\text{H}$	$R_{L_f} = 0.25 \Omega$
$L_k = 300 \mu\text{H}$	$R_{L_k} = 0.45 \Omega$
$L_s = 30 \mu\text{H}$	$R_s = 0.3 \Omega$
$C_f = 50 \text{ nF}$	
$R_f = 200 \Omega$	

**Table 5.2:** Values of the LCL filter components.**Figure 5.15:** Different approaches of filter damping [59].

filter in a more efficient way [59].

### 5.3.2 Rotor position sensing

#### Signal injection

As it can be seen in Figure 5.3, the signal  $\hat{u}_{ac}$  that contains rotor position information goes flat for some rotor positions. This is caused by the geometry of the specific machine under consideration, and it decreases the sensitivity of the position sensing at these rotor positions. To overcome this problem, the current is injected to the machine through a resonant tank (cf. Figure 5.16), whose resonant frequency changes with phase inductance of the machine. The tank is designed such that the resonant frequency moves closer to the injection frequency in regions where  $\hat{u}_{ac}$  goes flat, increasing the injected current, thus increasing the sensitivity. Doing so, the injected current only increases when needed, avoiding unnecessary losses. Figure 5.17 shows this for  $f_{inj} = 1.282 \text{ MHz}$ ,  $C_{hf} = 78 \text{ pF}$ ,  $L_{hf} = 200 \mu\text{H}$  when the inductance of the machine phase where the high-frequency signal is injected changes from  $L_s = 26 \mu\text{H}$  to  $L_s = 75 \mu\text{H}$ . The resulting normalized amplitudes of the injected current are plotted in Figure 5.18.

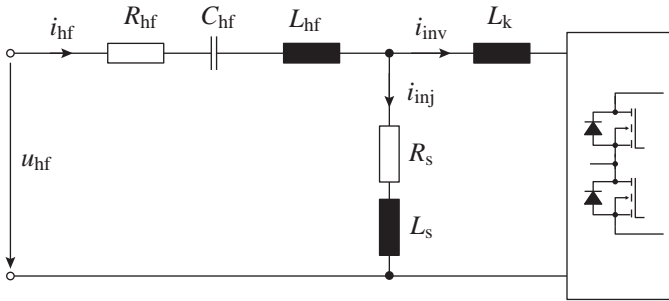


**Figure 5.16:** Resonant injection circuit which provides more current at the critical rotor positions.

### Rotor position estimation

Figure 5.19 shows the block diagram of the hardware realization of the high-frequency signal measurement, filtering and demodulation for rotor position estimation. Firstly, the voltage response of the machine to the injected high-frequency signal is measured using a differential amplifier and series capacitors for blocking the low-frequency components. The voltage  $u_{\text{offset},1}$  shifts the measured AC voltage to positive values such that single-supply operational amplifiers can be used.

The measured signal is filtered by a 4<sup>th</sup>-order band-pass filter whose center frequency is at the injection frequency. The realization of this filter with passive components is shown in Figure 5.20.

The transfer function of the band-pass filter in the Laplace domain is obtained by dividing the 4<sup>th</sup>-order band-pass into two 2<sup>nd</sup>-order filters (the low-pass stage composed of  $P_s$  and  $C_s$  is neglected in the first step)

$$V_1(s) = \frac{sL_1}{s^2L_1C_1R_1 + sL_1 + R_1} V_{\text{ac}}(s), \quad (5.20)$$

$$V_{\text{ac,bp}}(s) = \frac{sC_2R_2}{s^2L_2C_2 + sC_2R_2 + 1} V_1(s). \quad (5.21)$$

Multiplying (5.20) and (5.21) yields the 4<sup>th</sup>-order transfer function, which is plotted in Figure 5.21.

As the tolerances of the inductances and the series resistance of the inductors may slightly modify the behavior of the band-pass filter, an

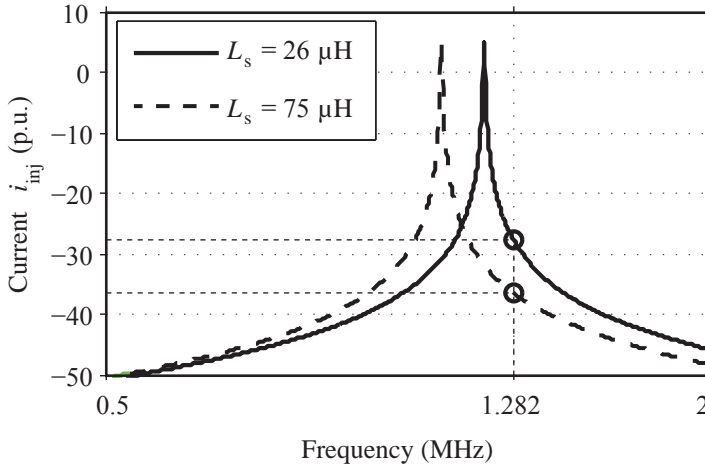


**Figure 5.17:** Amplitude of the injection current for different machine inductances. At the injection frequency  $f_{\text{inj}} = 1.282$  MHz, the amplitude of the current is calculated as 15.2 mA for  $L_s = 75 \mu\text{H}$  and as 41.5 mA for  $L_s = 26 \mu\text{H}$ .

additional low-pass filter made of  $P_s$  and  $C_s$  is added to the hardware in order to have the ability to tune the phase in case it is necessary.

The well-known amplitude demodulation by multiplication with a cosine function with the injection frequency is explained in Section 5.1.2. However for simplicity, a slightly different demodulation is implemented in hardware. Analog switches are used for a phase-sensitive rectification as shown in Figure 5.22. This can be interpreted as multiplication by a rectangular wave instead of a cosine a function, yielding an average of  $2\hat{u}_{\text{sig}}/\pi$  in the demodulated signal, which is higher compared to the  $\hat{u}_{\text{sig}}/2$  in (5.9). The demodulated signal  $u_{\text{ac, dm}}$  is obtained by using a differential amplifier circuit after the phase sensitive rectification.

Finally, the demodulated signal  $u_{\text{ac, dm}}$  is low-pass filtered to get the mean value which can be sampled by the DSP to obtain the rotor position information. The cut-off frequency is selected such that the phase lag at 13.33 kHz (40 000 r/min) does not exceed  $10^\circ$ .

Figure 5.23 shows the realization of the 4<sup>th</sup>-order active low-pass filter as the connection of two active 2<sup>nd</sup>-order low-pass filters in a

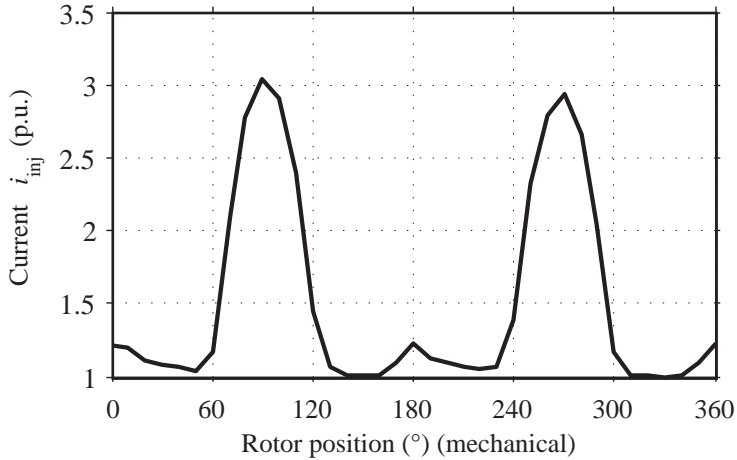


**Figure 5.18:** Normalized amplitude of the injection current for different rotor positions.

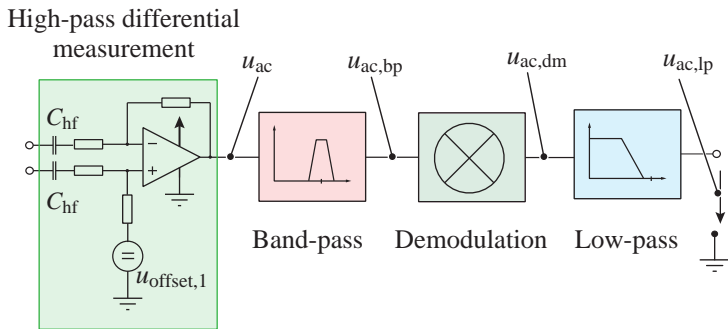


**Figure 5.19:** Block diagram of the rotor position estimation hardware.

Sallen-Key topology. The transfer function of a 2<sup>nd</sup>-order stage  $H_{2nd}$  can be written as

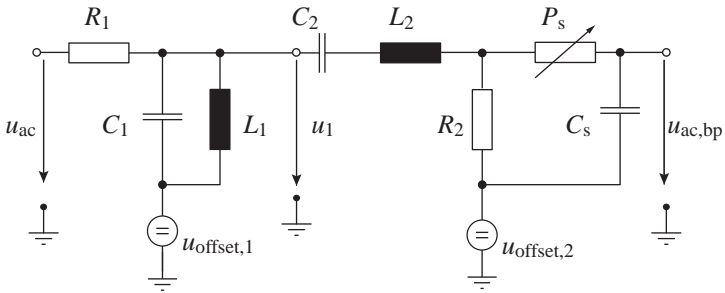


**Figure 5.20:** Realization of the band-pass filter using passive components.

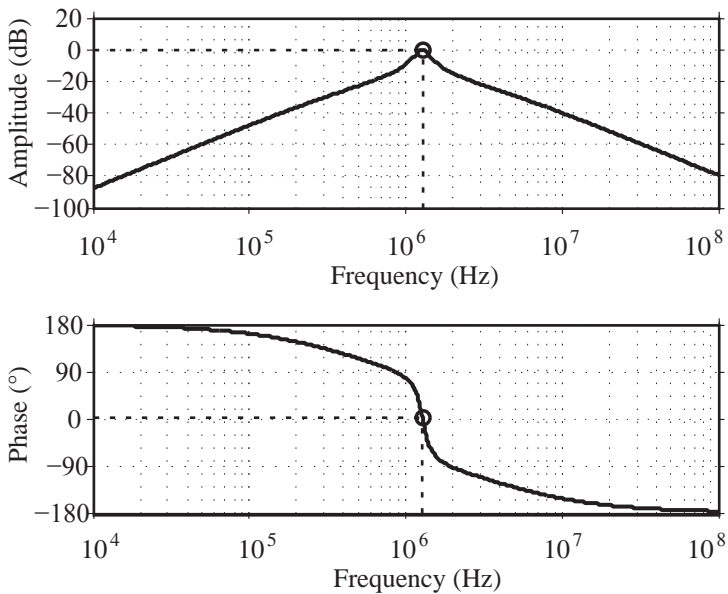


**Figure 5.21:** Bode plot of the 4<sup>th</sup>-order band-pass filter. Center frequency is 1.282 MHz, for  $R_1 = 100 \Omega$ ,  $L_1 = 2.2 \mu\text{H}$ ,  $C_1 = 7 \text{ nF}$ ,  $R_2 = 1 \text{ k}\Omega$ ,  $L_2 = 33 \mu\text{H}$ ,  $C_2 = 470 \text{ pF}$ .

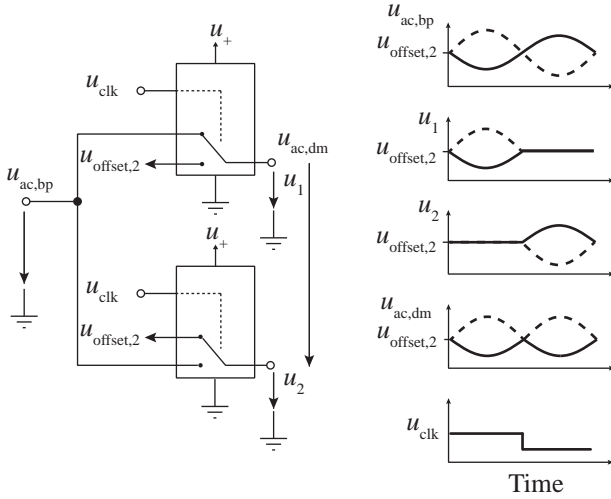


**Figure 5.22:** Phase sensitive rectification with analog switches. Dashed and solid lines show signals for two different rotor positions.

$$H_{2\text{nd}}(s) = \frac{(2\pi f_0)^2}{s^2 + s2\pi\frac{f_0}{Q} + (2\pi f_0)^2}, \quad (5.22)$$

$$f_{0x} = \frac{1}{2\pi\sqrt{R_{1x}R_{2x}C_{1x}C_{2x}}}, \quad x = [A, B], \quad (5.23)$$

$$Q_x = \frac{\sqrt{R_{1x}R_{2x}C_{1x}C_{2x}}}{C_{2x}(R_{1x} + R_{2x})}, \quad x = [A, B], \quad (5.24)$$

where  $f_0$  is the cut-off frequency and  $Q$  the quality factor whereas A and B denote the first and second 2<sup>nd</sup>-order stages.

The DC gain  $G_{DC}$  can be set as

$$G_{DC} = 1 + \frac{R_4}{R_3}, \quad (5.25)$$

and the overall transfer function is calculated as

$$H_{4\text{th}}(s) = G_{DC}H_{2\text{nd},A}(s)H_{2\text{nd},B}(s). \quad (5.26)$$

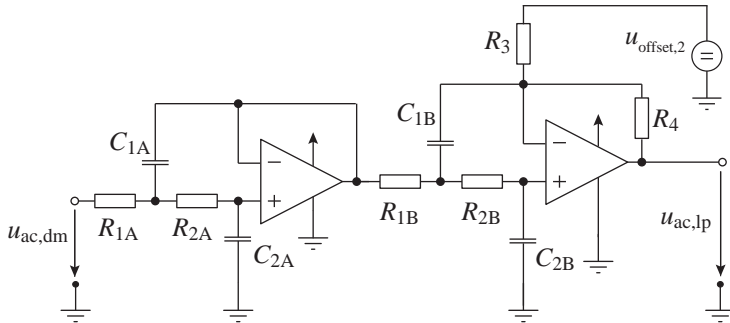


**Figure 5.23:** 4<sup>th</sup>-order active low-pass filter as the series connection of two active 2<sup>nd</sup>-order low-pass filters in Sallen-Key topology.

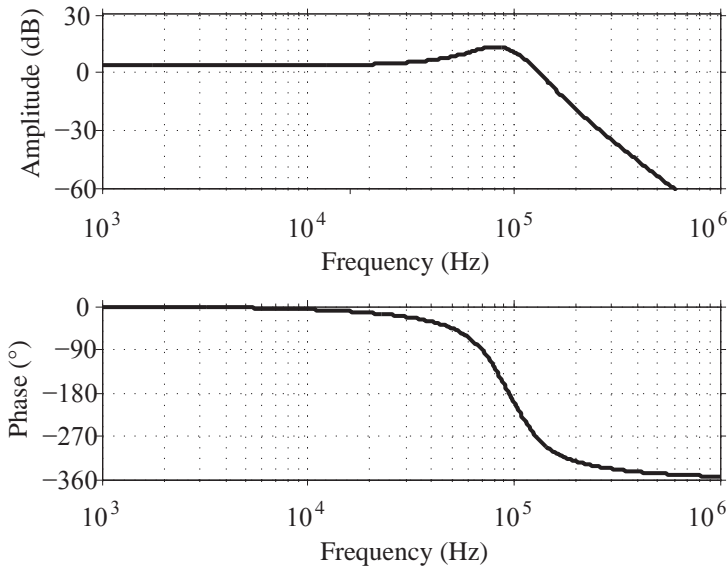


**Figure 5.24:** Bode plot of the 4<sup>th</sup>-order low-pass filter. The resonance frequencies and the quality factors of the 2<sup>nd</sup>-order stages are  $f_{0,A} = 81.8 \text{ kHz}$ ,  $f_{0,B} = 109.4 \text{ kHz}$ ,  $Q_A = 1.872$ ,  $Q_B = 1.829$  and the DC gain is  $G_{DC} = 1.5$ .

## 5.4 Software realization

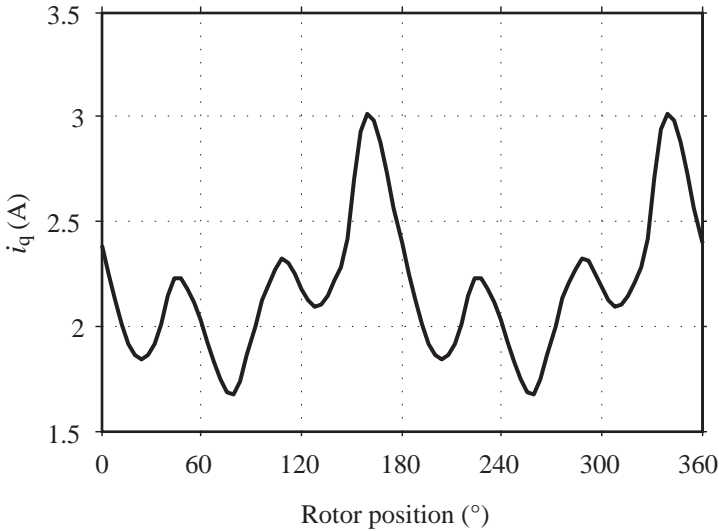
According to the well-known theory of vector control of surface-mounted PM machines, the three-phase stator currents can be expressed as direct and quadrature ( $i_d, i_q$ ) components in a dq-coordinate system that rotates with the rotor. In this case, the machine torque can be controlled by controlling  $i_q$  and  $i_d$  is set to zero for maximum torque-per-current operation. However, when the current profiles that actively cancel the torque in an LSM are written in the dq coordinate frame, both  $i_q$  and  $i_d$  are non-zero and they vary with rotor position (unlike the  $i_q$  in an ideal PMSM that stays constant for a given torque reference, regardless of the rotor position). This leads to two look-up tables, one for the optimum  $i_q$  and the other for the optimum  $i_d$  as a function of rotor position. Along with the increased control bandwidth requirement, this means also increased memory requirement for the DSP. However, for the first prototype of the LSM presented in this work, it is seen that setting  $i_d = 0$  and varying only the  $i_q$  for having a ripple-free torque leads to a mere 10% additional copper losses in the machine. Therefore, torque ripple compensation is realized by only modifying  $i_q$  as a function of rotor position and the torque reference while controlling  $i_d$  to zero. Figure 5.25 shows  $i_q$  over one period to achieve a ripple-free torque of 2.5 mNm and Figure 5.26 shows the first 20 Fourier coefficients of this waveform. The higher-order components that do not exist in a standard vector-controlled drive increase the control bandwidth requirement.

Figure 5.27 shows a block diagram of the overall drive system including the look-up tables for the rotor position estimation and torque ripple compensation.

## 5.5 Experimental results

### 5.5.1 Active torque ripple compensation

Figure 5.28 shows the experimental results of the torque ripple compensation at 5000 r/min and Figure 5.29 for 40 000 r/min. The dynamics of the current reference coincides with the according rotational speed whereas the machine is at standstill during the measurements. The quadrature current  $i_q$  varies according to the offline FEM simulations to compensate the torque ripple, while the direct component of the



**Figure 5.25:** Amplitude of  $i_q$  for constant torque of 2.5 mN m over one period.

current  $i_d$  is controlled to zero.

At 5000 r/min, the dynamics of  $i_q$  are comparably low and the actual current follows the reference very closely. At 40 000 r/min, the bandwidth limitations start to appear and the control error increases. Nevertheless, the average of the control error at 40 000 r/min is measured to be less than 1%.

### 5.5.2 Rotor position estimation

Figure 5.30 shows the digital rotor position signal (sampled by the ADC of the DSP) after the measurement, filtering and demodulation stages. It can be seen that almost the full range of the 12-bit ADC can be used for rotor position extraction, which proves the advantage of the differential measurement. When compared to Figure 5.3, it is also clear that the resonant injection tank helps to increase the sensitivity at the rotor positions where the signal goes flat.

The final estimation of the actual rotor position using the sampled

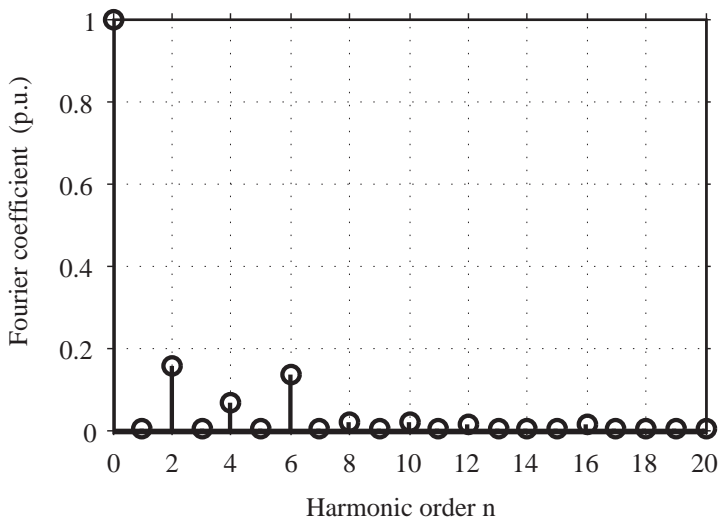


**Figure 5.26:** First 20 Fourier coefficients of  $i_q$ . For 40 000 r/min, the frequency of the 6<sup>th</sup> harmonic component is 8 kHz.

ADC result can be achieved by using look-up tables. Figure 5.31 shows the results of the position estimation using look-up tables.

It has to be noted that these results are obtained in a test setup where the rotor is fixed at different positions and the look-up tables in the DSP are used to estimate the rotor position depending on the filtered and demodulated response of the machine to the injected high-frequency signal. From Figure 5.30, it can be seen that the information contained in the signal sampled by the DSP is not enough to determine the direction of rotation. For determining the direction of rotation, a second channel of injection is needed.

Figure 5.32 shows a topology where two high-frequency signal injection channels inject two signals with different frequencies into the different phases of the machine. Two separate channels measure, filter and demodulate the respective responses of the machine. Figure 5.33 shows a different topology where one high-frequency injection and measurement channel is used to measure the impedance of different machine phases sequentially.

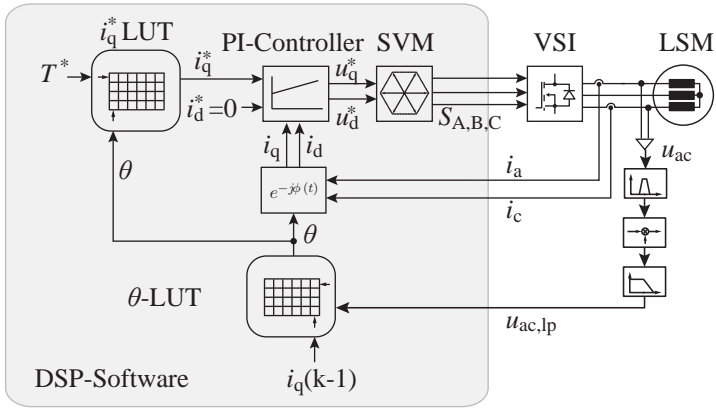


**Figure 5.27:** Block diagram of the overall drive system. The rotor position look-up table (LUT) estimates the rotor position based on the high-frequency voltage response of the machine as well as the current flowing in the machine (saturation effect). A second look-up table is used to find the optimum quadrature current reference  $i_q^*$  to create a ripple-free torque for a given torque reference  $T^*$  and rotor position  $\theta$ .

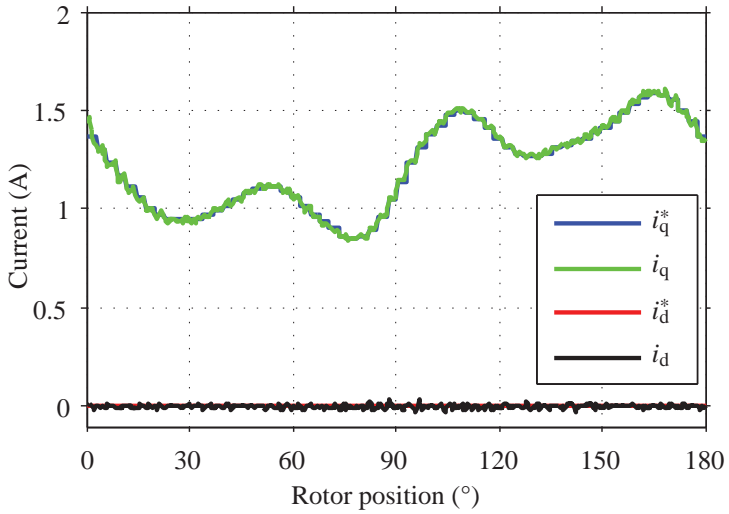


**Figure 5.28:** Reference and measured values of  $i_d$  and  $i_q$  resulting in a smooth torque. The reference values assume a constant rotational speed of 5000 r/min.

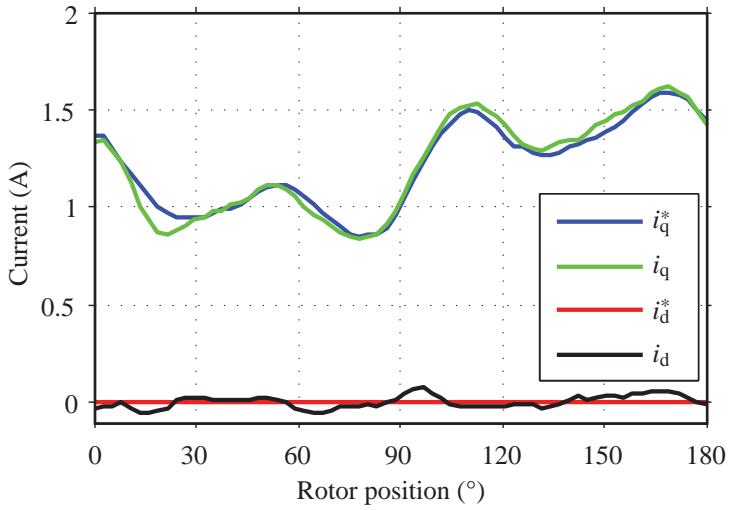


**Figure 5.29:** Reference and measured values of  $i_d$  and  $i_q$  resulting in a smooth torque. The reference values assume a constant rotational speed of 40 000 r/min.

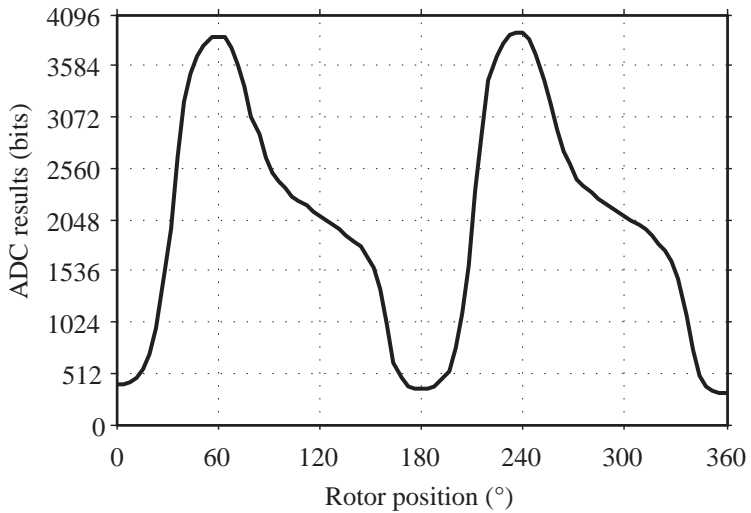


**Figure 5.30:** Signal containing the rotor position as sampled by the ADC of the DSP after the measurement, filtering and demodulation stages. The full range of the 12-bit ADC is utilized for rotor position extraction leading to a high-sensitivity measurement.

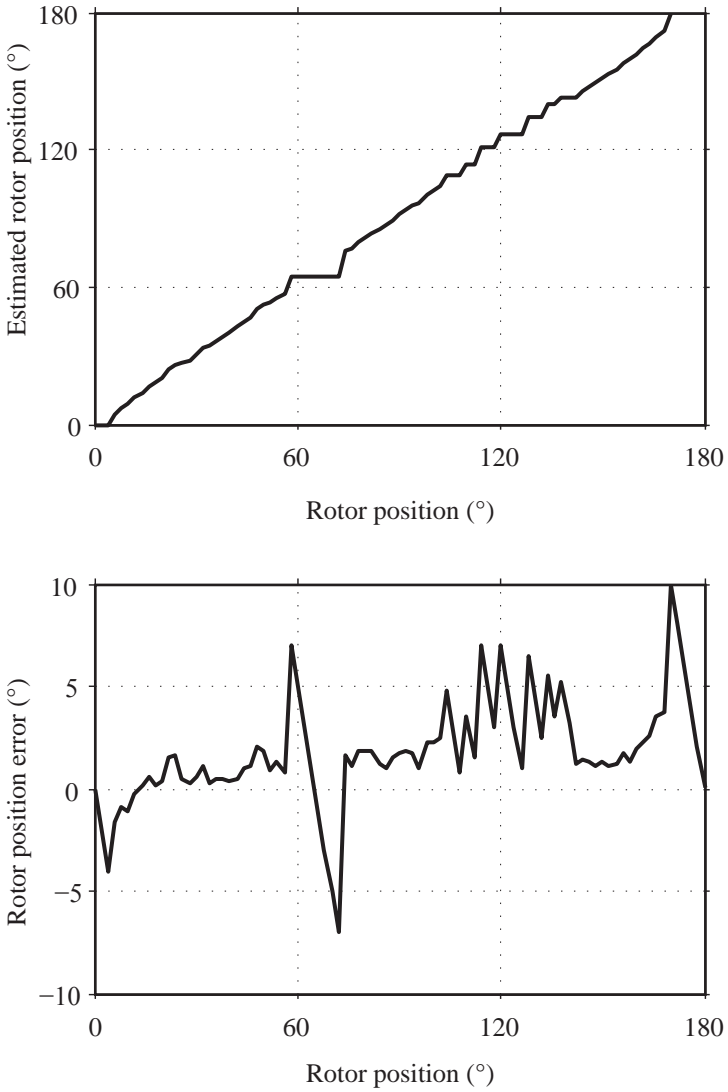


**Figure 5.31:** Experimental results of the rotor position estimation. The average error is  $2.3^\circ$  when two look-up tables are used with 56 16-bit entries between  $0^\circ$  and  $60^\circ$  and 128 16-bit entries between  $60^\circ$  and  $180^\circ$ .

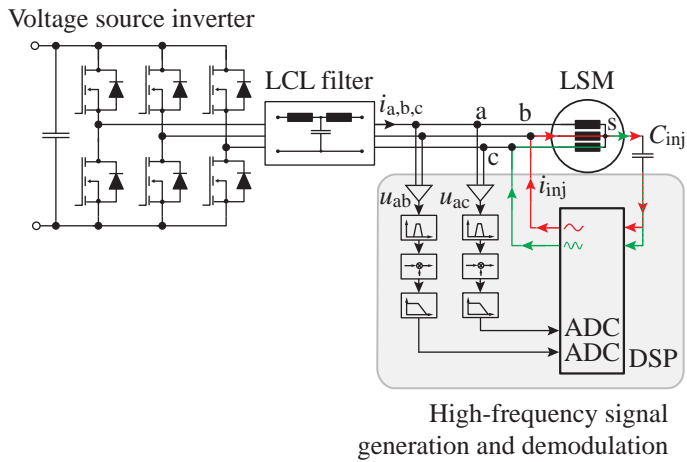


**Figure 5.32:** Drive system with a modified topology for the dedicated rotor position estimation hardware. In this configuration, two signals with different frequencies are injected into the machine in order to obtain the direction of rotation.

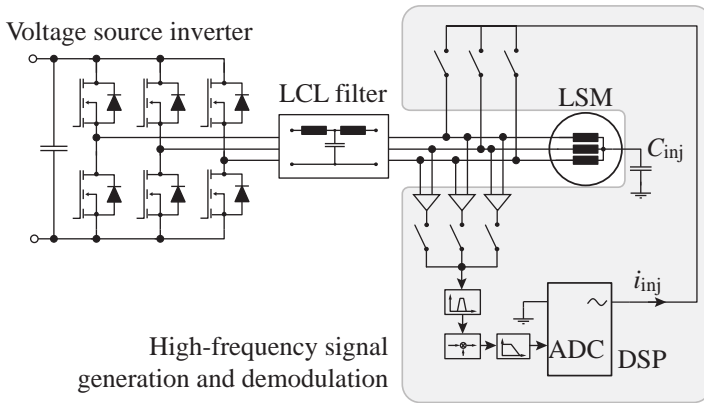


**Figure 5.33:** Drive system with modified topology for the dedicated rotor position estimation hardware. In this configuration, the high-frequency signal is injected into different machine phases sequentially in order to obtain the direction of rotation.



# Chapter 6

## Position estimation using sensing coils

### 6.1 Introduction

The previous chapter of this thesis showed a high-frequency signal injection method for tracking the phase impedance of an electrical machine and estimating the rotor position based on the measured impedance. The high-frequency signal is generated using dedicated hardware, avoiding any modification of the inverter operation (e.g. increasing the switching frequency or modifying the switching pattern). The response of the machine to the injected high-frequency signal is read using differential measurements, which allows for a high-sensitivity estimation even for low-saliency machines. Even though the LSM is not a low-saliency machine, this makes the proposed method very suitable for slotless PM machines that are commonly used for applications above 200 000 r/min.

The phase inductances of the LSM depend strongly on the rotor position, which is a desired property for impedance-tracking-based rotor position estimation algorithms. However, the phase inductance also depends heavily on the load due to the load-dependent saturation of the stator of the LSM. Figure 6.1 shows  $\hat{u}_{ac}$ , the amplitude of the differentially measured voltage response of the LSM when a high-frequency current is injected in the machine as described in the previous section, for different stator currents (i.e. different machine loads). Even though the response of the machine to the injected signal still contains rotor

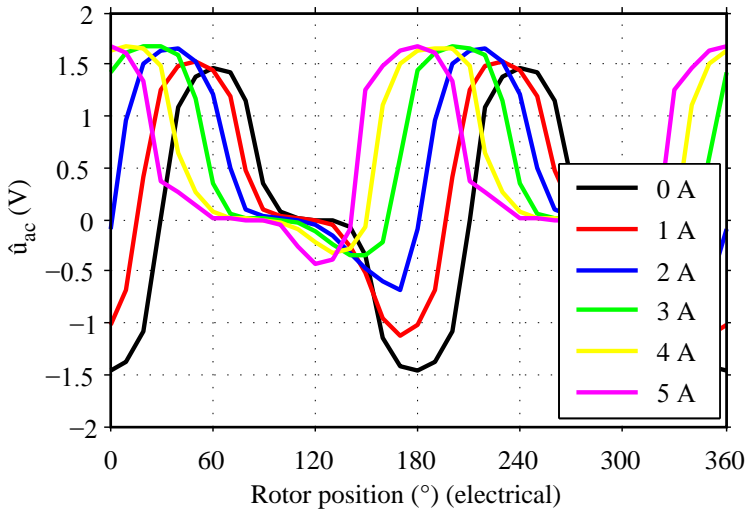


**Figure 6.1:** The amplitude of the machine’s response to the high-frequency current injection as described in the previous chapter for different rotor positions and different loads. As also described in Figure 5.3, the peak value of the machine’s response is defined as  $\hat{u}_{ac} = (M_{ba} - M_{bc})2\pi f_{inj}\hat{i}_{inj}$ , therefore, the negative values of  $\hat{u}_{ac}$  should be interpreted as the rotor positions where  $M_{ba} < M_{bc}$ .

position information, the dependency of the machine’s response to the rotor position changes significantly with load. This means that different look-up tables are needed for different load levels, which makes the implementation more complicated.

Another shortcoming of this method, which is also mentioned at the end of the previous chapter, can be revealed by a closer look at the zero stator current case in Figure 6.1. Even though  $\hat{u}_{ac}$  depends on the rotor position, the information contained in it is not enough to estimate the direction of rotation. For estimating the direction of rotation, a second channel of injection is needed. Different ways of implementing a second injection channel are shown in the previous section.

Figure 6.2 shows the mutual inductances between the phases of the first LSM prototype for different rotor positions at no-load. Similarly, Figure 6.3 shows the self inductances of the phases of the same machine at no-load. For the machine under consideration, all the self

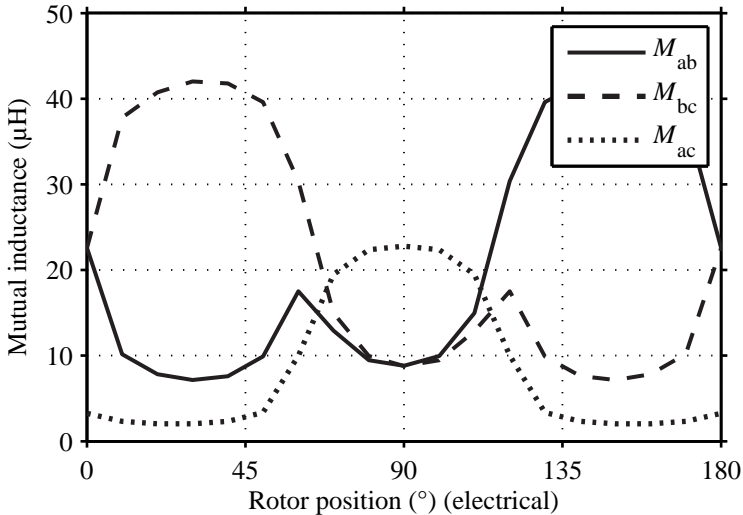


**Figure 6.2:** Mutual inductances between the phases of the first LSM prototype for different rotor positions at no-load.

and mutual inductances go flat at the same rotor position, making an impedance-based position estimation impossible at certain rotor positions regardless of the way the impedance is measured. This leads to the conclusion that an LSM optimized to maximize the torque for given copper losses while producing less no-load losses than a given limit is not necessarily suitable for a low-speed self-sensing position estimation method. Therefore, in this chapter, a new method is presented for sensing the rotor position of an LSM. Even though analyzed on a specific type of electrical machine, the presented method can be used for position estimation of several other types of electromechanical actuators.

## 6.2 Concept description

The shielding iron is an inherent part of the section-type LSM. It is needed to guide the flux of the magnets that are not facing the stator, such that the magnetic fields stay in a confined and controlled space. Even though it does not effect the mean torque capability of the machine, the geometry of the shielding iron may change the cogging torque

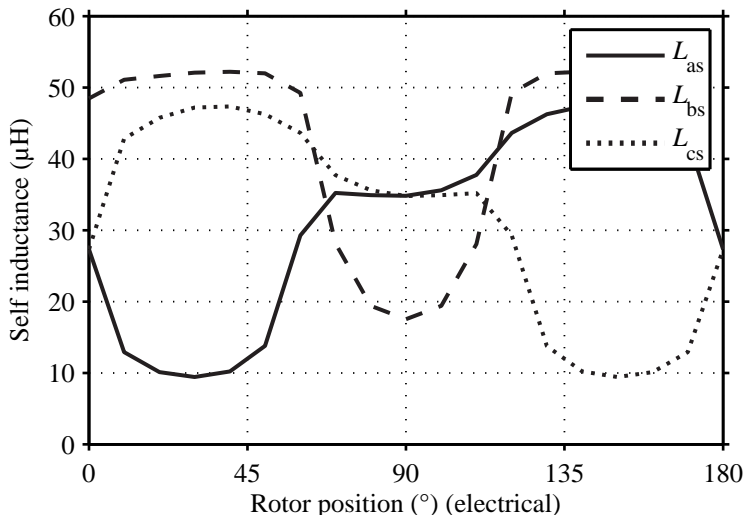


**Figure 6.3:** Self inductances of the phases of the first LSM prototype for different rotor positions at no-load.

and magnetic pull acting on the rotor as it changes the field distribution around the rotor.

Sensing coils can be wound on the shielding iron as shown in Figure 6.4. The position  $\alpha_{sc}$  of a sensing coil can be chosen freely as long as the mechanical construction permits, which is not the case when the machine phases are used for position sensing in a self-sensing approach. Furthermore, as clearly seen in Figure 6.5, the magnetic circuit is nearly not influenced by the field generated by the drive currents, which means that the rotor position estimation is not significantly affected by the load. On the other hand, the sensing coils increase the complexity of the machine production and increase the number of total cables between the machine and the inverter.

## 6.3 2-D FEM simulations

2-D FEM simulations are used to calculate the inductance of a sensing coil placed at different angles  $\alpha_{sc}$ , for different rotor positions. Figure 6.6 shows the self inductances of the sensing coils wound between

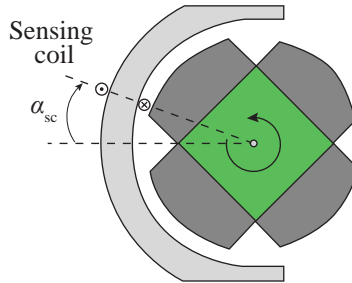


**Figure 6.4:** The placement of a sensing coil on the shielding iron of an LSM.

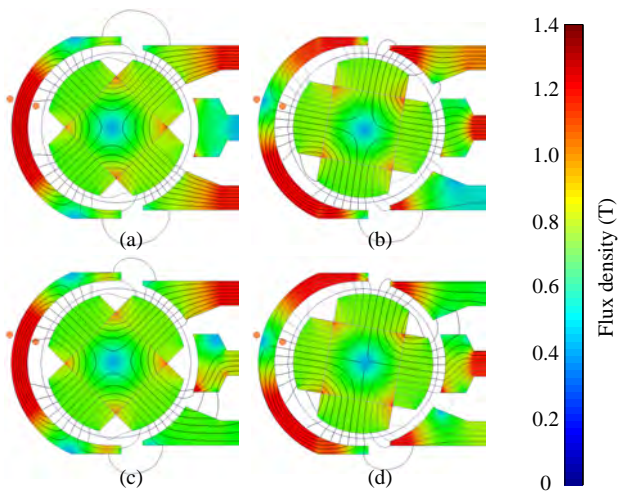


**Figure 6.5:** 2-D FEM simulations showing the field distribution in the shielding iron and the tips of the stator legs of the LSM. Rotor is at  $0^\circ$  (electrical) in (a) and (c) and at  $70^\circ$  (electrical) in (b) and (d). (a) and (b) show no-load and (c) and (d) show full-load condition. The sensing coil is placed at  $\alpha_{sc} = 15^\circ$  in all cases. It can be seen that the field distribution in the shielding iron mainly depends only on the rotor position and is not significantly affected by the machine's load.

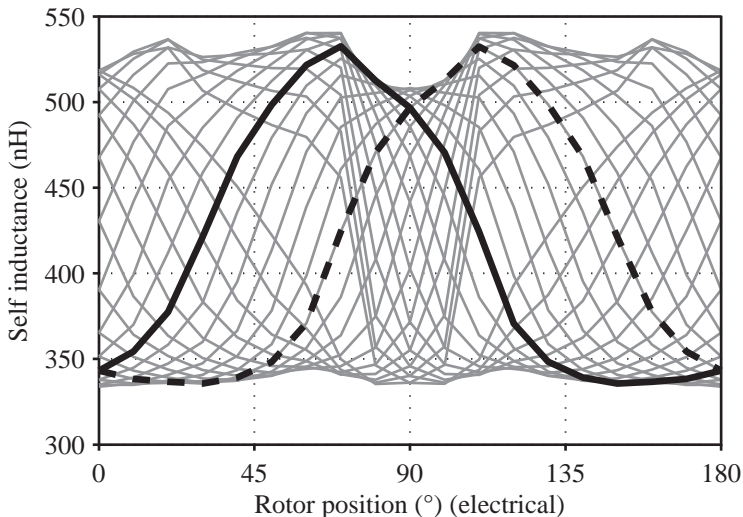


**Figure 6.6:** 2-D FEM analysis results showing the self inductances of the sensing coils placed at positions from  $-60^\circ$  to  $60^\circ$ . Solid and dashed black lines show  $\alpha_{sc} = 15^\circ$  and  $\alpha_{sc} = -15^\circ$ .

$\alpha_{sc} = -60^\circ$  and  $\alpha_{sc} = 60^\circ$  with  $10^\circ$  steps. The number of turns is assumed to be 5. It can be seen that the inductances of the coils at  $\alpha_{sc} = -15^\circ$  and  $\alpha_{sc} = 15^\circ$  can be used for estimating the rotor position as well as the direction of rotation.

The shape of the curves shown in Figure 6.6 can be better understood by looking at Figure 6.6 and Figure 6.5 together. The inductance of a sensing coil is at its minimum when the permanent magnet field pushes the part of iron under the sensing coil into saturation; and contrarily, it is at its maximum when the iron underneath is furthest away from saturation.

As the waveforms shown in Figure 6.6 have double the electrical frequency, they cannot be used to estimate the initial rotor position. In applications where the machine is not loaded at the start-up, the inverter can set the initial rotor position; whereas an initial rotor position sensing method, e.g. based on voltage pulses, can be implemented in applications where this is not possible [49].

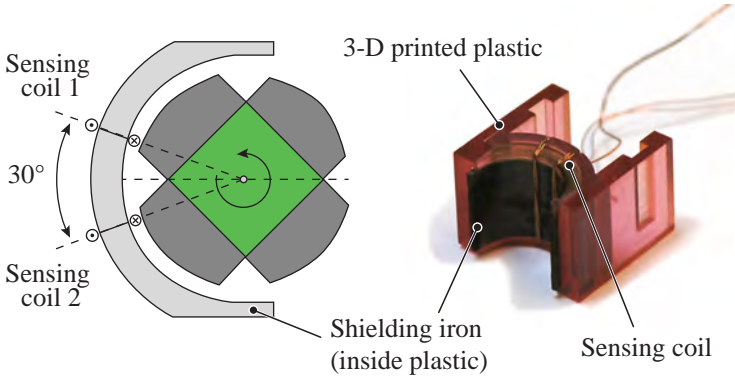


**Figure 6.7:** Cross-sectional view and a photo of a setup with two sensing coils placed at  $\alpha_{sc} = 15^\circ$  and  $\alpha_{sc} = -15^\circ$ . The photo shows a modified plastic chamber geometry that has slots for the sensing coils and additional features that interlock to the aluminum housing for taking the parts out of the housing easier for deceleration tests.

## 6.4 Hardware realization of sensing coils

Figure 6.7 shows a photo of the sensing coils wound around the shielding iron. Two 0.2 mm x 0.3 mm slots are introduced on the plastic chamber to facilitate the winding of the sensing coils. Each sensing coil has 5 turns.

After winding the two sensing coils on a shielding iron, an impedance analyzer (Agilent 4294A) is used to measure the impedance of the sensing coils at different rotor positions at standstill. Figure 6.8 shows the resistance  $R_{sc}$  and inductance  $L_{sc}$  of the sensing coils when a sensing coil is modeled with a series  $R$ - $L$  circuit and the measured impedance is  $Z_{sc} = R_{sc} + j\omega_{ia}L_{sc}$ ,  $\omega_{ia} = 2\pi f_{ia}$  and  $f_{ia} = 1$  MHz.

The measurement results show that the 2-D FEM simulations were able to predict the variation of the sensing coil inductance  $L_{sc}$  with the rotor position accurately. The measurement results also show that the sensing coil resistance  $R_{sc}$  also changes with the rotor position, and its dependency on the rotor position follows that of the  $L_{sc}$ . The measured coil resistance  $R_{sc}$  not only consists of the resistance of the copper used in the coils, but also reflects the losses generated by the measurement

signal in the shielding iron (core losses) and the rotor (eddy-current losses) at the injection frequency  $f_{inj}$ . When the external proximity losses in the sensing coils due to the rotation of the permanent magnets are neglected, the losses in the copper do not change with rotor position, but the core and eddy-current losses do, making  $R_{sc}$  a function of the rotor position for a constant injection frequency. This is explained in Figure 6.9. The permanent-magnet field in the shielding iron drives the major hysteresis loop whereas the minor loops are caused by the high-frequency signal injection used for impedance measurement. The coil inductance  $L_{sc}$  is high when the local slope of the major hysteresis curve is high, i.e. the operating point is close to the origin and far from saturation. The area of the minor hysteresis loops are large in this region, which leads to higher core losses and therefore a higher coil resistance  $R_{sc}$ . On the contrary, when the local slope of the major hysteresis curve is smaller, the coil inductance is lower, and so is the area of the minor loops, the core losses and consequently the coil resistance. Furthermore, when the coil inductance is higher, the higher flux generated by the injected current induces higher eddy-current losses in the conducting bodies of the rotor, increasing  $R_{sc}$ .

## 6.5 Design of sensor electronics

Figure 6.10 shows a functional block diagram of the sensor electronics. The DSP is used to generate a rectangular signal, which is low-pass filtered using an active filter which also acts as a buffer and provides the injection current. The capacitor  $C_{hf}$  blocks the DC and low-frequency components whereas a  $R_{lim}$  with sufficiently large resistance limits the current and makes the system behave as a high-frequency current source. The voltage  $u_{sc}$  is high-pass filtered in order to remove the induced voltage in the coil due to the rotation of the magnet field (back EMF). The demodulation of the signal is realized in a slightly different way compared to the method shown in the previous sections, using an inverting amplifier and an analog switch. Finally, a low-pass filter is used to obtain the rotor position containing signal that can be sampled by the DSP. The injection and measurement channel described here is built twice as there are two sensing coils wound on the shielding iron, as shown in Figure 6.11.

In the configuration shown in Figure 6.11, the voltages measured at the terminals of the sensing coils  $u_{sc,1}$ ,  $u_{sc,2}$  can be expressed as

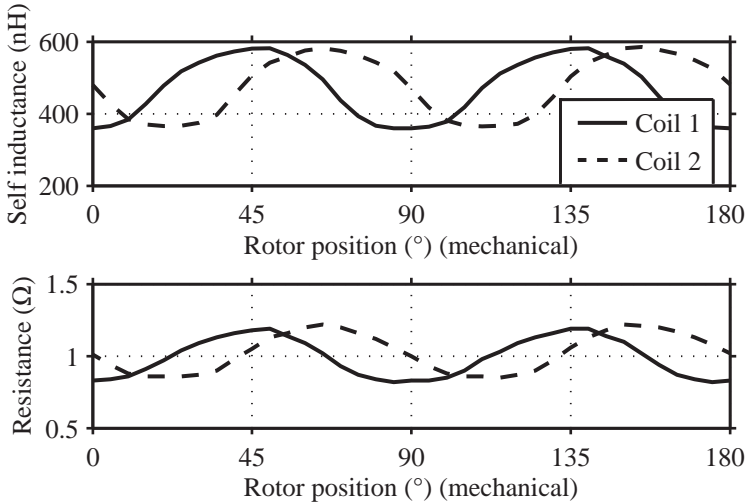


**Figure 6.8:** Series resistance  $R_{sc}$  and self inductance  $L_{sc}$  of the sensing coils measured using an impedance analyzer.

$$u_{sc,1} = i_{sc,1}R_{sc,1} + L_{sc,1}\frac{di_{sc,1}}{dt} + M_{sc}\frac{di_{sc,2}}{dt} + e_{sc,1}, \quad (6.1)$$

$$u_{sc,2} = i_{sc,2}R_{sc,2} + L_{sc,2}\frac{di_{sc,2}}{dt} + M_{sc}\frac{di_{sc,1}}{dt} + e_{sc,2}, \quad (6.2)$$

where  $M_{sc}$  is the mutual inductance between the two sensing coils and  $e_{sc,1}$  and  $e_{sc,2}$  are the back EMF in the first and second sensing coils caused by the rotation of the rotor permanent magnets, respectively.

The high-pass filter suppresses the back EMF, therefore  $e_{sc,1}$  and  $e_{sc,2}$  are not considered any further in the analysis. As only sinusoidal injection currents are considered and the amplitudes of the injected currents are too small to lead to any saturation-related distortions in the voltage response of the machine (i.e.  $L_{sc}$  changes only with rotor position and not with injected current), the voltage drops on the coil resistances and inductances are sinusoidal and  $90^\circ$  phase shifted. This means that the demodulation angle gives a degree of freedom on how

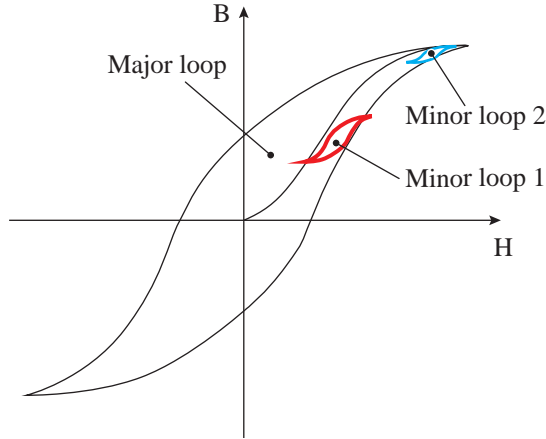


**Figure 6.9:** Major and minor hysteresis loops of the shielding iron core material. The permanent-magnet flux drives the major loop whereas the minor loops are caused by the high-frequency signal injection.

to synthesize the voltage that will be sampled by the DSP after being low-pass filtered.

This can be explained easily on a setup with only one sensing coil and no back EMF as

$$u_{sc}(t) = \hat{i}_{sc} R_{sc} \cos(\omega_{inj} t) + \hat{i}_{sc} \omega_{inj} L_{sc} \cos(\omega_{inj} t - \frac{\pi}{2}). \quad (6.3)$$

When a demodulation signal in the form of  $u_{dm}(t) = \cos(\omega_{inj} t - \phi_{dm})$  is used where  $\phi_{dm}$  is the demodulation angle, the demodulated signal can be written as

$$u_{sc, dm}(t) = u_{sc}(t) u_{dm}(t), \quad (6.4)$$

$$u_{sc, dm}(t) = (\hat{i}_{sc} R_{sc} \cos(\omega_{inj} t) + \hat{i}_{sc} \omega_{inj} L_{sc} \cos(\omega_{inj} t - \frac{\pi}{2})) (\cos(\omega_{inj} t - \phi_{dm})), \quad (6.5)$$

$$u_{sc, dm}(t) = \hat{i}_{sc} R_{sc} A + \hat{i}_{sc} \omega_{inj} L_{sc} B, \quad (6.6)$$

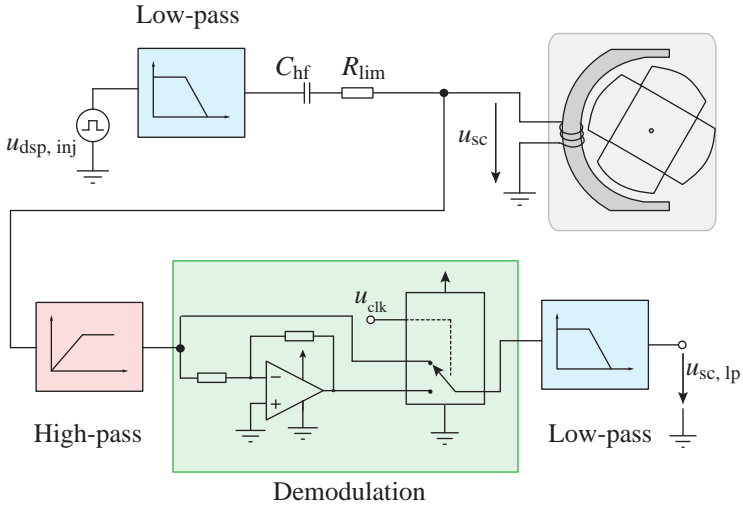


**Figure 6.10:** Block diagram of the high-frequency signal injection, measurement, filtering and demodulation for rotor position estimation using sensing coils. Only one sensing coil is shown for simplicity.

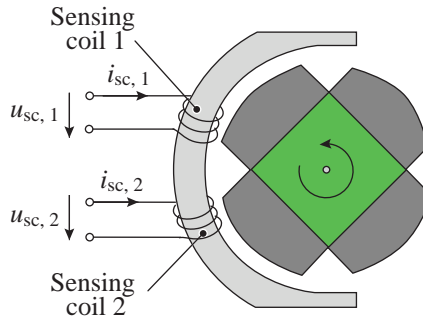


**Figure 6.11:** Two sensing coils on the shielding iron of a section-type LSM.

where

$$A = \frac{\cos(2\omega_{\text{inj}}t - \phi_{\text{dm}})}{2} + \frac{\cos(\phi_{\text{dm}})}{2}, \quad (6.7)$$

and

$$B = \frac{\cos(2\omega_{\text{inj}}t - \frac{\pi}{2} - \phi_{\text{dm}})}{2} + \frac{\cos(\phi_{\text{dm}} - \frac{\pi}{2})}{2}. \quad (6.8)$$

As the the low-pass filter suppresses the components of  $A$  and  $B$  that oscillate with twice the injection frequency, the low-pass filtered signal  $u_{\text{sc,lp}}$  is expressed as

$$u_{\text{sc,lp}} = \hat{i}_{\text{sc}} R_{\text{sc}} \frac{\cos(\phi_{\text{dm}})}{2} + \hat{i}_{\text{sc}} \omega_{\text{inj}} L_{\text{sc}} \frac{\cos(\phi_{\text{dm}} - \frac{\pi}{2})}{2}. \quad (6.9)$$

From (6.9) it can be concluded that the demodulation angle  $\phi_{\text{dm}}$  can be used to read either the voltage drop on the coil resistance, or the voltage drop on the coil inductance, or a combination of both. The equations (6.3) - (6.9) are derived on a setup with one sensing coil, i.e. without any mutual coupling. However, when mutual coupling from a neighboring sensing coil is present, depending on the phase angle  $\phi_{\text{p}}$  between the injected currents, the demodulation angle  $\phi_{\text{dm}}$  can be used to cancel the mutual coupling similarly.

Figure 6.12(a) shows the phasor diagram of a case where  $\phi_{\text{p}} = 90^\circ$  phase shifted currents are injected in two sensing coils with a mutual inductance  $M_{\text{sc}}$  between them. For each sensing coil, the demodulation angle  $\phi_{\text{dm}}$  can be set independently depending on what quantity is to be read from that channel, ( $u_{\text{sc,lp,1}}$  and  $u_{\text{sc,lp,2}}$  can be interpreted as the projections of the sensing coil voltages  $u_{\text{sc,1}}$  and  $u_{\text{sc,2}}$  on the dashed lines). For example, in Figure 6.12(a),  $\phi_{\text{dm,1}} = 0^\circ$  leads to the reading of the difference of the voltage drop on the first coil's resistance and induced voltage across the mutual reactance ( $u_{\text{sc,lp,1}} = i_{\text{sc,1}} R_{\text{sc,1}} - i_{\text{sc,2}} \omega_{\text{inj}} M_{\text{sc}}$ ); whereas  $\phi_{\text{dm,2}} = 90^\circ$  omits the resistive voltage drop and the mutual coupling, and leads to the reading of the voltage drop across the phase inductance of the second coil only ( $u_{\text{sc,lp,2}} = i_{\text{sc,2}} \omega_{\text{inj}} L_{\text{sc,2}}$ ).

Similarly, for the case shown in Figure 6.12(b) where  $\phi_{\text{p}} = 180^\circ$ ,  $\phi_{\text{dm,1}} = 0^\circ$  enables the measurement of only the resistive voltage drop on the first coil's resistance ( $u_{\text{sc,lp,1}} = i_{\text{sc,1}} R_{\text{sc,1}}$ ); whereas  $\phi_{\text{dm,2}} = 90^\circ$  leads to the reading the difference of the voltage drop across the self inductance of the second coil and the induced voltage across the mutual inductance ( $u_{\text{sc,lp,2}} = i_{\text{sc,2}} \omega_{\text{inj}} L_{\text{sc,2}} - i_{\text{sc,1}} \omega_{\text{inj}} M_{\text{sc}}$ ).

The degree of freedom introduced by the independently adjustable  $\phi_{\text{p}}$ ,  $\phi_{\text{dm,1}}$  and  $\phi_{\text{dm,2}}$  enables the synthesis of the required waveform at

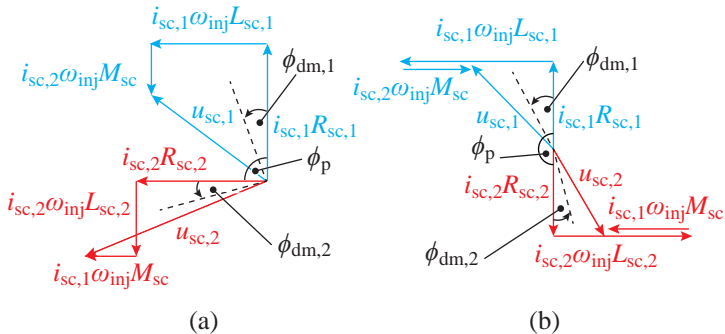


**Figure 6.12:** Phasor diagram of the induced voltages in two sensing coils on one shielding iron due to the injected signals (back EMF is omitted). Blue and red denote voltages induced in different sensing coils. (a) The currents injected in the sensing coils are  $90^\circ$  phase shifted. (b) The currents injected in the sensing coils are  $180^\circ$  phase shifted.

the output of the demodulation stage, giving the designer the flexibility to shape the voltage  $u_{sc,lp}$  sampled by the DSP. This may be used to maximize the rotor position sensing sensitivity for a given machine and sensor coil geometry, as explained in the following sections.

## 6.6 Further design aspects

So far, it has been shown that the position of the sensing coil  $\alpha_{sc}$ , the phase displacement between the injected currents  $\phi_p$ , and the demodulation angles  $\phi_{dm,1}$ ,  $\phi_{dm,2}$  all influence the shape of the signal  $u_{sc,lp}$ , which contains the rotor position information. Clearly, the set of these parameters needs to be selected such that the DSP sampling the resulting  $u_{sc,lp}$  of different sensing coils can estimate the rotor position based on these voltages in a computationally efficient way (e.g. using a look-up table), at all rotor positions. That is, the voltages should not go flat or reach their maxima/minima at the same rotor position. Clearly, the proper selection of these parameters depends strictly on the application, and a universally optimum set of parameters cannot be defined. Nevertheless, the above-mentioned design parameters are dis-

cussed here along with several others in order to present a complete set of guidelines for applying the analyzed method in various other position sensing applications.

The position  $\alpha_{sc}$  of a sensing coil is the first degree of freedom in order to modify the dependency of its impedance on the rotor position. However, mechanical constraints may limit where the sensing coil can be placed. In such a case,  $\phi_p$ ,  $\phi_{dm,1}$ ,  $\phi_{dm,2}$  can be modified in order to modify  $u_{sc,lp}$ . As a different example, an application where the iron is not pushed deeply into saturation can be considered. The self and mutual inductances of the sensing coils then do not depend strongly on the rotor position, but depending on the position of the sensing coil with respect to the conductive bodies in the rotor, the eddy-current losses induced in the rotor may lead to a rotor-position-dependent sensing coil resistance. This can be read without the effect of the sensing coil inductance as shown in Figure 6.12, by setting  $\phi_p = 180^\circ$  and  $\phi_{dm,1} = \phi_{dm,2} = 0^\circ$ . Different  $u_{sc,lp}$  measurements taken for different combinations of  $\phi_p$ ,  $\phi_{dm,1}$  and  $\phi_{dm,2}$  are presented in the following section.

In order to maintain a continuous rotor position sensing and to estimate the direction of rotation, at least two sensing coils are required. A higher number of sensing coils can be implemented for redundancy, but the additional manufacturing effort and the space limits need to be considered.

The number of turns of a sensing coil, as in windings of electric machines, changes the ratio of current and voltage supplied by the driving electronics. However, as the power consumption of the sensor electronics is typically much smaller than the drive power, this has almost no practical importance. A higher number of turns means smaller wire radius for a given slot area, and in small systems such as the LSM analyzed in this work (with  $0.06 \text{ mm}^2$  slot area), a practical limit exists on the thinnest wire that can be used without a complicated winding method where the tension on the wire is precisely controlled. On the other hand, the lead wires of the sensing coils add a rotor-position-independent offset to the sensing coil impedance, whose ratio to the rotor-position-dependent impedance can be decreased by using a high number of turns. Twisting of the lead wires further decreases this impedance offset.

Injection frequency  $f_{inj}$  has to be selected sufficiently higher than the highest-frequency component of the back EMF induced in the sensing coils at the maximum rotor speed. The impedance  $Z_{sc}$  of a sensing

coil depends on  $f_{\text{inj}}$  as its inductance  $L_{\text{sc}}$  decreases and the resistance  $R_{\text{sc}}$  increases with increasing  $f_{\text{inj}}$ . Even though the magnetic circuit is decoupled from the drive currents, parasitic coupling may occur when the signal and power electronics share the same circuit board, which should also be considered when selecting  $f_{\text{inj}}$  in order to avoid any possible parasitic crosstalk.

The magnetic material on which a sensing coil is wound has a significant effect on its impedance. In applications where the magnetic material on which the sensing coils are wound can be selected, the designer should consider the permeability and the core losses of the material at the injection frequency as well as at the maximum electrical frequency of the rotor in order to guarantee a position dependent impedance at all rotor speeds, without unfeasibly high core losses.

Finally, the corner frequency of the low-pass filter has to be selected to pass all the significant harmonics of the  $u_{\text{sc,lp}}$  at the highest rotor speed. For example, considering the waveform shown with the solid line in Figure 6.6, signals up to the sixth harmonic need to be considered, which occurs at 80 kHz when the machine speed is 200 000 r/min.

## 6.7 Measurement results

Following the analysis described above, the signal electronics is realized in hardware to verify the design procedure. However, after the low-pass filters, simple analog subtraction and gain stages are utilized with variable resistors and operational amplifiers in order to be able to shift and scale the signals easily during measurements. In this section, the signals noted as  $u_{\text{sc,lp}}$  are demodulated and filtered as described above; and additionally they are shifted and scaled before being measured. The final variable shifting and scaling stage makes the hardware suitable for testing different sensing coils and different demodulation strategies, and it can be omitted in a final design where the sensing coil and the demodulation type are defined.

Even though a precise estimation of the back EMF in the sensing coils is not directly needed for rotor position estimation, the expected back EMF needs to be known in order to design the high-pass filter properly. Figure 6.13 shows the induced back EMF in the sensing coils when the rotor is rotating at 200 000 r/min. There is a very good correlation between the simulated and measured waveforms which verifies the FEM model.

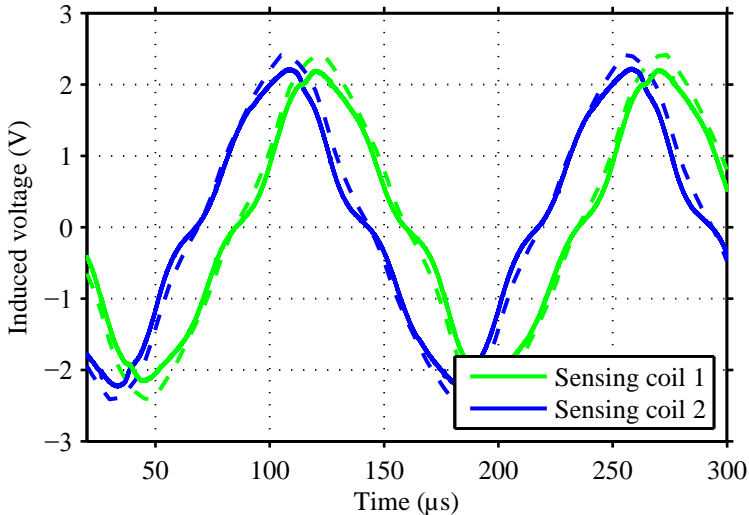


**Figure 6.13:** Measured and simulated back EMF at 200 000 r/min. Solid lines shows measured and dashed lines shows simulated waveforms.

The simulation results for the self inductances for the two sensing coils with 5 turns each as well as the mutual inductance between them can be seen in Figure 6.14. Figure 6.15 shows  $u_{sc,lp}$ , the demodulated and filtered signal that is fed to the DSP, at (top) 10 000 r/min, (middle) 100 000 r/min and (bottom) 200 000 r/min. For this measurement, the currents injected in the two sensing coils are  $\phi_p = 90^\circ$  shifted and the demodulation signals in both channels are adjusted to read only the self inductances and cancel out the resistances and the mutual coupling ( $\phi_{dm,1} = \phi_{dm,2} = 90^\circ$ ). The waveform stays the same throughout the whole speed range, which verifies the design of the filters. As clearly seen, the back EMF is successfully attenuated up to 200 000 r/min. A comparison to the simulated self inductances shown in Figure 6.14 reveals that the waveforms look similar, hence the effect of the mutual coupling is canceled out and the self inductances are read as intended.

Figure 6.16 shows the high-pass filtered voltages before demodulation, where a high-frequency current is injected in only one sensing coil. The envelopes of the signals are visible at the top, whereas the bottom

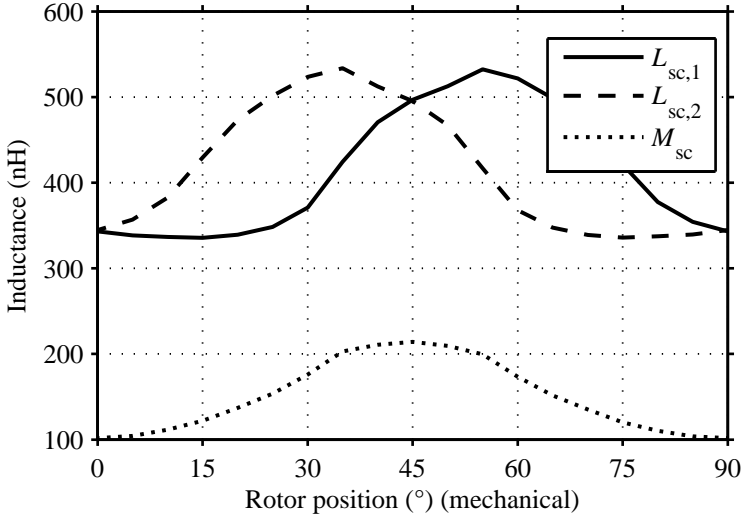


**Figure 6.14:** 2-D FEM simulation results showing the self inductances  $L_{sc,1}$  and  $L_{sc,2}$  of the two sensing coils as well as their mutual inductance  $M_{sc}$ , for different rotor positions. The number of turns is 5.

plot shows a close-up of the same measurement with a shorter period. The amplitudes of the signal envelope are calculated offline and plotted in Figure 6.17. Here, the larger signal relates to the self inductance and the resistance of the sensing coil where the high-frequency current is injected, and the smaller signal is proportional to the voltage induced in the other (open circuited) sensing coil, hence relates to the mutual inductance. The machine is rotating at 10 000 r/min.

Figure 6.18 shows the simulated values for the sum of self and mutual inductance for both sensing coils in the top plot. In order to read the sum of self and mutual inductances without the resistive voltage drops, the currents in both sensing coils are in phase ( $\phi_p = 0^\circ$ ), and the demodulation angles are set as  $\phi_{dm,1} = \phi_{dm,2} = 90^\circ$ . The bottom plot shows the resulting  $u_{sc,lp}$ , whose waveform is virtually identical to that of the simulation results shown in the top plot. The machine is rotating at 10 000 r/min and the amplitudes of the high-frequency currents injected in the machine are  $\hat{i}_{sc} = 20$  mA.

Finally, Fig. 6.19 shows the simulation results for the difference of

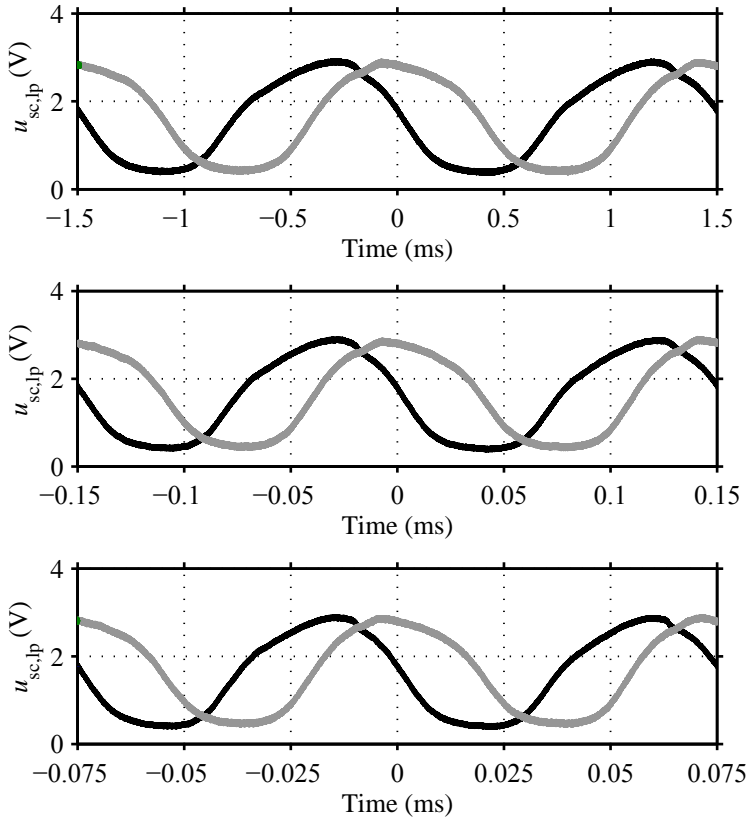


**Figure 6.15:** The demodulated and filtered signal  $u_{sc,lp}$  fed to the DSP, measured at three different speeds. Black and gray denote the signals from two different channels (two different sensing coils). (Top) 10 000 r/min, (middle) 100 000 r/min and (bottom) 200 000 r/min. The currents injected in the two sensing coils are  $\phi_p = 90^\circ$  phase shifted and the demodulation signals in both channels are adjusted to read only the self inductances and cancel out the resistive voltage drops and the effect of mutual coupling ( $\phi_{dm,1} = \phi_{dm,2} = 90^\circ$ ).

self and mutual inductances for both sensing coils in the top, whereas the bottom plot shows the  $u_{sc,lp}$  that is shaped to follow the same

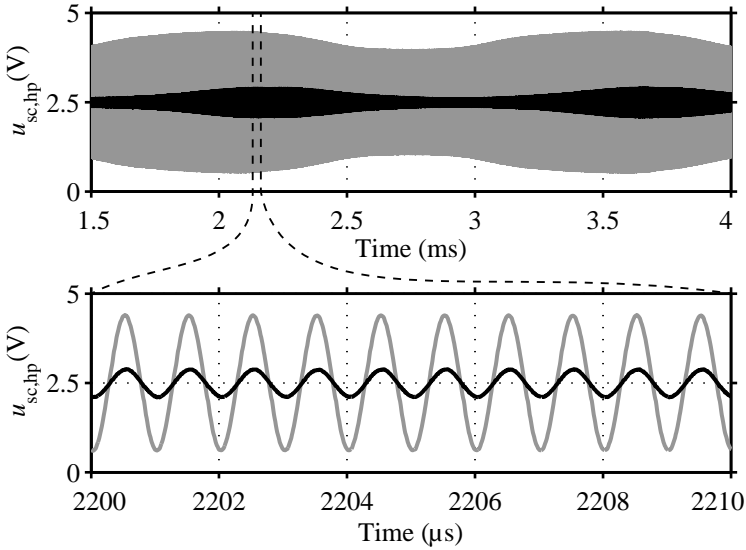


**Figure 6.16:** The high-pass filtered voltage responses of sensing coils when a high-frequency signal is injected only in one sensing coil (the second one is open-circuited). (Top) Gray is the voltage response of the sensing coil where the current is injected. It relates to the voltage drops on the self inductance and the resistance. Black is the voltage induced in the open-circuited sensing coil due to the mutual coupling; hence it relates to the mutual inductance. (Bottom) Close-up of the same measurement with a shorter period.

waveform by injecting  $\phi_p = 180^\circ$  phase shifted high-frequency currents in the sensing coils and adjusting the demodulation angles as  $\phi_{dm,1} = \phi_{dm,2} = 90^\circ$ . During this measurement, the machine speed is 10 000 r/min and the amplitudes of the high-frequency currents are  $\hat{i}_{sc} = 20$  mA.

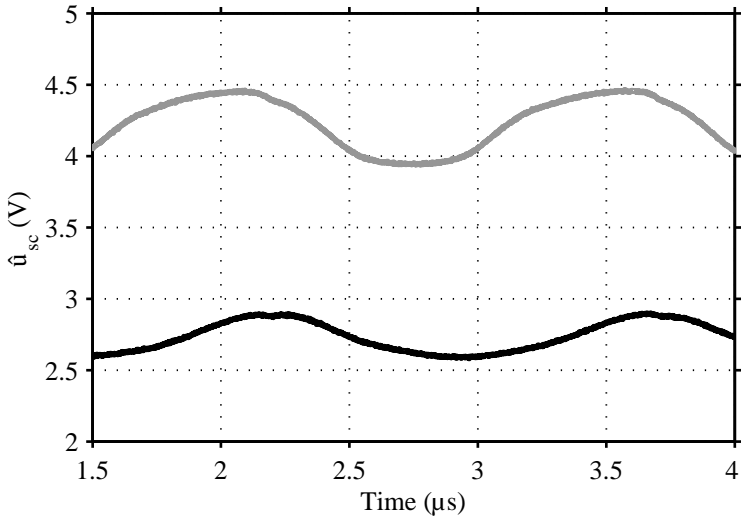


**Figure 6.17:** The amplitudes of the envelopes shown in Figure 6.16 (calculated offline). The gray waveform relates to the self inductance and resistance and the black waveform relates to the mutual inductance.

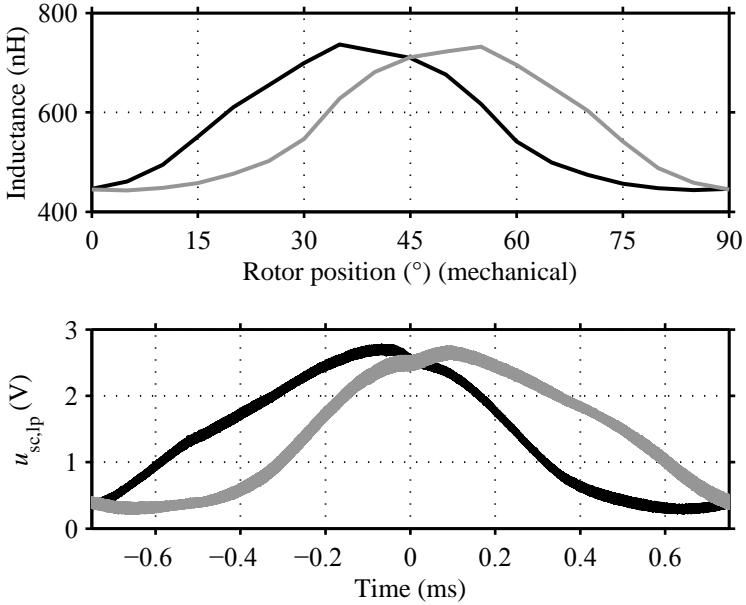


**Figure 6.18:** Simulated and measured values for the sum of self and mutual inductances for two sensing coils. (Top) Simulated inductances. (Bottom) The measured voltage responses of the sensing coils after filtering and demodulation stages. In order to read the sum of self and mutual inductances and omit the resistive voltage drops, the currents in both sensing coils are in phase ( $\phi_p = 0^\circ$ ), and the demodulation angles are  $\phi_{dm,1} = \phi_{dm,2} = 90^\circ$ . The machine speed is 10000 r/min and the amplitude of the high-frequency currents injected in the machine are  $\hat{i}_{sc} = 20$  mA.

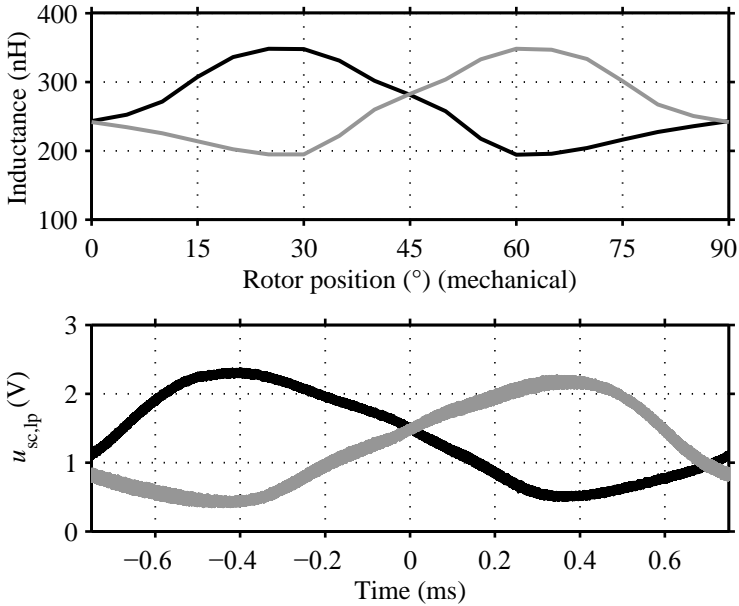


**Figure 6.19:** Simulated and measured values for the difference of self and mutual inductances for two sensing coils. (Top) Simulated inductances. (Bottom) The measured voltage responses of the sensing coils after filtering and demodulation stages. In order to read the difference of self and mutual inductances and omit the resistive voltage drops, the currents in both sensing coils are  $\phi_p = 180^\circ$  phase shifted, and the demodulation angles are  $\phi_{dm,1} = \phi_{dm,2} = 90^\circ$ . The machine speed is 10 000 r/min and the amplitude of the high-frequency currents injected in the machine are  $\hat{i}_{sc} = 20$  mA.

## Chapter 7

# Comparison with the state of the art

In the previous chapters of this thesis, the LSM is introduced for directly driven machining applications where the space at the tool head is limited and where the electrical machine can grow only in one lateral direction. Dental drills are given as an example due to the space limits at the head of the handpiece introduced by ergonomic constraints.

The peculiar shape of the LSM enables a larger electrical machine to be used to drive the same tool. Therefore, the same tool is intuitively expected to be able to deliver a higher power output when driven by an LSM compared to a standard electrical machine that would fit in the tool head. However, so far no quantitative comparison is made between the LSM and standard cylindrical electrical machines. Thus, this chapter deals with the comparison of the LSM and two other types of standard permanent-magnet electrical machines.

Due to their large magnetic air gap, slotless PM machines have weak armature reaction and consequently lower rotor losses [15]. They are therefore well suited for high-speed drive applications with speeds above 200 000 r/min. For example, a 500 000 r/min electrical machine is designed in [5], and another one running at 1 000 000 r/min in [9], both with slotless stators and one-piece diametrically magnetized permanent magnet rotors.

However, even though they are better suited for high-speed applications, the torque density of slotless machines is lower compared to their

slotted counterparts [60]. Slotted machines with concentrated (non-overlapping) windings offer higher torque densities due to their shorter end windings [61]. Therefore, in the following sections of this thesis, the LSM topology is compared to both the one pole-pair slotless machine type with straight distributed windings and the slotted machine type with higher number of poles and concentrated windings. Even though the latter is not a suitable machine topology for high-speed applications due to the higher fundamental frequency and higher rotor losses, it is interesting to compare its torque capability with that of the LSM for applications in confined spaces.

## 7.1 Slotless topology

Figure 7.1 shows the geometry of the slotless machine considered here. The rotor consists of a one-piece, diametrically magnetized cylindrical permanent magnet. In order to transfer the torque to the load and ensure mechanical stability of the rotor at high speeds, a retaining sleeve is needed (the sleeve is not shown in the figure for the sake of simplicity).

The modeling of the slotless machine is done in the same way as the electromagnetic design of the first prototype described in Section 3.2<sup>1</sup>. However, as the main goal of this chapter is to compare the torque capabilities of different machine topologies, the rotor losses are neglected. The machine geometry is parametrized according to Figure 7.1. The stator outer radius  $r_s$  is fixed to 4 mm. The rotor radius  $r_r$  and the winding thickness  $t_w$  are both swept from 0.4 mm to 2.8 mm with 0.4 mm steps, excluding the designs where the sum of the rotor radius, the air gap<sup>2</sup> (fixed to 0.6 mm) and the winding thickness is larger than 3.8 mm. This results in a minimum allowed stator core thickness of 0.2 mm. The rotor is assumed to be made of a diametrically magnetized sintered NdFeB permanent magnet with a remanent flux density of 1.1 T. Amorphous iron (Table 3.1) is assumed as the stator core material, as in the LSM analyzed earlier in this work. A copper filling factor of 0.3 is assumed in the windings. The axial length of the

---

<sup>1</sup>Two FEM simulations are carried out to evaluate each machine at the low-speed high-torque and high-speed, no-load operating points. Air-friction losses are calculated according to [19]. Further details about the modeling approach be found in Section 3.

<sup>2</sup>As the rotor losses are not considered, and as the magnetic permeability of the sleeve is very close to that of air, the sleeve is not included in the model. The space required for the sleeve is accounted for in the air gap.

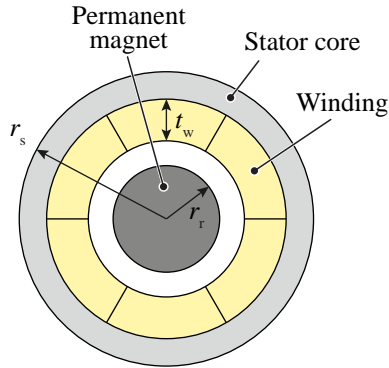


**Figure 7.1:** Cross-sectional view and the geometric parameters of slotless machine.

$T_1$	Mean torque at 6 W copper losses	1.55 mN m
$P_{fe}$	Stator core losses at 200 000 r/min	44 mW
$P_{air}$	Air-friction losses at 200 000 r/min	32 mW
$r_s$	Stator outer radius	4 mm
$r_r$	Rotor radius	1.6 mm
$t_w$	Winding thickness	1.2 mm
$l_a$	Active length	7.4 mm

**Table 7.1:** Key parameters of the slotless machine that generates the highest torque.

machine is set to 7.4 mm, as the LSM described in Section 3.2.

Figure 7.2 shows the mean torque of the analyzed slotless machines when they are driven with stator currents resulting in 6 W of copper losses versus their no-load losses at 200 000 r/min. The no-load losses include stator core losses and air-friction losses. It can be seen that the maximum torque that can be generated using a slotless PM machine that fits in the defined space is 1.55 mN m. Table 7.1 gives the key parameters of the machine that generates the highest torque.

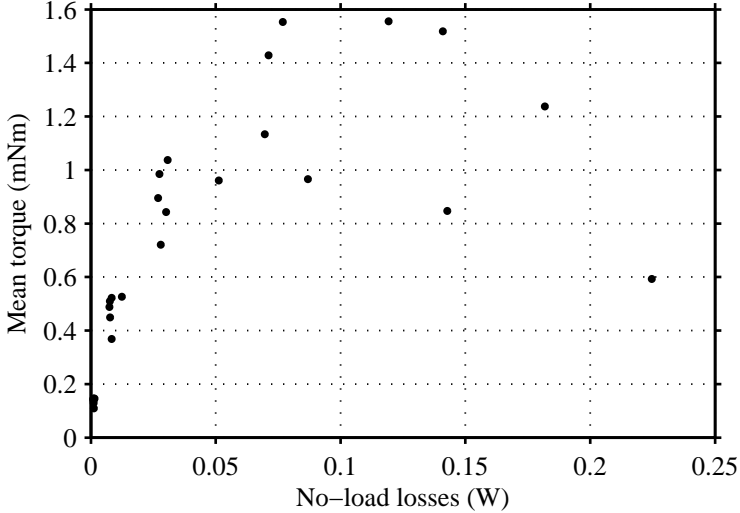


**Figure 7.2:** Performance of the analyzed slotless machines. y-axis shows the mean torque of the machine when producing 6 W copper losses. x-axis shows the no-load losses at 200 000 r/min.

## 7.2 Slotted topology with concentrated windings

The geometry of the analyzed slotted machine is shown in Figure 7.3. As more independent variables are needed to represent the geometry compared to the slotless machine, an analytical model is used in order to assess the performance of this machine type in a computationally efficient way, contrary to the FEM simulations described earlier.

Firstly, the no-load flux in the air gap is calculated according to [20]. Then, the stator tooth width  $w_1$  is dimensioned as

$$w_1 = \frac{r_b}{B_{\text{sat}}} \int_{-\pi/Q}^{\pi/Q} B_{\text{ra}}(\theta_t) d\theta_t, \quad (7.1)$$

where  $B_{\text{ra}}$  is the radial component of the no-load air gap flux density at the stator bore  $r_b$  and  $\theta_t$  is the integration variable in the tangential direction. (7.1) is evaluated at the rotor position where the considered

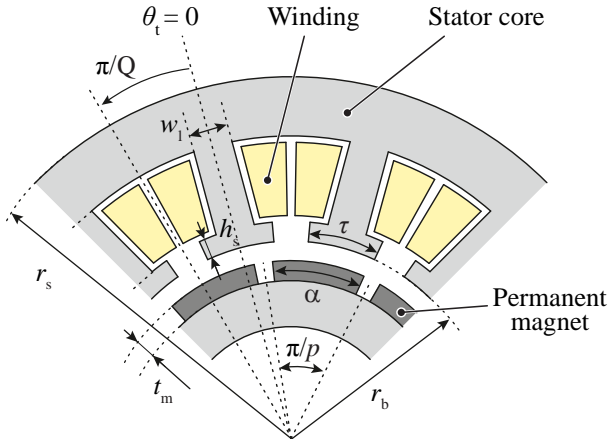


**Figure 7.3:** Cross-sectional view and the geometric parameters of the slotted machine.

tooth is aligned with a permanent magnet. This means that the no-load flux is just enough to saturate the tooth. It has to be noted that the effect of the armature reaction is neglected, resulting in an optimistic machine model in terms of torque capability.

The tooth tip height  $h_s$  is calculated similarly, such that the tooth tip operates at saturation at no-load

$$h_s = \frac{r_b}{B_{\text{sat}}} \int_{w_l/2r_b}^{\pi/Q} B_{\text{ra}}(\theta_t) d\theta_t. \quad (7.2)$$

Only double-layer windings are considered for minimizing the axial space required by the end windings. Rotor magnets are assumed to be sintered NdFeB permanent magnets with remanent flux density of 1.1 T and amorphous iron (Table 3.1) is considered as stator core material, similar to the slotless machine.

The flux linkage of one phase is calculated for each rotor position by integrating the radial component of the no-load air gap flux seen by the coils belonging to that phase as

$$\psi_{\text{phaseA}}(\theta) = l_a r_b \sum_{\text{phaseA}} \int_{w_1/2r_b}^{\pi/Q} B_{\text{ra}}(\theta_t) d\theta_t, \quad (7.3)$$

where  $\theta$  is the rotor position. The back EMF is obtained as the time derivative of the flux linkage. The stator phase currents are calculated such that the resulting copper losses are 6 W, assuming a copper filling factor of 0.3. Finally, the torque is calculated from the power balance as

$$T = 3 \frac{E_{\text{b,rms}} I_{\text{rms}}}{\omega_m}, \quad (7.4)$$

where  $E_{\text{b,rms}}$  and  $I_{\text{rms}}$  are the root-mean-square values of the back EMF and the phase current, and  $\omega_m$  is the the mechanical rotational speed of the rotor.

The stator core losses are calculated based on Steinmetz's equation, assuming that the peak flux is equal to the core material's saturation flux density everywhere in the stator core. Air-friction losses are calculated according to [19], assuming a cylindrical rotor resulting from a 0.2 mm sleeve covering the permanent magnets.

The analytical model described above is verified using linear<sup>3</sup> 2-D FEM analysis. Figure 7.4 shows the results of the radial component of flux density in the middle of the air gap for one pole as calculated by analytical and FEM models. Figure 7.5 shows the back EMF of the same machine for one winding turn at 200 000 r/min as calculated by analytical and FEM models. It can be concluded that both models yield very similar results, which verifies the use of computationally more efficient analytical models for the optimization of the slotted machine.

Figure 7.6 shows the no-load flux distribution in the same machine. It can be seen that the tooth width and the tooth tip height are calculated properly as the maximum flux density in the stator is equal to the saturation flux density of the core material<sup>4</sup>.

<sup>3</sup>The term linear FEM means that a constant permeability is assumed for all the materials in the FEM model.

<sup>4</sup>As shown in Table 3.1, the saturation flux density of the stator core material is 1.56 T. However, this is true for the iron only. Considering a stacking factor of 84%, iron is present only in the 84% of the active length whereas field sources such as windings and permanent magnets cover 100% of the active length. Therefore, the stator is modeled as a single solid with an active length identical to that of the permanent magnets and the windings, and an effective saturation flux density

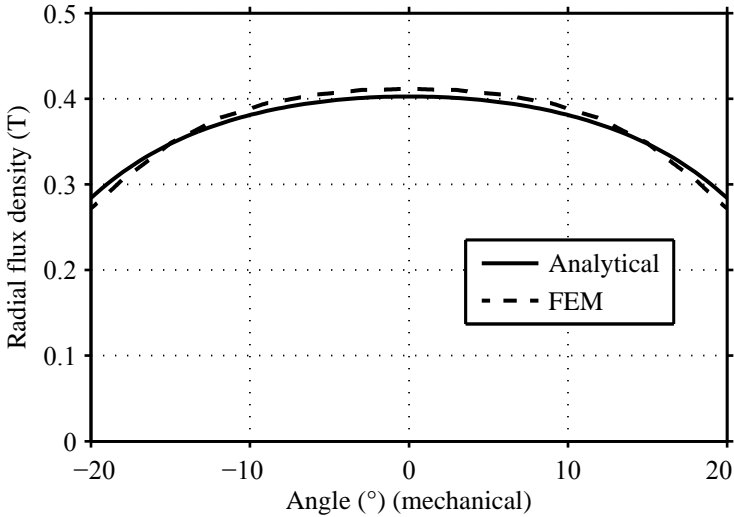


**Figure 7.4:** The radial component of the no-load flux in the air gap of a 3-pole, 9-slot machine with  $r_b = 2.7$  mm,  $t_m = 0.5$  mm,  $\alpha = 81^\circ$ ,  $\tau = 72^\circ$ . The windings of the machine are double-layer concentrated windings.

$r_s$	Stator outer radius	4 mm
$r_b$	Stator bore radius	1 to 3.5 mm
$t_m$	Magnet thickness	0.5 to 3.5 mm
$\frac{\tau Q}{2\pi}$	Tooth tip coverage	0.6 to 0.85
$\frac{\alpha p}{\pi}$	Pole coverage	0.6 to 1
$p/Q$	Pole-pair/slot number	2/6, 3/9, 4/12, 5/15, 6/18
$l_a$	Active length	7.4 mm

**Table 7.2:** Range of parameters defining the analyzed slotted machines.

After the verification using a 2-D linear FEM model, the analytical model is used to evaluate several machines that would fit in the same space as the slotless machine described in Section 7.1 and the LSM described in Section 3.2. The range of evaluated parameters is

$$B_{\text{sat}} = 1.56 \text{ T} \cdot 0.84 = 1.3 \text{ T}.$$

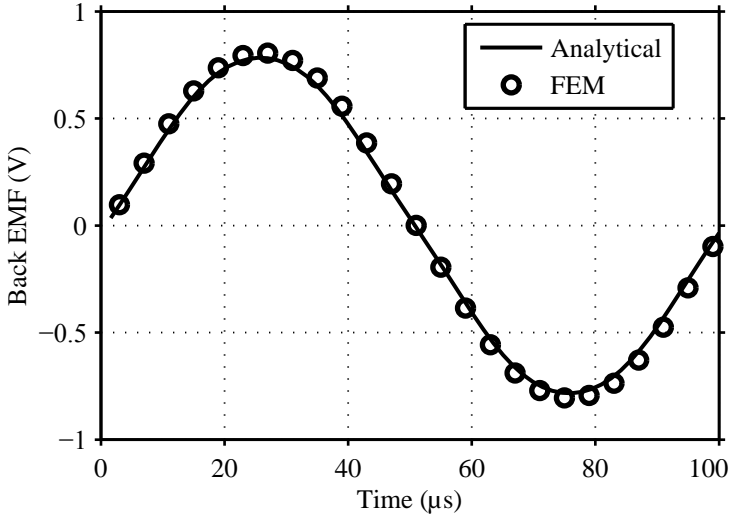


**Figure 7.5:** The back EMF of a 3-pole, 9-slot machine with  $r_b = 2.7$  mm,  $t_m = 0.5$  mm,  $\frac{\alpha p}{\pi} = 0.9$ ,  $\frac{\tau Q}{2\pi} = 0.8$ ,  $w_1 = 0.42$  mm and  $h_s = 0.17$  mm. The windings of the machine are double-layer concentrated windings. The speed of the machine is 200 000 r/min and the number of winding turns is one.

listed in Table 7.2. Figure 7.7 shows the mean torque at 6 W of copper losses and the no-load losses (stator core losses and air-friction losses) at 200 000 r/min for all the analyzed machines. It can be seen that the maximum torque that can be generated in the analyzed space is 1.7 mNm. Table 7.3 summarizes the key parameters of the machine that generates this torque.

### 7.3 Comparison

Previous sections of this chapter dealt with the analysis of both slotless and slotted radial flux machines that would fit in the same machining tool as the lateral-stator machine described in Section 3.2. Figure 7.8 shows the results of this analysis where the performance of these two state-of-the-art machine topologies and the LSM is shown. It can be seen clearly that for the same radial space in the tool head and the same

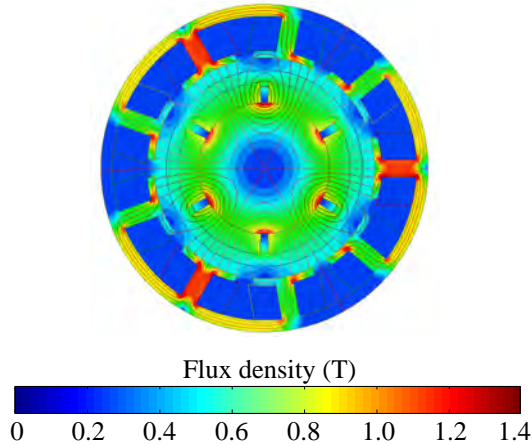


**Figure 7.6:** Linear 2-D FEM simulation results showing the no-load flux distribution of a 3-pole, 9-slot machine with  $r_b = 2.7$  mm,  $t_m = 0.5$  mm,  $\frac{\alpha p}{\pi} = 0.9$ ,  $\frac{\tau Q}{2\pi} = 0.8$ ,  $w_l = 0.42$  mm and  $h_s = 0.17$  mm. It can be seen that the maximum flux density in the stator is 1.3 T.

machine active length, the lateral-stator topology enables significantly higher torque output for the same copper losses.

Even though the same space limits are considered, this comparison is still not fair, as the same active length is assumed for all three types of machines. However, due to the straight and distributed windings with  $180^\circ$  pitch, the slotless machine requires considerably larger space for the end windings compared to the LSM, meaning that a shorter active length needs to be considered for the slotless machine if both machines must fit in the same space. Rhombic or skewed slotless windings may be used to shorten or fully avoid the end windings [62]; however, this reduces the winding factor and the torque-per-current rating of the machine.

The torque output of the slotted machine is also considerably smaller compared to that of an LSM for the same tool head. As only double-layer concentrated windings are considered in the slotted case, the space needed for the end windings is minimized. However, the end windings still need to be placed in the tool head, which is not the case for the LSM, as shown in Figure 7.9. Therefore, even if the axial length of the

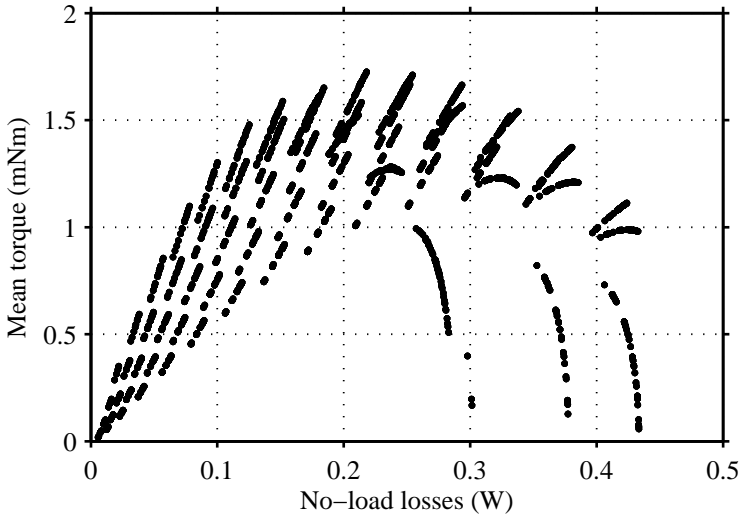


**Figure 7.7:** Performance of the slotted machines. y-axis shows the mean torque of the machine when producing 6 W copper losses. x-axis shows the no-load losses at 200 000 r/min.

end windings are the same for a cylindrical and a lateral-stator machine, the LSM can still have a longer rotor as the end windings are not in the tool head.

Finally, the analysis presented in this chapter assumes the same copper losses (6 W) for all the three machines that are compared. As the cylindrical machines that fit in the tool head have much smaller surface for cooling, the comparison of torque capability is expected to change even more in favor of the lateral-stator topology following a thermal analysis of the cylindrical machines<sup>5</sup>. If Figure 7.8 is interpreted considering the remarks about the end windings and the thermal aspects, it can be concluded that the LSM produces *at least* three times the torque that the state-of-the-art machines produce for given tool size.

It has to be noted that so far only applications with a limited space around the rotor have been considered where the stator of the LSM can grow in one lateral direction. Clearly, this gives an advantage to the

<sup>5</sup>A thermal model of an LSM in a dental handpiece is shown in the following section.

$T_1$	Mean torque at 6 W copper losses	1.72 mN m
$P_{\text{fe}}$	Stator core losses at 200 000 r/min	128 mW
$P_{\text{air}}$	Air-friction losses at 200 000 r/min	90 mW
$r_s$	Stator outer radius	4 mm
$r_b$	Stator bore radius	2.6 mm
$t_m$	Magnet thickness	0.7 mm
$\frac{\tau Q}{2\pi}$	Tooth tip coverage	0.6
$\frac{\alpha p}{\pi}$	Pole coverage	1
$p/Q$	Pole-pair/slot number	3/9
$w_1$	Tooth width	0.4 mm
$l_a$	Active length	7.4 mm

**Table 7.3:** Key parameters of the slotless machine that generates the highest torque.

LSM when comparing the maximum torque that can be generated, as the LSM does not need to fit in the same confined space; therefore, it can utilize more active material (permanent magnets, copper and iron). To be fair, it has to be mentioned that it is the *local* torque density that increases when using an LSM. When comparing the overall torque densities, state-of-the-art round-shaped electrical machines are likely to perform better due to the inherent disadvantages of the LSM topology such as the stray field between the stator legs and the shielding iron that does not contribute to torque production.

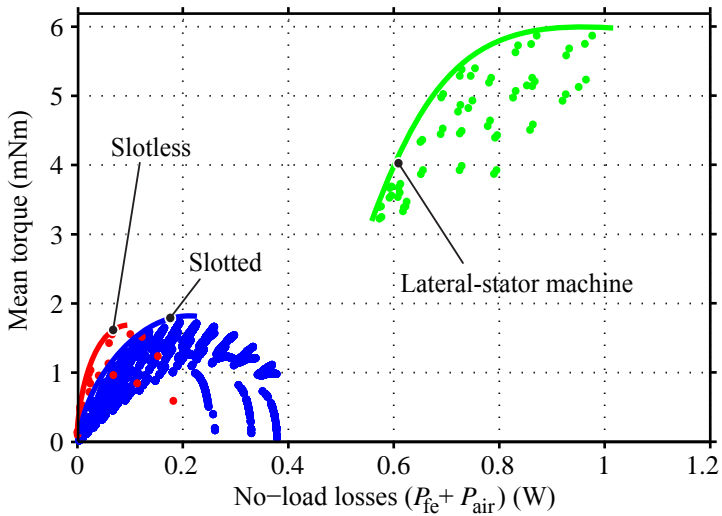


**Figure 7.8:** Comparative evaluation of the performances of two state-of-the-art machines and the lateral-stator machine. y-axis shows the mean torque of the machines when producing 6 W copper losses. x-axis shows the no-load (stator core and air friction) losses at 200 000 r/min.

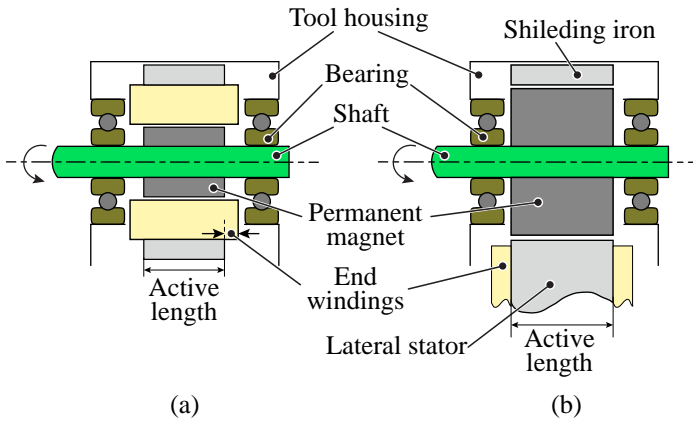


**Figure 7.9:** Positioning of two different machines in the same machining tool. (a) Standard cylindrical machine with end windings, (b) section-type lateral-stator machine. The end windings of the standard machine and the bearings need to fit in the same space, limiting the maximum machine active length. As the windings are taken out of the tool head, the LSM can have a larger active length compared to the standard machine.



## Chapter 8

# Improved machine design and integration in a medical application

In the previous chapters of this thesis, the LSM concept is introduced for directly driven machining applications where the space at the tool head is limited. Two different types of this new machine topology are comparatively analyzed by simplifying the whole operation range to the consideration of only two operating points: the zero-speed, high-torque operating point and the high-speed, no-load operating point. The design goal is to maximize the torque at the zero-speed operating point for given copper losses while generating less losses than a given limit at the high-speed, no-load operating point. Following this analysis, an initial prototype is built where the loss limits originate from very simple thermal considerations. The design procedure is experimentally verified using the initial prototype.

This section deals with the integration of an improved LSM in a medical application, following the same design procedure. However, a more detailed thermal model of the example application (a dental handpiece) is built and used to set the loss limits at the aforementioned operating points. In order to do so, a lumped-parameter-based thermal model is constructed for a given dental handpiece and a given LSM geometry. The overall cooling capability depends strongly on the coolant (air and water, as described in the following section) flow rates, the

	Amorphous	Cobalt-iron
Density ( $\text{g}/\text{cm}^3$ )	7.18	8.12
Young's modulus (GPa)	100	200
Saturation flux density (T)	1.56	2.3
Stacking factor	84%	>95%
Electrical resistivity ( $\mu\Omega \text{ m}$ )	1.3	0.44
Core losses at 400 Hz, 0.5 T (W/kg)	0.5	2.5
Core losses at 400 Hz, 1 T (W/kg)	1.8	12
Core losses at 1 kHz, 0.5 T (W/kg)	2	15
Core losses at 1 kHz, 1 T (W/kg)	5	55

**Table 8.1:** Comparison of commercially available 23  $\mu\text{m}$  amorphous iron [25] and 0.35 mm cobalt-iron sheets [34].

shape and the structure of the handpiece, and the positioning of the LSM in the handpiece. Therefore at the first step, the electromagnetic loss limits considered in this chapter originate from a thermal model that assumes a constant LSM geometry that is based on the analysis of the first prototype.

So far in this thesis only amorphous iron is considered as stator core material due its lower losses compared to standard electrical steel and its relatively high saturation flux density compared to nanocrystalline alloys and ferrites. As the saturation of the core is one of the main limiting factors for torque generation, a stator core material with higher saturation flux density will lead to a higher torque capability, which is the main motivation behind the lateral-stator concept. For this reason, in this section cobalt-iron is also considered as stator core material along with amorphous iron, as the saturation flux density of cobalt-iron is 2.3 T, significantly higher compared to the 1.56 T of the amorphous iron. Furthermore, the stacking factor of cobalt-iron laminations is above 95% whereas for the amorphous iron this value is around 84%. Accordingly, the difference between the effective saturation flux densities of amorphous and cobalt-iron cores is even larger. Table 8.1 compares further properties of both materials.

At the time of writing this thesis, cobalt-iron laminations with individual sheets as thick as 0.1 mm or even 0.05 mm are available, and they have significantly lower core losses than the standard 0.35 mm sheets. On the other hand, the precise production of small parts with

$d_p$	Water pipe diameter	1 mm
$w_p$	Water pipe wall thickness	0.2 mm
$d_t$	Air tube diameter	1 mm
$r_c$	Handpiece case radius	8 mm
$w_c$	Handpiece case wall radius	1 mm
$w_w$	Winding thickness	1.2 mm
$l_a$	Active length	8 mm
$l_w$	Winding length	10 mm
$a_{sc}$	Stator core cross-sectional area	60 mm <sup>2</sup>
$a_{in}$	Insulation tape thickness	0.2 mm
$r_r$	Rotor (magnet outer) radius	3.6 mm
$r_o$	Stator bore radius	3.8 mm
$w_r$	Shaft radius	1.5 mm

**Table 8.2:** Dimensions of the thermal model.

features smaller than 1 mm using thin laminations is still a challenging task where a few iterations may be needed before the machining process is fully optimized. However, the author believes that in the near future with some effort spent on manufacturing, the use of cobalt-iron in small sized LSMs will be feasible and increase the torque capability of the LSMs even further. Therefore, the analysis considering cobalt-iron is valuable as it shows the near-future capability of this machine type.

## 8.1 Thermal analysis of a dental handpiece

Figure 8.1 shows two cross-sectional views of the stator of an LSM placed in the neck of a dental handpiece. The housing of the handpiece is assumed to have a cylindrical form and it is filled with epoxy to facilitate the cooling of the stator. An air tube, which is directly connected to the housing, carries pressurized air that first goes through the neck of the handpiece and later through the air gap before being sprayed into the patient's mouth. This means that the air helps cooling both the stator and the rotor of the handpiece. Similarly, a water pipe going through the neck carries water that helps cooling the stator before being sprayed in the patient's mouth. The water does not go through the air gap, hence it does not contribute to rotor cooling. Table 8.2 gives the dimensions and Table 8.3 lists the properties of the materials used.

	Specific heat $c$ , J/(kg K)	Density $\rho$ , kg/m <sup>3</sup>	Thermal conductivity $\lambda$ , W/(m K)
Aluminium	900	2700	235
Copper	385	8930	350
Epoxy	1060	1200	0.5
Magnetic iron	430	8120	40
Permanent magnet	350	7700	230
Insulation tape	-	-	0.2

**Table 8.3:** Physical properties of the materials used in the thermal model.

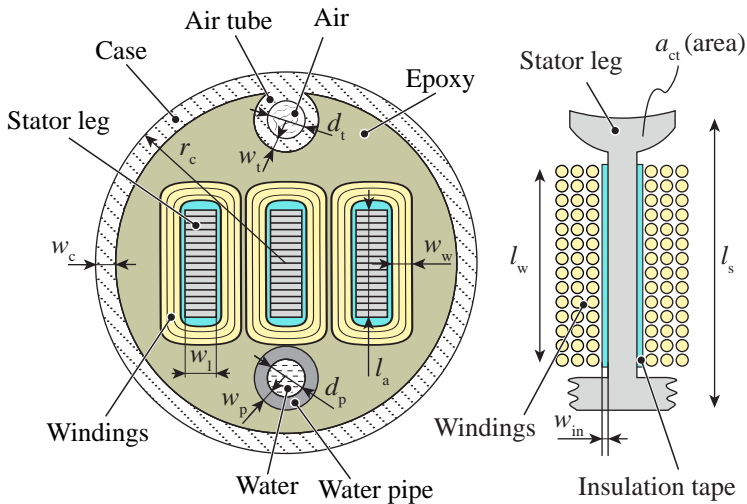


**Figure 8.1:** Cross-sectional view of the dental handpiece and the middle leg of the LSM with the windings.

Thermal behavior of the stator in the handpiece is analyzed using a lumped-parameter thermal equivalent circuit that is depicted in Figure 8.2. Table 8.4 lists the physical meanings of the elements of the thermal equivalent circuit.

The calculation of the thermal capacitances is straightforward as

Power sinks/sources	
$P_{fe}$	Core losses (shielding iron is neglected)
$P_{cu}$	Copper losses
$P_{air}$	Air-friction losses
$P_{air,s}$	Heat removed from the stator by air
$P_{air,r}$	Heat removed from the rotor by air
$P_{eddy}$	Eddy-current losses
$P_{wa}$	Heat removed from the stator by water
Thermal resistances	
$R_{fe-w}$	Between stator core and windings
$R_{w-ep}$	Between windings and epoxy
$R_{ep}$	Between epoxy and handpiece housing
$R_{c-amb}$	Between housing and ambient
$R_{t-air}$	Between tube and air in the tube
$R_{w-p}$	Between windings and water pipe
$R_{p-wa}$	Between pipe and water inside
Thermal capacitances	
$C_{fe}$	Stator core (shielding iron is neglected)
$C_w$	Windings (all three coils)
$C_{ep}$	Epoxy that fills the voids in the handpiece
$C_c$	Handpiece housing
$C_{air}$	Air in the tube
$C_p$	Water pipe
$C_r$	Rotor
$C_{wa}$	Water in the pipe
$T_{amb}$	Ambient (room) temperature

**Table 8.4:** Physical meanings of the elements of the thermal equivalent circuit.

the specific heat values for the used materials are well known and their masses can be easily calculated based on their geometries. For example, the thermal capacitance of the stator core can be approximated as

$$C_{sc} = a_{sc} l_a k_s \rho_{fe} c_{fe} \quad (8.1)$$

where  $a_{ct}$  is the cross-sectional area of the stator core,  $l_a$  is the active length,  $k_s$  is the stacking factor,  $\rho_{fe}$  and  $c_{fe}$  are the density and the specific heat of the core material.

Similarly, the thermal capacitance of the windings can be calculated as

$$C_w = m_w c_w \quad (8.2)$$

where  $m_w$  is the mass of the windings and is given by

$$m_w = 6(l_a + w_w + w_l)w_w l_w \rho_w \quad (8.3)$$

and

$$\rho_w = k_f \rho_{cu} + (1 - k_f) \rho_{ep} \quad (8.4)$$

where  $k_f$  is the filling factor and  $\rho_{cu}$  and  $\rho_{ep}$  represent the densities of copper and epoxy. The equivalent specific heat of the winding pack is calculated as

$$c_w = k_f c_{cu} \frac{\rho_{cu}}{\rho_w} + (1 - k_f) c_{ep} \frac{\rho_{ep}}{\rho_w}, \quad (8.5)$$

where  $c_{cu}$  and  $c_{ep}$  are the specific heats of copper and epoxy, respectively.

The geometry of epoxy filling the voids between the LSM and the handpiece is approximated by a hollow cylinder and its thermal capacitance is calculated as

$$C_{ep} = l_w \pi ((r_c - w_c)^2 - (w_w + l_a/2)^2) \rho_{ep} c_{ep} \quad (8.6)$$

As they all have hollow cylindrical shapes, the thermal capacitances of the air tube, the water pipe and the handpiece casing are calculated in a very similar fashion to the thermal capacitance of the epoxy filling.

The thermal capacitances of the air in the tube and the water in the pipe are calculated as

$$C_{fl} = V_{fl} \rho_{fl} c_{fl} \quad (8.7)$$

where  $V_{fl}$ ,  $\rho_{fl}$  and  $c_{fl}$  represent the volume, density and the specific heat of the fluid (air or water) in the channels (air tube or water pipe).

The copper losses are assumed to be concentrated only in the middle of the winding width  $w_w$ . When the thermal resistance along copper direction is neglected, the thermal resistance between the stator core and the windings can be approximated as

$$R_{sc-w} = \frac{1}{3} \left( R_{in} + \frac{0.5 w_w}{2(l_a + w_l) l_w \lambda_w} \right) \quad (8.8)$$

where  $\lambda_w$  denotes the thermal conductivity of the winding region in the direction perpendicular to the copper winding direction and it can be calculated as

$$\lambda_w = \left( \frac{k_f}{\lambda_{cu}} + \frac{1 - k_f}{\lambda_{ep}} \right)^{-1}. \quad (8.9)$$

The thermal resistance of the insulation tape is

$$R_{in} = \frac{w_{in}}{2(l_a + w_l)\lambda_w\lambda_{in}} \quad (8.10)$$

where  $\lambda_{in}$  is the thermal conductivity of the insulation tape.

The thermal resistance between the windings and the epoxy is calculated similarly

$$R_{w-ep} = \frac{0.5w_w}{S_{w-ep}\lambda_w} \quad (8.11)$$

where  $S_{w-ep}$  is the contact surface area between the windings and the epoxy, which can be calculated as

$$S_{w-ep} = 2l_w((3w_s + 6w_w) + (l_a + 2w_w)). \quad (8.12)$$

As its shape is approximated by a hollow cylinder, the thermal resistance of the epoxy filling can be obtained as [63]

$$R_{ep} = \frac{\ln\left(\frac{r_c - d_c}{w_w + l_a/2}\right)}{2\pi l_w \lambda_{ep}}. \quad (8.13)$$

The natural convection from the handpiece housing to ambient (represented by the thermal resistance  $R_{c-amb}$ ) is calculated according to [64], assuming a cylindrical housing.

The heat transfer coefficient  $h$  from a circular channel to the fluid flowing in it can be calculated as

$$h = \frac{Nu\lambda_{fl}}{d_h} \quad (8.14)$$

where  $Nu$  is the Nusselt number,  $\lambda_{fl}$  is the thermal conductivity of the fluid and  $d_h$  is the hydraulic diameter, which is equal to the channel diameter for circular channels. The Nusselt number is calculated using empirical equations depending on the flow properties, as described in

	Air	Water
Specific heat, $c$ (J/(kg K))	1005	4184
Density, $\rho$ (kg/m <sup>3</sup> )	1.18	997
Thermal conductivity, $\lambda$ (W/(m K))	0.026	0.597
Volumetric flow rate, $\dot{V}$ (l/min)	10	0.12
Nusselt number (in the tube and pipe), $Nu$	3.66	21.56

**Table 8.5:** Physical properties and flow rates of the fluid used as coolants.

detail in [65]. Finally, the thermal resistance between the pipe and the fluid can be calculated as

$$R_{\text{fl}} = \frac{1}{hS_{\text{wet}}} \quad (8.15)$$

where  $S_{\text{wet}}$  is the wetted surface area inside the pipe. The flow rate and further relevant physical properties of the coolant fluids are given in Table 8.5.

The heat that is removed from the stator by the air is calculated as

$$P_{\text{air,s}} = \rho_{\text{air}} \dot{V}_{\text{air}} c_{\text{air}} (\delta_{\text{o}} - \delta_{\text{i}}) \quad (8.16)$$

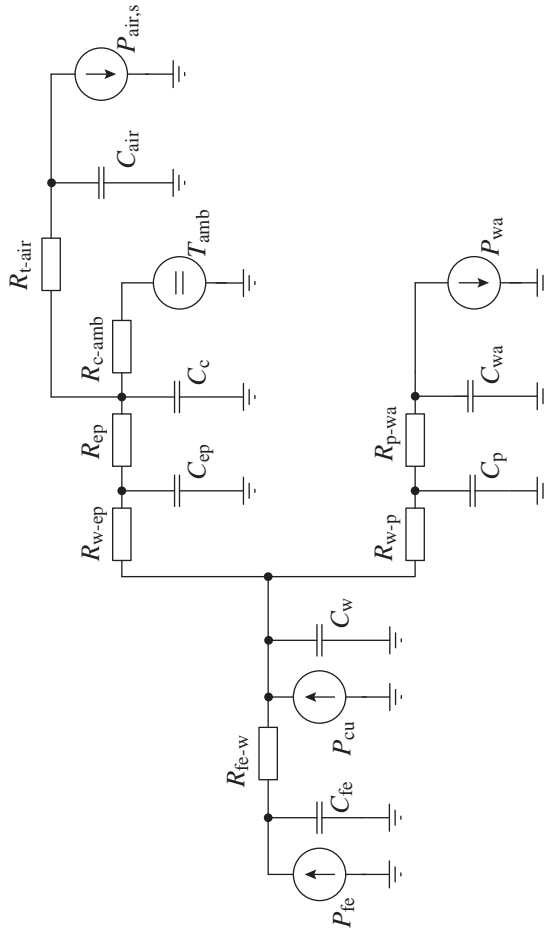
where  $\rho_{\text{Air}}$  is the density,  $\dot{V}_{\text{Air}}$  is the volumetric flow rate and  $c_{\text{Air}}$  is the specific heat of air.  $\delta_{\text{i}}$  and  $\delta_{\text{o}}$  denote the temperature of air that enters and exits the tube, respectively. The heat removed by water is calculated in a similar fashion.

Figure 8.3 shows the assumed rotor geometry for the thermal analysis of the rotor and the air gap. Figure 8.4 shows the thermal equivalent circuit. The rotor is modeled with an isothermal cylindrical body whose thermal capacitance is calculated as

$$C_{\text{r}} = \pi w_{\text{s}}^2 l_{\text{a}} \rho_{\text{fe}} c_{\text{fe}} + \pi (r_{\text{r}} - w_{\text{s}})^2 l_{\text{a}} \rho_{\text{pm}} c_{\text{pm}}, \quad (8.17)$$

where  $\rho_{\text{pm}}$  is the density and  $c_{\text{pm}}$  is the specific heat of the permanent magnet.

In order to calculate the thermal resistance from the rotor to the air gap at different operating conditions of the handpiece, the heat transfer coefficient from the rotor to the air gap is calculated for three different cases:



**Figure 8.2:** Lumped parameter thermal equivalent circuit describing the thermal behavior of the lateral-stator in the handpiece.

- ▶ rotor at standstill, no axial air flow (handpiece turned off);
- ▶ rotor at standstill, axial air flow present (low-speed, high-torque operating point of the handpiece);

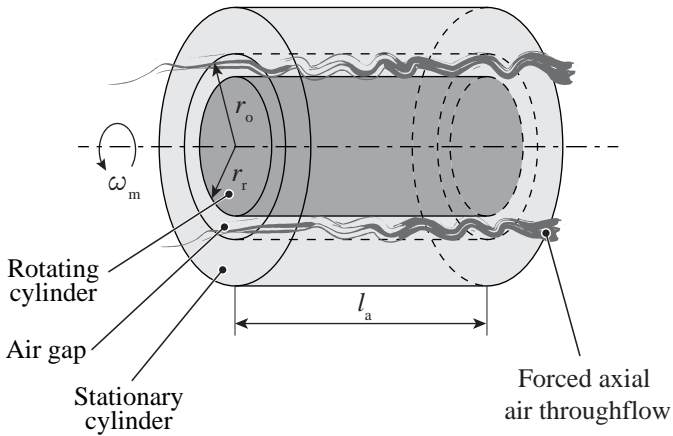


**Figure 8.3:** Cooling of the rotor with forced axial air throughflow.

- rotor rotating at 200 000 r/min, axial air flow present (high-speed, no-load operating point of the handpiece).

The heat transfer through the bearings is neglected at the first step for all the cases. For the first case, natural convection is the only heat transfer mechanism, whose heat transfer coefficient is calculated according to [64].

For the second case, the Nusselt number is taken from [65]. The heat transfer coefficient is calculated according to (8.14), where the hydraulic diameter  $d_h$  is written as  $d_h = 2(r_b - r_r)$ , and  $r_r$  and  $r_b$  are the rotor and stator bore radii.

Finally, for the third case, the empirical equation for calculating the Nusselt number is taken from [66], which presents empirical correlations for the heat transfer in coaxial cylinders where there is axial air flow in the annulus and the inner cylinder is rotating.

The thermal model described above can be used to estimate the temperature in various parts of the LSM and the handpiece as well as the coolant temperatures exiting the handpiece. Hence, they can be used to set the maximum allowed losses under different operating conditions based on either ergonomic constraints or safe operation limits of the machine components. Table 8.6 summarizes those limits.

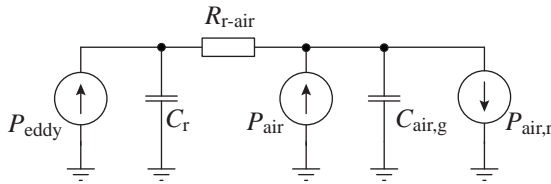


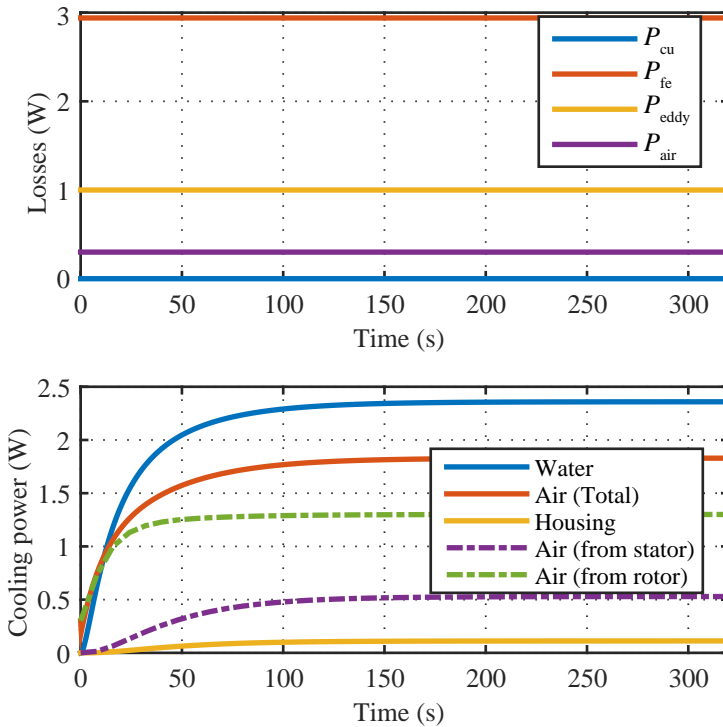
**Figure 8.4:** Thermal equivalent circuit of the rotor.

Ergonomic constraints	
Maximum air spray temperature	37 °C
Maximum water spray temperature	37 °C
Maximum handpiece housing temperature	41 °C
Device safe operation limits	
Maximum winding temperature (insulation limit)	100 °C
Maximum rotor temperature (demagnetization limit)	120 °C

**Table 8.6:** Temperature limits in the handpiece.

For example, Figure 8.5 shows the heat generated by different no-load loss components during continuous operation at 200 000 r/min along with the heat removed by different cooling mechanisms when the volumetric flow rate is 120 ml/min for water and 10 l/min for air. Figure 8.6 shows the temperatures in different parts of the machine as well as the coolant temperatures for the same condition. Figure 8.7 shows the values of key thermal resistances.

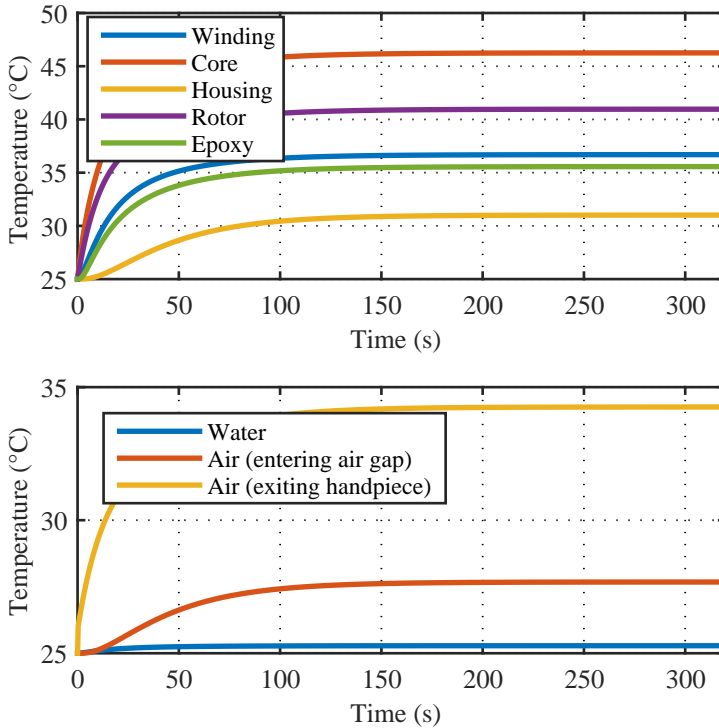
As clearly seen in these figures, water removes the most amount of heat whereas the cooling through natural convection on the handpiece housing is comparably weak. None of the machine parts heats up to temperatures above 50 °C, therefore the safe operation of the device is not endangered. The warmest component is the stator core whose temperature goes up to 46 °C when the initial temperature is assumed to be 25 °C. The water temperature stays almost constant at no-load conditions, whereas the air temperature rises from 25 °C to around 28 °C after going through the neck and removing some heat from the stator. The air temperature rises further to 34 °C due to the rotor eddy-current and air-friction losses after flowing axially through the air gap. It can



**Figure 8.5:** (Top) Heat generated by different loss components at 200 000 r/min. (Bottom) The heat removed by different cooling mechanisms. The volumetric flow rate is 120 ml/min for water and 101/min for air.

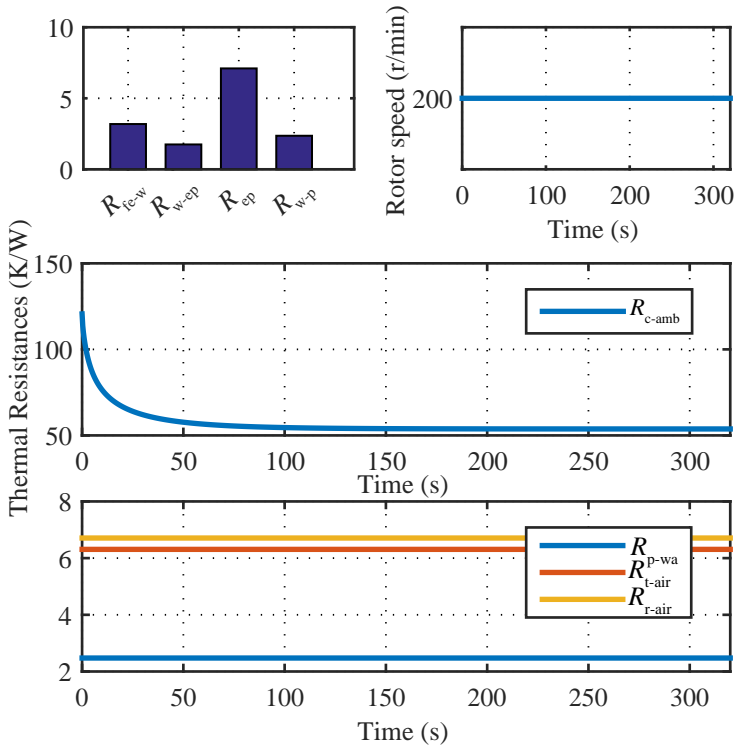
be seen that the assumed no-load loss components shown in Figure 8.5 do not violate the thermal limits given in Table 8.6. However, in order to set the final limits for the different loss components, also the intermittent high-torque operating point needs to be considered.

Figure 8.8 shows the heat generated by various loss components and removed by different cooling mechanisms when the machine alternates between the high-speed, no-load operating point and the intermittent zero-speed, high-torque operating point. The duty cycle of operation is assumed to be 2 min of high-speed low-load operation followed by a



**Figure 8.6:** Temperature rise in the machine and in the coolants while the machine runs continuously at 200 000 r/min at no-load. The volumetric flow rate is 120 ml/min for water and 101/min for air.

20s low-speed, high-load operation. As for the continuous operation, the flow rate of both coolants stay constant over the whole operation at 120 ml/min for water and 101/min for air. Figure 8.9 shows the temperature rise in the machine and in the coolants for this operation. The temperature of the air exiting the handpiece goes up to 36 °C, very close to the ergonomic limit of 37 °C at the end of 12s. On the other hand, the highest temperature in the machine is only 60 °C, well below the safe operating limits of the LSM. Figure 8.10 shows various thermal resistances in the LSM and the rotor speed during the intermittent operation.



**Figure 8.7:** Various thermal resistances and the rotor speed during the continuous operation. The volumetric flow rate is 120 ml/min for water and 10l/min for air.

## 8.2 Electromagnetic design of the machine

### 8.2.1 Modeling

The electromagnetic design of the second prototype is carried out in the same way as that of the first prototype. Due to its higher torque capability, only the section-type LSM topology is considered. Table 8.7 shows the loss limits considered for the design, which originate from the thermal analysis presented in the previous section.

The geometry is parametrized as shown in Figure 8.11. The discretization of the parameter range along with the geometric constraints

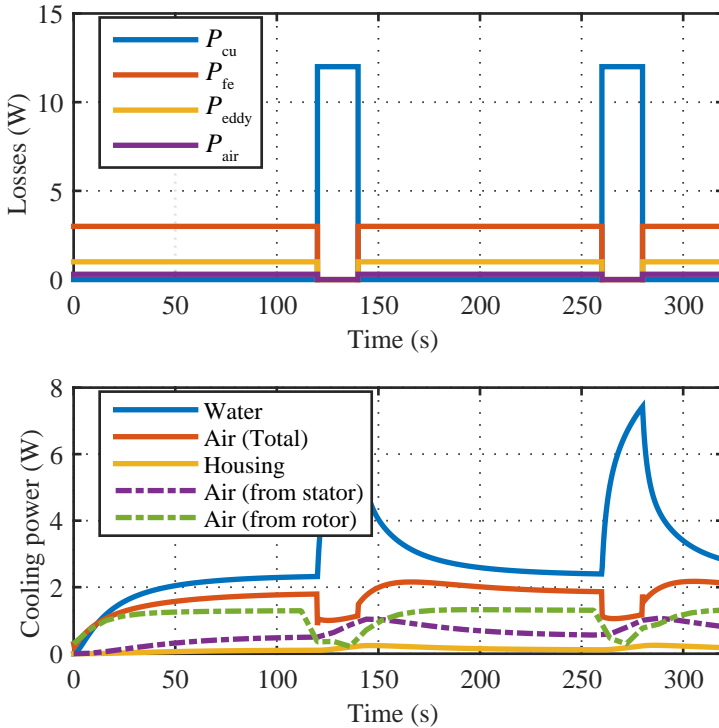


**Figure 8.8:** (Top) Heat generated by different loss components at 200 000 r/min. (Bottom) The heat removed by different cooling mechanisms. The machine is alternating between the high-speed, no-load operating point (2 min and the intermittent, zero-speed, high-torque operating point (20 s). The volumetric flow rate stays constant at 120 ml/min for water and 101/min for air.

are given in Table 8.8. Compared to the first prototype, the stator geometry is modified slightly for a better integration in the available space in a dental handpiece. For example, the overall machine width (sum of the width of three legs and six coil sides) is fixed to be equal to the neck width of the tool housing  $w_t$ . Similarly, the active length of the machine  $l_a$  is not a constant (as it is in the first prototype), but a function of the winding width  $w_w$  and the housing depth (axial space available for the machine)  $d_t$  as

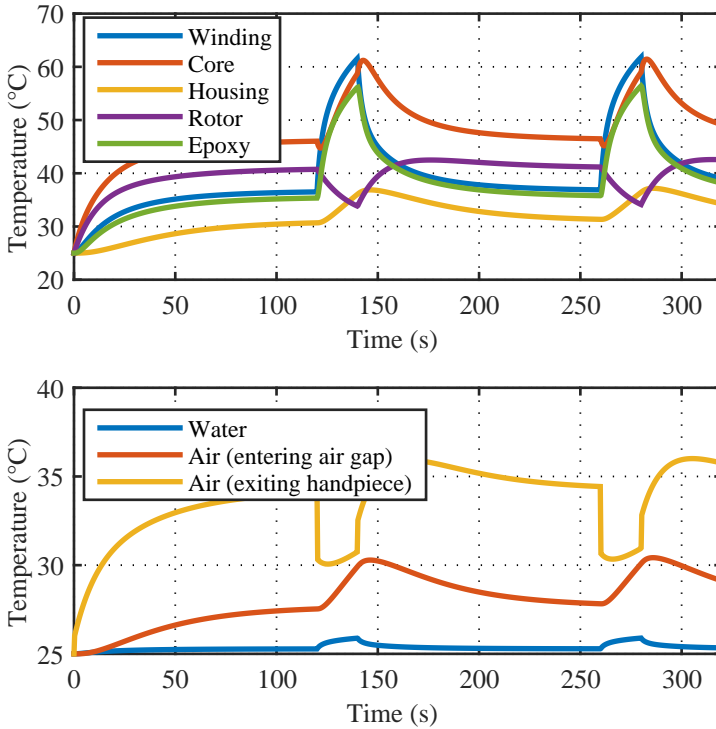


**Figure 8.9:** Temperature rise in the machine and in the coolants while the machine alternates between the high-speed, no-load operating point (2 min) and the intermittent, zero-speed, high-torque operating point (20 s). The volumetric flow rate stays constant at 120 ml/min for water and 101/min for air.

$$l_a = d_t - 2w_w, \quad (8.18)$$

where  $w_w$  is defined as

$$w_w = \frac{w_t - 3w_l}{6}. \quad (8.19)$$

Similar to the first prototype, a solid cobalt-iron shaft, NdFeB magnets with 1.1 T remanent flux density and a titanium sleeve is used.

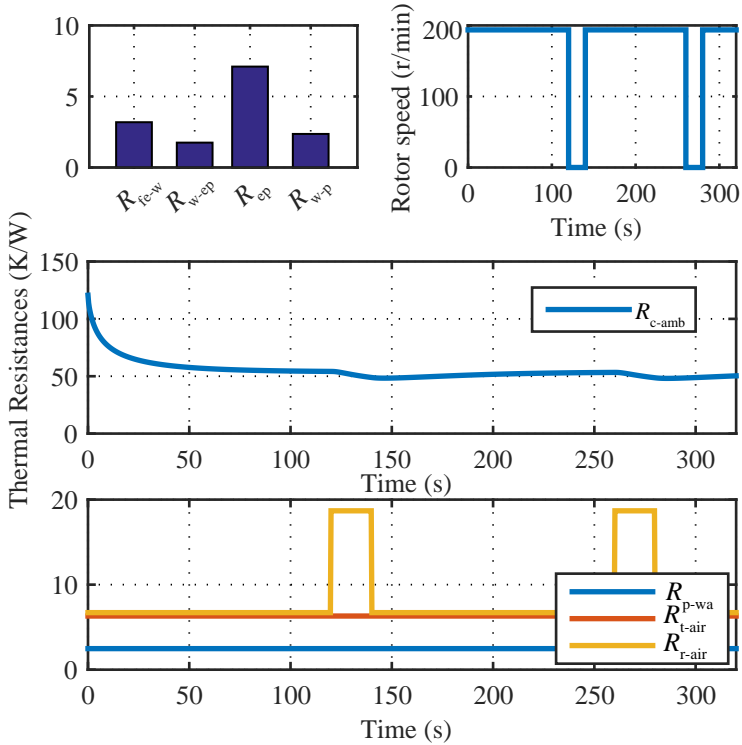


**Figure 8.10:** Various thermal resistances and the rotor speed during the intermittent operation. The volumetric flow rate is 120 ml/min for water and 101/min for air.

Table 3.6 shows the electrical conductivities and Table 3.8 mechanical properties of these materials.

## 8.2.2 Simulation results

As can be seen from the definition of the geometric parameters, the rotor outer radius is the same (3.3 mm) for all the analyzed machines. The maximum active length that any machine in the analyzed parameter space can have is 6.8 mm according to (8.18), (8.19) and Table 8.8. Consequently, the maximum air-friction losses can be calculated accord-

High-speed, no-load operating point	
$P_{\text{air}}$	0.3 W
$P_{\text{eddy}}$	1 W
$P_{\text{fe}}$	3 W
Zero-speed, high-torque operating point	
$P_{\text{cu}}$	12 W

**Table 8.7:** Loss limits considered for the electromagnetic design.

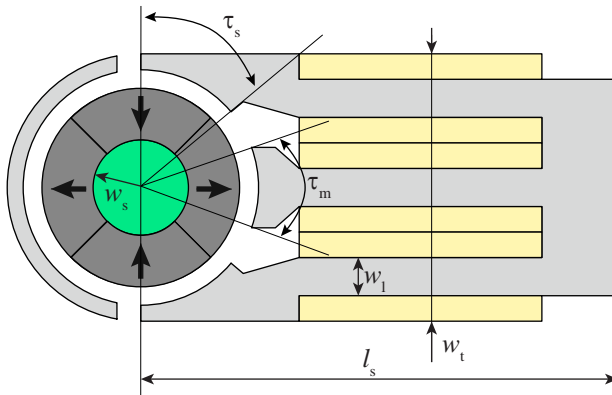


**Figure 8.11:** Cross-sectional view and the geometric parameters of the second prototype.

ing to [19] to be 0.24 W.

Figure 8.12 plots the mean torque for 12 W copper losses and core losses at no-load and 200 000 r/min for all the analyzed machines. As expected, cores made of cobalt-iron yield higher torque, but also higher core losses. Figure 8.13 shows the average torque and the torque ripple, which is defined as difference of the maximum and minimum values of the instantaneous torque over one period at full-load, for all the machines. The use of amorphous core material does not bring any advantages in terms of torque ripple either; therefore, from here on only the cobalt-iron is considered as core material. Figure 8.14 shows the mean torque and the rotor eddy-current losses for machines with

$w_s$	Shaft radius	0.2, 1, 1.5 and 2.5 mm
$l_s$	Stator length	15, 25, 35 and 45 mm
$\tau_s$	Shoe span (side)	25, 30, 40, 50 and 55°
$\tau_s$	Shoe span (middle)	25, 30, 40, 50 and 55°
$w_l$	Leg width	0.5, 0.8, 1, 1.2, 1.6, 1.8 and 2 mm
$w_t$	Tool neck width (fixed)	8.4 mm
$d_t$	Tool housing depth (into page plane)	8 mm

**Table 8.8:** Discretization of the parameter range including fixed parameters for the first prototype.

cobalt-iron core only. The highest torques are achievable with machines that generate less than 1 W of rotor eddy-current losses<sup>1</sup>.

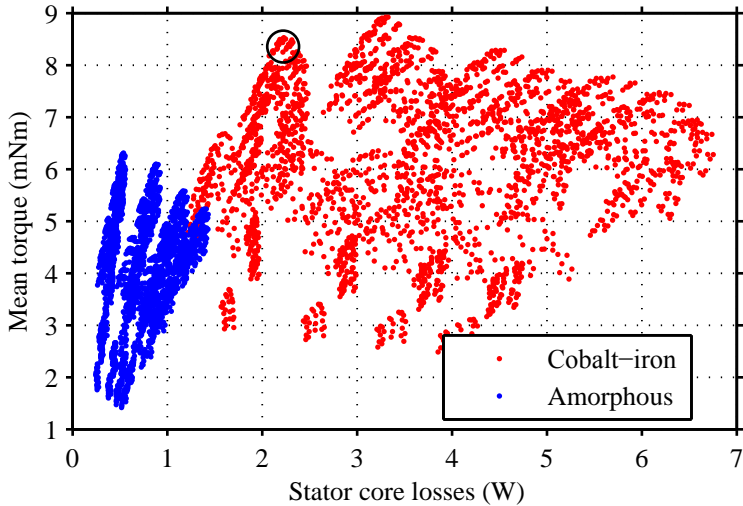
Figure 8.15 depicts the effect of the stator length, the leg width and the shaft radius on the machine performance. Even though the highest torques are achieved at 25 mm stator length, the larger stator volume leads to iron losses above the limit of 3 W. Increasing the stator length further keeps increasing the iron losses, but does not increase the torque due to the leakage flux between the stator legs.

Figure 8.16 shows the effect of the leg width the machine performance. A too narrow leg width limits the flux carrying capacity of the stator whereas a too wide leg width leaves little space for the windings and limits the current for a given amount of copper losses. In this case, 1.2 mm, which is in the middle of the analyzed region, is the optimum value for stator leg thickness.

As it can be seen in Figure 8.17, the shaft radius does not play a very important role in the electromagnetic behavior of the machine as long as it is not too large, which leads to too thin permanent magnets as the rotor outer radius is fixed. However, the shaft radius may play a significant role in terms of mechanical stability of the rotor, therefore is has to be selected following a mechanical analysis of the rotor, as discussed in the design of the first prototype.

Of the optimum machines marked with a circle in Figure 8.12, the one with the smallest torque ripple is selected as the best machine in the design space. The mean torque of this machine is 8.6 mm at 12 W

<sup>1</sup> The eddy-current losses are calculated in a 2-D model which is known to over-estimate the losses due to the lack of end resistances.



**Figure 8.12:** Mean torque at 12 W copper losses and core losses at no-load and 200 000 r/min for all the analyzed machines. Blue denotes machines with stators made of amorphous iron, red denotes machines with stators made of cobalt-iron. The circle marks the optimum group of machines, i.e. machines that generate the highest torque while generating less iron losses than the limit of 3 W.

Rotor eddy-current losses	0.66 W
Stator core losses	2.43 W
Air-friction losses	0.22 W

**Table 8.9:** Calculated no-load loss components of the selected machine at 200 000 r/min.

of copper losses. Figure 8.18 shows the dimensions of this machine. Table 8.9 lists the different components of the no-load losses generated in this machine at 200 000 r/min.

Figure 8.19 shows the torque generated by this machine for different loads (different stator currents, leading to different copper losses). The design point corresponding to 12 W copper losses is marked with a circle. This operating point corresponding to the knee region of the saturating

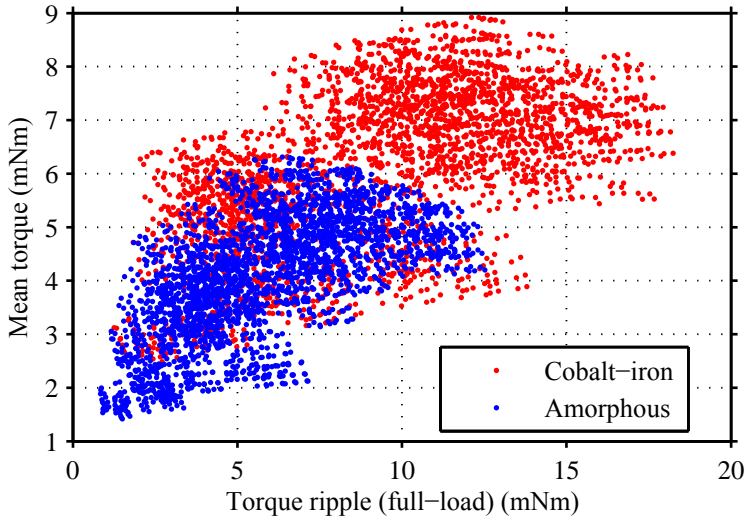


**Figure 8.13:** Torque ripple at 12 W copper losses and core losses at no-load and 200 000 r/min for all the analyzed machines. Blue denotes machines with stators made of amorphous iron, red denotes machines with stators made of cobalt-iron.

curve shows a good utilization of the machine. This is an interesting outcome showing that the simulation approach followed in this work by fixing the outer dimensions, limiting the iron losses and maximizing the torque for a given copper losses actually led to an optimum utilization of the core of the machine, even though it was not directly forced by the optimization routine.

In Chapter 3, the proof-of-concept is presented for the LSM and it is followed by the optimization and hardware realization of the LSM first prototype. This chapter presents a slightly different arrangement of the machine geometry, ensuring a better utilization of the available space in the tool. Furthermore, a more detailed thermal analysis is presented. As a result, a mean torque of 8.6 mN m is achieved considering NdFeB magnets with 1.1 T remanent flux density, cobalt-iron core material with 0.1 mm lamination thickness and a machine geometry that fits in a dental handpiece with a neck width of 8.4 mm and a depth of 8 mm.

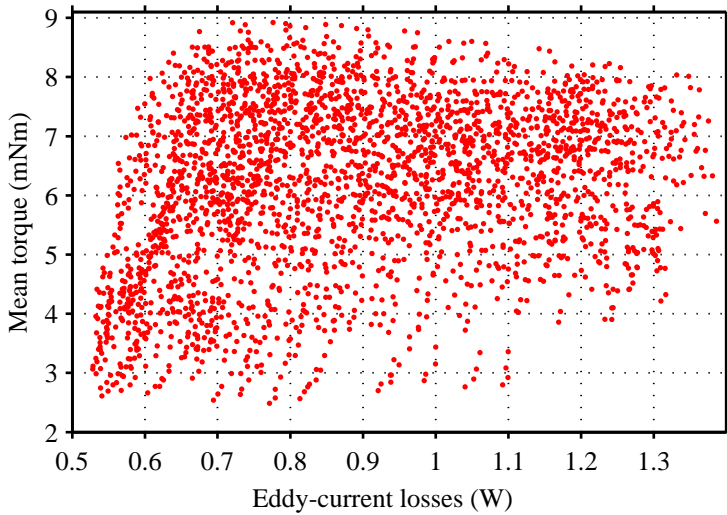


**Figure 8.14:** Rotor eddy-current losses losses and core losses at no-load and 200 000 r/min of the machines with stators made of cobalt-iron.

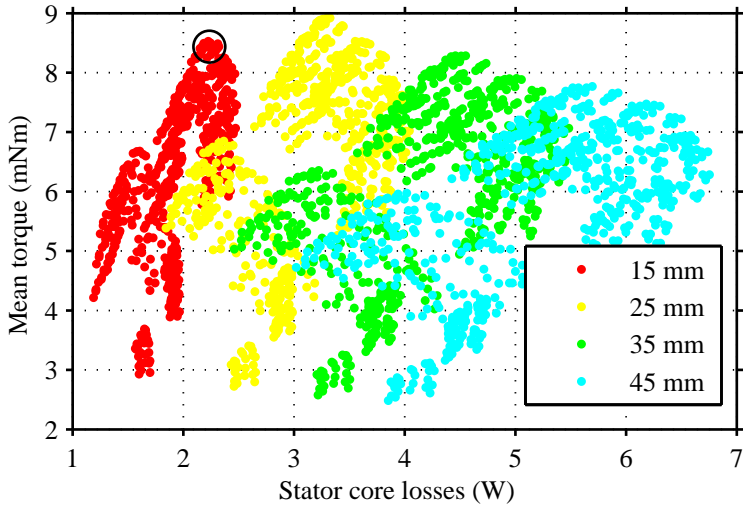


**Figure 8.15:** The effect of the stator length on the performance of the machines with stators made of cobalt-iron.

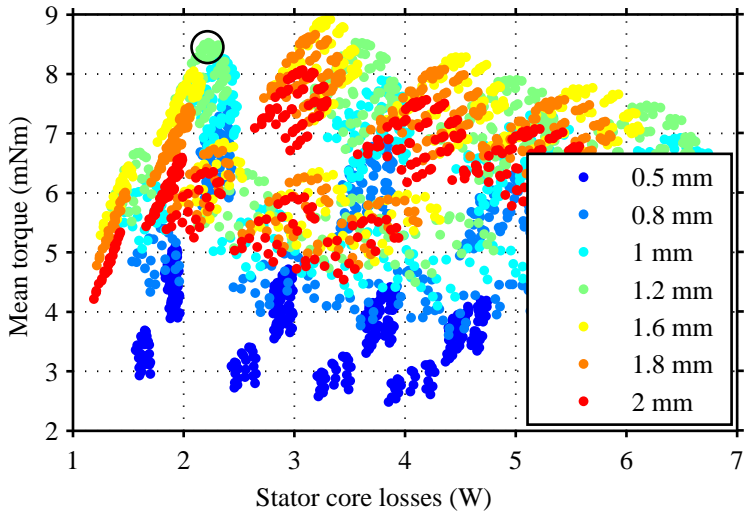


**Figure 8.16:** The effect of the leg width on the performance of the machines with stators made of cobalt-iron.

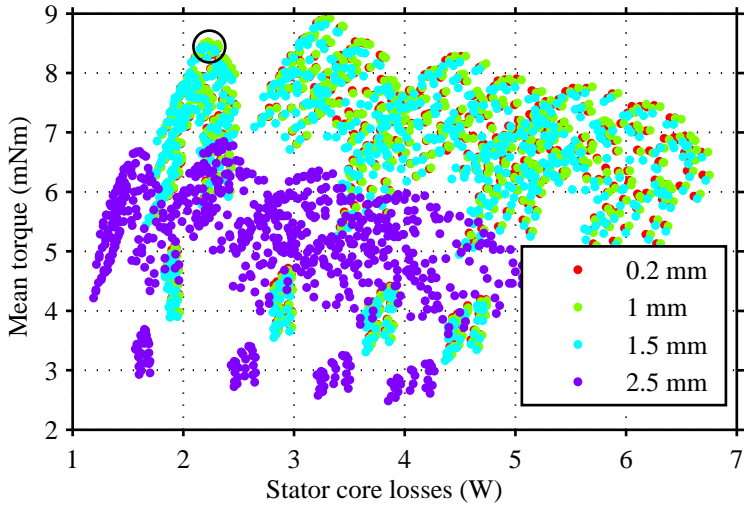


**Figure 8.17:** The effect of the shaft radius on the performance of the machines with stators made of cobalt-iron.

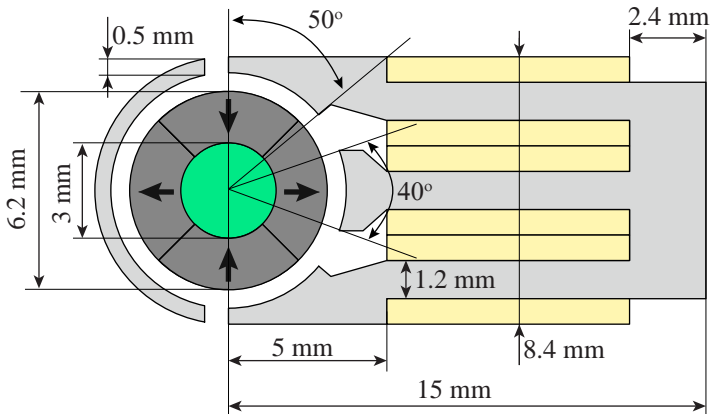


**Figure 8.18:** Mechanical dimensions of the selected machine. Active length (into page plane) of the machine is 6.4 mm.

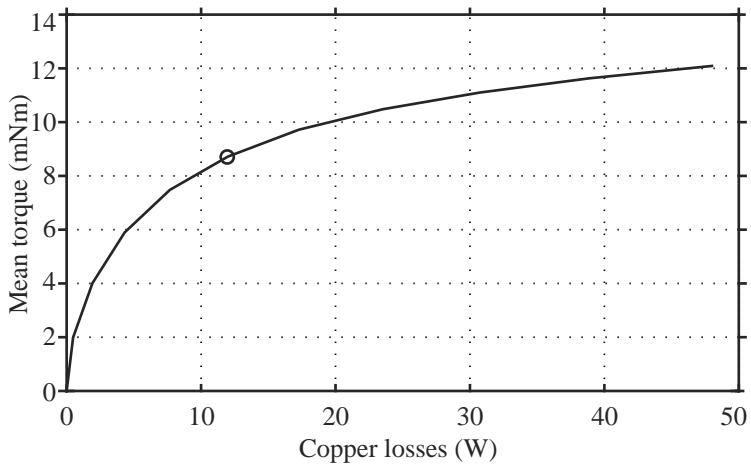


**Figure 8.19:** The average torque of the selected machine under different loads leading to different copper losses. The design point with 12 W copper losses is marked with a circle.



# Chapter 9

## Conclusions

### 9.1 Summary

High-speed electrical drives are gaining more and more interest in academia and are increasingly utilized in industry applications such as portable power generation, turbocompressors for heat pumps or air pressurization systems, spindles for micro-machining, attitude control systems for small satellites and optical applications like high-speed scanning. Some of these applications such as the turbocompressors benefit from a higher power density when the rotational speed is increased, as the volume of a machine decreases by increasing its speed for a given power rating and cooling capability.

In applications such as spindles, high-speed drives eliminate the need for using step-up gearboxes which results in a direct drive with a higher system reliability and a lower maintenance effort. However, the volume of the spindle tool housing may limit the size of a direct-drive machine and the maximum torque that can be generated. Such an application are dental handpieces.

In the state-of-the-art dental handpiece, an electric motor that is located in the body of the handpiece drives the drill through several stages of step-up mechanical transmission. The mechanical power transmission can be eliminated by placing a high-speed direct-drive machine in the tool head. However, the space in the tool head is strictly limited as the handpiece cannot be larger than a certain size due to ergonomic constraints. A similar application with space limits is desktop machin-

ing centers for processing very small pieces for watchmaking and medical applications, where the head size of the spindle limits the possible shapes of the work piece.

In this thesis, a novel electrical machine topology is presented for high-speed, direct-drive spindle applications where the space in the tool head is limited. The stator of the machine grows in one lateral direction outside the tool head, making use of the space that would otherwise not be utilized by a standard electrical machine placed in the tool head. The proposed machine is called *Lateral-Stator Machine* (LSM) due to the shape of its stator.

Several analytical approaches have been presented in literature for modeling various types of electrical machines. Even though they are computationally very effective, they cannot be used to predict the performance of the LSM as it depends heavily on the partial saturation of the core and on the stray fields. Therefore, 2-D FEM analysis is used for modeling the LSM.

The drive profile of a typical spindle application is simplified by considering only two operating points. In the high-speed operating point, the torque requirement of the application is sufficiently small to assume zero copper losses, and only the no-load losses are considered. In the low-speed, high-torque operating point on the other hand, the speed is sufficiently small to consider only the copper losses, which can be significantly higher than the no-load losses as this is an intermittent operating point. The limits for the no-load losses and the copper losses in these operating points are set based on thermal considerations. The design goal is to maximize the torque output of the machine at the low-speed, high-torque operating point for given copper losses while producing less no-load losses than the no-load loss limit when running at the high-speed operating point. A direct search method is used to find the optimum machine within a given range of parameters. Although computationally intensive, a direct search is simple to set up, it does not need a cost function and it has no risk of converging to a local optimum. As it analyzes the suboptimum regions of the parameter range with the same intensity, a direct search yields data that can be used for sensitivity analysis for any parameter and any performance criteria.

After the optimum machine design is identified, it is realized in hardware. The stresses in the rotor are studied using 2-D FEM analysis and 3-D FEM models are employed to study the rotor dynamics. Both

metallic and fiber reinforced polymer retaining sleeves are manufactured and tested.

A test bench that can evaluate the machine performance precisely in the two operating points mentioned above is designed and constructed. Deceleration tests are commonly used for measuring the overall (mechanical and electromagnetic) no-load losses of electrical machines. However, as the goal here is to verify the design procedure, the segregation of the mechanical and electromagnetic losses is required. Therefore, a deceleration test is proposed where only the electromagnetic losses can be obtained. For evaluating the machine performance at the zero-speed, high-torque operating point, a standstill torque measurement setup is designed in which the reaction torque is measured on the stator side in a bearingless configuration. Doing so, effect of bearing friction is omitted and the electromagnetic torque of the machine is measured directly.

The experimental results are shown to verify the design procedure. The standstill machine torque predicted by the 2-D FEM simulations matches the measured values. For the no-load losses, the 2-D FEM models predict higher losses than the measurements, which is expected due to the lack of the end resistances in calculation of the rotor eddy-current losses. However, 3-D FEM models are shown to predict the losses more accurately at the expense of significantly higher computational effort.

The asymmetric structure of the LSM along with the partial saturation of its stator core and the stator slotting lead to strong torque ripple, which results in undesired speed oscillations at lower speeds. In order to counteract this and to minimize the speed ripple, an FEM-based current profiling approach is presented. This active torque ripple compensation strategy is shown to lead to a ripple-free torque with only a slight increase in copper losses.

Similar to any other electronically commutated electrical machine, the LSM requires the knowledge of the rotor position for a closed-loop operation. In this thesis two different signal-injection-based position sensing methods are developed to estimate the rotor position. In the first method, a high-frequency signal is injected into one of the machine phases and the response of the machine is measured differentially on the other two phases. Even though not directly beneficial for the LSM as it is a high-saliency machine, it is shown that the differential measurements enable a very high position sensing sensitivity. There-

fore, this method enables the full speed range self-sensing operation of very low-saliency machines such as the slotless machines commonly used for speeds above 200 000 r/min. However, it is also shown that this method is challenging to implement in machines where a significant load-dependent saturation occurs. Furthermore, a specific LSM optimized as described above is shown to be not necessarily particularly suitable for impedance-tracking-based position estimation.

Therefore, second method for position sensing is introduced where the shielding iron of a section-type LSM can be turned into a position sensor by adding sensing coils. Doing so, the position sensing can be made independent of the load. Experimental results show that the proposed position sensing method with the sensing coils can be used from very low speeds up to 200 000 r/min. A discussion on several design aspects of such a position sensing method is given in order to clarify how to design a functional position sensor for different applications.

A comparison to state-of-the-art electrical machines reveals the advantages of the LSM for applications in confined spaces. A one pole-pair slotless PM machine with straight distributed windings and a multipole slotted PM machine with concentrated windings that fit in the same cross-sectional area of the tool head are shown to achieve less than one third of the local torque density compared to the first LSM prototype. The same active length is assumed for both the LSM and the other two types of machines for simplicity; therefore, the comparison is expected to be even more in favor of the LSM when the end windings of the cylindrical machines are taken into account. Similarly, the same loss limits are assumed for the LSM and the other two machines that fit in the same confined space. The comparison of torque capability is expected to change even further in favor of the LSM following a fair thermal evaluation of the state-of-the-art machines as they have more limited cooling capabilities.

## 9.2 Outlook

In this thesis, after the verification of the design of the first prototype with measurements, and after a comparison of the LSM and two different state-of-the-art electrical machines that shows the advantages of using an LSM in a space-restricted applications, the electromagnetic design of a second prototype is carried out. Cobalt-iron core material is shown to increase the torque density of the LSM further compared

to the amorphous core. However, at the time this thesis is being written, the production of small parts with sufficient accuracy using thin ( $\leq 0.1$  mm) cobalt-iron sheets is still challenging, and a few iterations are needed until the stator pieces can be manufactured successfully. Therefore, the manufacturing of small core parts needs to be perfected for applications where the highest torque densities are required.

The LSM exhibits a strong magnetic pull due to its asymmetric geometry. This results in a constant radial load for the bearings, and long lifetime tests are required to see the effect of the magnetic pull on the lifetime of the ball bearings.

Both a metallic (titanium) sleeve and composite (carbon, glass and aramid fiber) sleeves are designed, built and tested up to the rated speed in this work. However, the identification of the best sleeve requires detailed thermal modeling of the rotor and the analysis of different sleeve materials on the rotor temperature.

Finally, research on developing accurate 2-D analytical or FEM models for rotor eddy-current loss calculation is required for an accurate estimation of the rotor losses in the sleeve, the magnets and the rotor core.



# Bibliography

- [1] D. Gerada, A. Mebarki, N. Brown, C. Gerada, A. Cavagnino, and A. Boglietti, “High-speed electrical machines: Technologies, trends, and developments,” *IEEE Transactions on Industrial Electronics*, vol. 61, no. 6, pp. 2946–2959, Jun 2014.
- [2] C. Zwyssig, S. D. Round, and J. W. Kolar, “An ultrahigh-speed, low power electrical drive system,” *IEEE Transactions on Industrial Electronics*, vol. 55, no. 2, pp. 577–585, Feb 2008.
- [3] A. Borisavljevic, M. Kimman, P. Tsigkourakos, H. Polinder, H. Langen, R. Schmidt, and J. Ferreira, “Motor drive for a novel high-speed micro-milling spindle,” in *Proceedings of the IEEE/ASME International Conference on Advanced Intelligent Mechatronics (AIM)*, Jul 2009, pp. 1492–1497.
- [4] P.-D. Pfister and Y. Perriard, “Very-high-speed slotless permanent-magnet motors: Analytical modeling, optimization, design, and torque measurement methods,” *IEEE Transactions on Industrial Electronics*, vol. 57, no. 1, pp. 296–303, Jan 2010.
- [5] D. Krahenbühl, C. Zwyssig, H. Weser, and J. W. Kolar, “A miniature 500 000 r/min electrically driven turbocompressor,” *IEEE Transactions on Industry Applications*, vol. 46, no. 6, pp. 2459–2466, 2010.
- [6] S. Stevens, G. Deliege, J. Driesen, and R. Belmans, “A hybrid high speed electrical micromachine for micro scale power generation,” in *Proceedings of the IEEE International Conference on Electric Machines and Drives*, May 2005, pp. 1135–1142.

- [7] C. Zwyssig, T. Baumgartner, and J. W. Kolar, “High-speed magnetically levitated reaction wheel demonstrator,” in *Proceedings of the IEEE International Power Electronics Conference (IPEC - ECCE Asia)*, May 2014, pp. 1707–1714.
- [8] C. Zwyssig, “An ultra-high-speed electrical drive system,” Ph.D. dissertation, ETH Zurich, 2008.
- [9] C. Zwyssig, J. W. Kolar, and S. D. Round, “Megaspeed drive systems: pushing beyond 1 million r/min,” *IEEE/ASME Transactions on Mechatronics*, vol. 14, no. 5, pp. 564–574, Oct 2009.
- [10] A. Looser and J. W. Kolar, “An active magnetic damper concept for stabilization of gas bearings in high-speed permanent-magnet machines,” *IEEE Transactions on Industrial Electronics*, vol. 61, no. 6, pp. 3089–3098, Jun 2014.
- [11] J. Peirs, T. Waumans, P. Vleugels, F. Al-Bender, T. Stevens, T. Verstraete, S. Stevens, R. D’hulst, D. Verstraete, P. Fiorini, R. Van den Braembussche, J. Driesen, R. Puers, P. Hendrick, M. Baelmans, and D. Reynaerts, “Micropower generation with microgasturbines: A challenge,” *Proceedings of the Institution of Mechanical Engineers, Part C: Journal of Mechanical Engineering Science*, vol. 221, no. 4, pp. 489–500, 2007.
- [12] M. Kimman, H. Langen, J. Van Eijk, and R. Schmidt, “Design and realization of a miniature spindle test setup with active magnetic bearings,” in *Proceedings of the IEEE/ASME International Conference on Advanced Intelligent Mechatronics (AIM)*, Sep 2007, pp. 1–6.
- [13] L. Xiao-bao, L. Wen-he, and Z. Lin, “Design of a two-spindle CNC machine tool applications for dental restoration,” in *Proceedings of the Third International Conference on Measuring Technology and Mechatronics Automation (ICMTMA)*, vol. 1, Jan 2011, pp. 934–937.
- [14] G. M. Kurtzman, “Electric handpieces: An overview of current technology,” *Inside Dentistry*, vol. 3, no. 6, pp. 2946–2959, Jun 2007.

- 
- [15] N. Bianchi, S. Bolognani, and F. Luise, “Potentials and limits of high-speed PM motors,” *IEEE Transactions on Industry Applications*, vol. 40, no. 6, pp. 1570–1578, Nov 2004.
- [16] A. Borisavljevic, H. Polinder, and J. Ferreira, “On the speed limits of permanent-magnet machines,” *IEEE Transactions on Industrial Electronics*, vol. 57, no. 1, pp. 220–227, Jan 2010.
- [17] Y. Watanabe, Japanese Patent JP2 000 324 775A, 2000.
- [18] T. I. I. Hashimoto, Japanese Patent JP9 019 123A, 1997.
- [19] J. Luomi, C. Zwysig, A. Looser, and J. W. Kolar, “Efficiency optimization of a 100-W 500 000-r/min permanent-magnet machine including air-friction losses,” *IEEE Transactions on Industry Applications*, vol. 45, no. 4, pp. 1368–1377, Jul 2009.
- [20] Z. Zhu, D. Howe, E. Bolte, and B. Ackermann, “Instantaneous magnetic field distribution in brushless permanent magnet DC motors. I. Open-circuit field,” *IEEE Transactions on Magnetics*, vol. 29, no. 1, pp. 124–135, Jan 1993.
- [21] Z. Zhu and D. Howe, “Instantaneous magnetic field distribution in brushless permanent magnet DC motors. II. Armature-reaction field,” *IEEE Transactions on Magnetics*, vol. 29, no. 1, pp. 136–142, Jan 1993.
- [22] —, “Instantaneous magnetic field distribution in brushless permanent magnet DC motors. III. Effect of stator slotting,” *IEEE Transactions on Magnetics*, vol. 29, no. 1, pp. 143–151, Jan 1993.
- [23] —, “Instantaneous magnetic field distribution in permanent magnet brushless DC motors. IV. Magnetic field on load,” *IEEE Transactions on Magnetics*, vol. 29, no. 1, pp. 152–158, Jan 1993.
- [24] L. Wu, Z. Zhu, D. Staton, M. Popescu, and D. Hawkins, “Analytical prediction of electromagnetic performance of surface-mounted PM machines based on subdomain model accounting for tooth-tips,” *IET Electric Power Applications*, vol. 5, no. 7, pp. 597–609, Aug 2011.
- [25] 2605SA1 & 2605HB1M magnetic alloy datasheet, Metglas Inc., Conway, USA. <http://www.metglas.com/>.

- [26] J. Reinert, A. Brockmeyer, and R. De Doncker, "Calculation of losses in ferro- and ferrimagnetic materials based on the modified Steinmetz equation," *IEEE Transactions on Industry Applications*, vol. 37, no. 4, pp. 1055–1061, Jul 2001.
- [27] Z. Zhu, K. Ng, N. Schofield, and D. Howe, "Analytical prediction of rotor eddy current loss in brushless machines equipped with surface-mounted permanent magnets. i. magnetostatic field model," in *Proceedings of the Fifth International Conference on Electrical Machines and Systems (ICEMS)*, vol. 2, Aug 2001, pp. 806–809.
- [28] S. Ruoho, T. Santa-Nokki, J. Kolehmainen, and A. Arkkio, "Modeling magnet length in 2-D finite-element analysis of electric machines," *IEEE Transactions on Magnetics*, vol. 45, no. 8, pp. 3114–3120, Aug 2009.
- [29] Bimatec AG. Zurich, Switzerland. <http://www.bimatec.ch/>.
- [30] Rare earth permanent magnets catalogue, Vacuumschmelze GmbH & Co. KG. Hanau, Germany. <http://www.vacuumschmelze.com/>.
- [31] H. Jussila, P. Salminen, A. Parviainen, J. Nerg, and J. Pyrhonen, "Concentrated winding axial flux permanent magnet motor with plastic bonded magnets and sintered segmented magnets," in *Proceedings of the Eighteenth International Conference on Electrical Machines (ICEM)*, Sep 2008, pp. 1–5.
- [32] *Maxwell 2D technical notes*, Ansys Inc., 2013.
- [33] Titan Grade 5 (6Al-4V) catalogue, Bibus Metals Ag, Switzerland. <http://http://www.bibusmetals.ch/>.
- [34] Soft magnetic cobalt-iron-alloys catalogue, Vacuumschmelze GmbH & Co. KG. Hanau, Germany. <http://www.vacuumschmelze.com/>.
- [35] D. Lin, P. Zhou, W. N. Fu, Z. Badics, and Z. Cendes, "A dynamic core loss model for soft ferromagnetic and power ferrite materials in transient finite element analysis," *IEEE Transactions on Magnetics*, vol. 40, no. 2, pp. 1318–1321, Mar 2004.

- [36] W. Li, H. Qiu, X. Zhang, J. Cao, and R. Yi, "Analyses on electromagnetic and temperature fields of superhigh-speed permanent-magnet generator with different sleeve materials," *IEEE Transactions on Industrial Electronics*, vol. 61, no. 6, pp. 3056–3063, Jun 2014.
- [37] Z. Kolondzovski, A. Belahcen, and A. Arkkio, "Comparative thermal analysis of different rotor types for a high-speed permanent-magnet electrical machine," *IET Electric Power Applications*, vol. 3, no. 4, pp. 279–288, Jul 2009.
- [38] A. Borisavljevic, H. Polinder, and J. Ferreira, "Enclosure design for a high-speed permanent magnet rotor," in *Proceedings of the Fifth IET International Conference on Power Electronics, Machines and Drives (PEMD)*, Apr 2010, pp. 1–6.
- [39] A. Tüysüz, A. Schaubhut, C. Zwysig, and J. W. Kolar, "Model-based loss minimization in high-speed motors," in *Proceedings of the IEEE International Electric Machines Drives Conference (IEMDC)*, May 2013, pp. 332–339.
- [40] R&G Faserverbundwerkstoffe GmbH, Waldenbuch, Germany. <http://www.r-g.de/>.
- [41] Myonic standard catalog, Myonic GmbH, Leutkirch, Germany. <http://www.myonic.com/>.
- [42] Somos ProtoTherm 12120 datasheet, Royal DSM, Heerlen, Netherlands. <http://www.dsm.com/>.
- [43] 9329A reaction torque sensor datasheet, Kistler Group, Winterthur, Switzerland. <http://www.kistler.com/>.
- [44] 5011B charge amplifier datasheet, Kistler Group, Winterthur, Switzerland. <http://www.kistler.com/>.
- [45] A. Nagorny, "A simple and accurate method for the experimental performance evaluation of high speed sensorless brushless DC motors," in *Proceeding of the IEEE International Electric Machines and Drives Conference (IEMDC)*, May 2009, pp. 916–921.
- [46] CM-2-500 datasheet, Celeroton AG. Zurich, Switzerland. <http://www.celeroton.com/>.

- [47] J. Shao, D. Nolan, and T. Hopkins, "A novel direct back EMF detection for sensorless brushless DC (BLDC) motor drives," in *Proceedings of the Seventeenth Annual IEEE Applied Power Electronics Conference and Exposition (APEC)*, vol. 1, 2002, pp. 33–37.
- [48] S.-C. Yang and R. Lorenz, "Comparison of resistance-based and inductance-based self-sensing controls for surface permanent-magnet machines using high-frequency signal injection," *IEEE Transactions on Industry Applications*, vol. 48, no. 3, pp. 977–986, May 2012.
- [49] M. Schroedl, "Sensorless control of AC machines at low speed and standstill based on the INFORM method," in *Conference Record of the Thirty-First IEEE Industry Applications Society Annual Meeting (IAS)*, vol. 1, Oct 1996, pp. 270–277.
- [50] E. Robeischl and M. Schroedl, "Optimized INFORM measurement sequence for sensorless PM synchronous motor drives with respect to minimum current distortion," *IEEE Transactions on Industry Applications*, vol. 40, no. 2, pp. 591–598, Mar 2004.
- [51] P. Weinmeier, "Sensorless high dynamic control of a hybrid reluctance machine in the low frequency range including standstill," Ph.D. dissertation, TU Vienna, 1998.
- [52] T. Wolbank and J. Machl, "A modified PWM scheme in order to obtain spatial information of AC machines without mechanical sensor," in *Proceedings of the Seventeenth Annual IEEE Applied Power Electronics Conference and Exposition (APEC)*, vol. 1, 2002, pp. 310–315.
- [53] H. Kim and R. D. Lorenz, "Carrier signal injection based sensorless control methods for IPM synchronous machine drives," in *Conference Record of the Thirty-Ninth Industry Applications Society Annual Meeting (IAS)*, vol. 2, Oct 2004, pp. 977–984.
- [54] D. Raca, P. Garcia, D. Reigosa, F. Briz, and R. Lorenz, "Carrier-signal selection for sensorless control of PM synchronous machines at zero and very low speeds," *IEEE Transactions on Industry Applications*, vol. 46, no. 1, pp. 167–178, Jan 2010.
- [55] J. F. Gieras, *Permanent magnet motor technology*. CRC Press, 2009.

- [56] C. De Angelo, G. Bossio, G. Garcia, J. Solsona, and M. Valla, "Sensorless speed control of permanent magnet motors with torque ripple minimization," in *Proceedings of the Twenty-Eighth Annual Conference of the IEEE Industrial Electronics Society (IECON)*, vol. 1, Nov 2002, pp. 680–685.
- [57] S.-J. Park, H.-W. Park, Y.-J. Lee, M.-H. Lee, and C.-U. Kim, "A new approach for pulsating torque minimization of brushless PM motor," in *Proceedings of the Twenty-Sixth Annual Conference of the IEEE Industrial Electronics Society (IECON)*, vol. 1, 2000, pp. 76–82.
- [58] IRF6674TRPbF datasheet, International Rectifier, El Segundo, USA. <http://www.irf.com/>.
- [59] R. W. Erickson and D. Maksimovic, *Fundamentals of power electronics*. Springer, 2011.
- [60] J. W. Kolar, T. Friedli, F. Krismer, A. Looser, M. Schweizer, R. Friedemann, P. Steimer, and J. Bevirt, "Conceptualization and multiobjective optimization of the electric system of an airborne wind turbine," *IEEE Journal of Emerging and Selected Topics in Power Electronics*, vol. 1, no. 2, pp. 73–103, Jun 2013.
- [61] J. Cros and P. Viarouge, "Synthesis of high performance PM motors with concentrated windings," *IEEE Transactions on Energy Conversion*, vol. 17, no. 2, pp. 248–253, Jun 2002.
- [62] A. Looser, T. Baumgartner, J. W. Kolar, and C. Zwyssig, "Analysis and measurement of three-dimensional torque and forces for slotless permanent-magnet motors," *IEEE Transactions on Industry Applications*, vol. 48, no. 4, pp. 1258–1266, Jul 2012.
- [63] J. Pyrhonen, T. Jokinen, and V. Hrabovcová, *Design of rotating electrical machines*. Wiley, 2014.
- [64] M. Markovic, L. Saunders, and Y. Perriard, "Determination of the thermal convection coefficient for a small electric motor," in *Proceedings of the Forty-First IEEE Industry Applications Society Annual Meeting*, vol. 1, Oct 2006, pp. 58–61.
- [65] F. P. Incropera, D. P. DeWitt, T. L. Bergman, and A. S. Lavine, *Introduction to heat transfer*. Wiley, 2007.

- [66] D. Howey, P. Childs, and A. Holmes, “Air-gap convection in rotating electrical machines,” *IEEE Transactions on Industrial Electronics*, vol. 59, no. 3, pp. 1367–1375, Mar 2012.

# Curriculum Vitae

## Personal

Name	Arda Tüysüz
Date of birth	18 <sup>th</sup> of February 1984
Place of origin	Istanbul, Turkey

## Education

2009 – 2014	Ph.D. at the Power Electronic Systems Laboratory (PES), ETH Zurich, Switzerland Supervised by Prof. Dr. Johann W. Kolar
2006 – 2009	M.Sc. in Electrical Power Engineering RWTH Aachen University
2002 – 2006	B.Sc. in Electrical Engineering Istanbul Technical University

## Work Experience

2009 – 2014	Research assistant at the Power Electronic Systems Laboratory (PES), ETH Zurich
2006 – 2008	Student assistant at the Institute for Power Electronics and Electrical Drives (ISEA), RWTH Aachen, Germany
2008	Internship with ABB Corporate Research, Västerås, Sweden
2006	Teaching assistant at Istanbul Technical University, Turkey